

**KARADENİZ TECHNICAL UNIVERSITY
THE GRADUATE SCHOOL OF NATURAL AND APPLIED SCIENCES**

CIVIL ENGINEERING DEPARTMENT

**STATIC AND DYNAMIC ANALYSIS OF AXISYMMETRIC STRUCTURES
USING HARMONIC SOLID RING FINITE ELEMENT MODELING**

MASTER THESIS

Ali İhsan KARAKAŞ

**JANUARY 2012
TRABZON**

**KARADENİZ TECHNICAL UNIVERSITY
THE GRADUATE SCHOOL OF NATURAL AND APPLIED SCIENCES**

CIVIL ENGINEERING DEPARTMENT

**STATIC AND DYNAMIC ANALYSIS OF AXISYMMETRIC STRUCTURES
USING HARMONIC SOLID RING FINITE ELEMENT MODELING**

Ali İhsan KARAKAŞ, B.S.

**Submitted to the Graduate School of Karadeniz Technical University in Partial
Fulfillment of the Requirements for the
Degree of Master of Science**

**Date of submission : 20.12.2011
Date of defence examination : 09.01.2011**

Supervisor : Prof. Dr. Ayşe DALOĞLU

Trabzon 2012

Approval of the thesis

**STATIC AND DYNAMIC ANALYSIS OF AXISYMMETRIC STRUCTURES
USING HARMONIC SOLID RING FINITE ELEMENT MODELING**

submitted by **Ali İhsan KARAKAŞ** in partial fulfillment of the requirements for the degree of **Master of Science in Civil Engineering Department at Karadeniz Technical University** by examining committee constituted by the graduate school board with the reference number of 595-2585 on December 12 th of 2011.

Examining Committee Members

Prof. Dr. Ragıp ERDÖL

Prof. Dr. Ayşe DALOĞLU

Prof. Dr. Orhan AYDIN

Prof. Dr. Sadettin KORKMAZ

Director, Graduate School of Natural and Applied Sciences

ACKNOWLEDGEMENTS

In the first place I would like to record my sincere gratitude to my supervisor Prof. Dr. Ayşe DALOĞLU for her supervision, insightful comments and motivation she provided from the very early stage of this research. Her guidance helped me in all the time of research and writing of this thesis.

Besides my supervisor, I gratefully thank Prof. Dr. Ragıp ERDÖL and Prof. Dr. Orhan AYDIN for their constructive comments on this thesis. I am thankful that in the midst of all their activity, they accepted to be members of the reading and evaluation committee.

Also, I would like to express my special gratitude to Asst. Prof. Korhan ÖZGAN for his support, guidance, helps and constructive comments throughout my research.

I offer my regards and blessings to all of those who supported me in any respect during the completion of the thesis.

The Turkish Scientific and Technical Research Council (TUBITAK) is also gratefully acknowledged due to the financial support provided during my M.Sc. research.

Last but not the least; I would like to thank my family for giving birth to me at the first place and supporting me spiritually throughout my life.

Ali İhsan KARAKAŞ
Trabzon 2012

THESIS STATEMENT

I hereby declare that all information in this thesis titled as “Static and Dynamic Analysis of Axisymmetric Structures Using Harmonic Solid Ring Finite Element Modeling” has been completed under the responsibility of my supervisor Prof. Dr. Ayşe DALOĞLU and presented in accordance with academic rules and ethical conduct. I also declare that, as required by these rules and conduct, I have fully cited and referenced all material and results that are not original to this work. 09.01.2012.

Ali İhsan KARAKAŞ

TABLE OF CONTENTS

	<u>Page</u>
ACKNOWLEDGEMENTS	III
THESIS STATEMENT	IV
TABLE OF CONTENTS	V
ÖZET	VII
SUMMARY	IX
LIST OF FIGURES	X
LIST OF TABLES	XIV
NOTATIONS	XV
1. GENERAL INFORMATION	1
1.1. Introduction	1
1.2. Literature Review	2
1.3. Objectives of This Research	4
1.4. Selection of the Model and the Computational Technique	5
1.5. Finite Element Modeling of Axisymmetric Structures	5
1.6. Geometry Definitions of Axisymmetric Problems	6
1.7. Element Coordinates and Shape Functions	8
1.8. Strains and Stresses in an Axisymmetrical Solid Element	11
1.9. Plane Axisymmetric Finite Element	12
1.10. Plane Axi-antisymmetric Finite Element	16
1.11. Harmonic Finite Element	17
1.12. Element Stiffness Matrix	24
1.13. Element Mass Matrix	28
1.14. Element Nodal Force Vectors	31
1.14.1. Fourier Series Representation of Loading	31
1.14.2. Consistent Body Force Vector	33
1.14.3. Consistent Surface Force Vector	35
1.14.4. Consistent Line and Concentrated Load Vectors	37
1.15. Modal Analysis	39

1.16.	Static Analysis	40
1.17.	Linear Dynamic Analysis	41
1.17.1.	The Newmark Method.....	42
1.18.	Model Reduction for Linear Systems.....	43
2.	NUMERICAL EXAMPLES AND RESULTS	45
2.1.	Accuracy Verification of the Program.....	45
2.1.1.	Hollow Cylinder Under Various Loadings.....	45
2.1.2.	Modal Analysis of a Hollow Cylinder.....	47
2.1.3.	Internally Pressurized Thick Cylinder	48
2.1.4.	Rotating Thin Disc	53
2.1.5.	Circular Plate Bending.....	56
2.2.	Analysis of a Cooling Tower.....	64
2.2.1.	Geometry and Material Properties of the Cooling Tower	65
2.2.2.	Loadings of the Cooling Tower.....	66
2.2.3.	Free Vibration Analysis of the Cooling Tower	74
2.2.4.	Static Analysis of the Cooling Tower	82
2.2.5.	Dynamic Analysis of the Cooling Tower	92
3.	CONCLUSIONS AND RECOMMENDATIONS	99
4.	REFERENCES	102
CURRICULUM VITA		

Yüksek Lisans

ÖZET

HARMONİK HALKA SONLU ELAMAN MODELLEMESİ KULLANARAK
EKSENEL SİMETRİK YAPILARIN STATİK VE DİNAMİK ANALİZİ

Ali İhsan KARAKAŞ

Karadeniz Teknik Üniversitesi
Fen Bilimleri Enstitüsü
İnşaat Mühendisliği Bölümü
Danışman: Prof. Dr. Ayşe DALOĞLU
2012, 103 Sayfa

Düzgün iç ve dış basınç gibi aksenel simetrik olan ve/veya rüzgâr ve deprem gibi aksenel simetrik olmayan yüklere maruz kalan aksenel simetrik yapıların statik, serbest ve zorlanmış titreşim analizleri harmonik sonlu eleman yöntemiyle halka elemanlar kullanarak incelenmiştir. Harmonik sonlu eleman yönteminde aksenel simetrik olmayan yüklerin Fourier serileri şeklinde ifade edilmesiyle üç boyutlu problemler iki boyuta, iki boyutlu düzlem problemler de bir boyuta indirgenebilmektedir. Böylece her Fourier terimi için düzlem aksenel simetrik benzeri analiz yapılır ve aksenel simetrik olmayan yük altındaki problemin tam çözümü yeterli sayıda terim çözümlerinin süperpozisyonuyla elde edilir. Bu amaçla Matlab yardımıyla bir bilgisayar programı kodlanmıştır. Programın güvenilirliği iç basınçlı kalın cidarlı silindir, dönen ince disk ve basit mesnetli ince plak gibi kesin çözümü elde edilebilen örneklerle kontrol edilmiştir. Çalışmada dörtgen enkesitli 4 ve 9 düğüm noktası bulunan iki halka eleman kullanılmıştır. Bu iki eleman sonuçların hassasiyeti ile kayma ve hacimsel kilitlenme problemleri açısından birbirleriyle karşılaştırılmıştır. 4 düğüm noktalı elemanın aksine 9 düğüm noktalı elemanın kilitlenme problemlerinden etkilenmediği gözlenmiştir.

Programın güvenilirliği sağlandıktan sonra 9 düğüm noktalı eleman kullanılarak bir soğutma kulesinin TS 498 ve Eurocode'a göre tanımlanan rüzgâr yükleri altında statik ve Düzce deprem yükü altında dinamik analizleri yapılmıştır. Statik analiz sonucunda rüzgâr basıncının çevresel dağılımının yer değiştirmeler ve gerilmeler üzerindeki etkisi incelenmiştir. Yer değiştirme ve gerilmelerin Eurocode'a göre hesaplanan yükler altında çok daha büyük değerler aldığı görülmüştür. Bu durumun Eurocode'a göre elde edilen çevresel dağılım için Fourier açılımındaki 2. ve 3. terimlerin katsayılarının diğerlerinden

daha büyük deęerler almasıyla yapının bu yükleme altında dalgalanan çevresel hareketlere büyük ölçüde maruz kalmasından kaynaklandığı düşünölmektedir. Fourier katsayılarının büyüklüğünden yüklemenin hangi tür deformasyonlara (kabuk veya kiriş benzeri) daha çok sebep olacağı anlaşılabilir. Serbest titreşim analizleri sonucunda yapının doğal frekanslarının artan çevresel mod numarasıyla bir minimum değere kadar azaldığı ve bu değerdan sonra ise artmaya başladığı görölmüştür. Bu davranışın silindirik kabuk tipi yapıların tipik bir özelliğı olduğı söylenebilir.

Son olarak parametrik çalışma yapılarak kule yüksekliğinin, eğriliğinin ve kabuk kalınlığının yapının serbest titreşim ve sismik davranışı üzerindeki etkileri incelenmiştir. Titreşim periyodunun artan eğrilikle yaklaşık olarak doğrusal azaldığı, büyük eğriliklerde ise bu eğilimin tersine döndüğü gözlenmiştir. Ayrıca yapının yüksekliği arttıkça periyodun arttığı ve kabuk kalınlığı arttıkça periyodun azaldığı görölmüştür. En büyük periyodun artan kalınlık ve yükseklikle lineer olarak deęiştığı de izlenmiştir. Birinci yanal mod periyodunun artan kabuk kalınlığından etkilenmediğı fakat artan kalınlıkla modun daha erken oluştuğı gözlenmiştir. Benzer şekilde birinci yanal modun oluşum sırasının artan yükseklikle azaldığı görölmüştür. Dinamik analizlerde kule yüksekliğine, eğriliğine ve kabuk kalınlığına bağılı olarak gerilmelerde dikkate deęer deęişimlerin meydana geldiğı izlenmiştir.

Anahtar Kelimeler: Eksenel Simetrik Yapılar, Halka Sonlu Eleman, Harmonik Analiz, Fourier Serisi, Rüzgâr Yüğü, Hiperbolik Soęutma Kulesi, Statik ve Dinamik Analiz, Serbest Titreşim.

Master Thesis

SUMMARY

STATIC AND DYNAMIC ANALYSIS OF AXISYMMETRIC STRUCTURES
USING HARMONIC SOLID RING FINITE ELEMENT MODELING

Ali İhsan KARAKAŞ

Karadeniz Technical University
The Graduate School of Natural and Applied Sciences
Civil Engineering Department
Supervisor: Prof. Dr. Ayşe DALOĞLU
2012, 103 Pages

Static, free and forced vibration analysis of axisymmetric structures under non-axisymmetric loadings such as wind and earthquake as well as axisymmetric loadings such as internal or external pressure were studied using harmonic solid ring finite elements. With the help of harmonic analysis physically three dimensional problems can be reduced to two dimensional problems by expressing non-axisymmetric loading in the form of Fourier series. The complete solution for the problem is obtained by superimposing a reasonable number of solutions for load components. 4-noded (Ring4) and 9-noded (Ring9) solid quadrilateral ring elements were used for the finite element analysis. A computer program for the purpose was coded in Matlab and verified solving several benchmark problems. During verification process these elements were compared with each other for accuracy, shear and volumetric locking. Ring9 seemed to be free of locking problems whereas Ring4 suffered from locking.

After verification process a cooling tower was analyzed quasi-statically under wind loadings described in accordance with TS 498 and Eurocode and dynamically under Düzce earthquake using Ring9. It was realized that the circumferential distribution of wind pressure influenced the displacements and stresses significantly. Additionally, Fourier series coefficients of wind loadings indicate that the significant portion of the loading will cause shell or beam like deformations. Finally, the influence of height, thickness and curvature on the free vibration and seismic response of cooling towers were examined with a parametric study. It was recognized that the period of vibration tended to decrease approximately linearly with increasing curvature, but for high curvatures this trend reversed. Likewise, the variations in the fundamental period of vibration with shell thickness and height were approximately linear. As well, remarkable changes in stresses were noticed for cooling towers with different wall thickness and curvature in seismic analysis.

Key Words: Axisymmetric Structures, Ring Finite Element, Harmonic Analysis, Fourier Series, Wind Loading, Hyperbolic Cooling Towers, Static and Dynamic Response, Free Vibration.

LIST OF FIGURES

	<u>Page</u>
Figure 1. Generators of an axisymmetric object and an element	6
Figure 2. Nodal numbering and global cylindrical coordinate system of (a) 4-node (b) 9-node quadrilateral ring element cross sections	8
Figure 3. Coordinate transformation of (a) 4-noded (b) 9-noded quadrilateral ring elements	9
Figure 4. Perspective view of the shape functions for (a) node 1 of the 4-node bilinear quadrilateral ring and (b) node 1 (c) node 5 (d) node 9 of the 9- node biquadratic quadrilateral ring	11
Figure 5. Strain components in an axisymmetrical solid element	12
Figure 6. Load components in an axisymmetric body:	32
Figure 7. Plots of constant and the first two cosine and sine terms.....	32
Figure 8. FEM discretization for the hollow cylinder under various loadings (a) 10-element Ring4 discretization (b) 5-element Ring9 discretization.....	46
Figure 9. Two example FEM discretization for the pressurized thick cylinder (a) 4- element Ring4 discretization of a slice (b) 2-element Ring9 discretization of a slice	49
Figure 10. Computed versus exact (a) radial displacements (b) radial stresses (c) hoop stresses using Ring4 and (d) radial displacements (e) radial stresses (f) hoop stresses using Ring9 for different meshes of the pressurized hollow cylinder	50
Figure 11. Computed versus exact (a) radial stresses (b) hoop stresses using Ring4 (c) radial stresses (d) hoop stresses using Ring9 for different Poisson's ratio.....	52
Figure 12. Two example FEM discretization for the rotating thin disc (a) 4-Ring4 (b) 2-Ring9 element discretization of disc section.....	53
Figure 13. Computed versus exact (a) radial displacements (b) radial stresses (c) hoop stresses using Ring4 and (d) radial displacements (e) radial stresses (f) hoop stresses using Ring9 for different meshes of the rotating thin disc	55
Figure 14. Two example FEM discretization for the circular plate bending (a) 8-Ring4 (b) 2-Ring9 element discretization	56
Figure 15. Point loaded circular plate: axial displacements for (a) element meshes of Ring4 and (b) element meshes of Ring9.....	57
Figure 16. Point loaded circular plate: radial stresses for (a) element meshes of Ring4 and (b) element meshes of Ring9	58

Figure 17. Dimensionless center axial displacements versus number of elements for various thicknesses to diameter ratios (a) $H/D=0.001$ (b) $H/D=0.005$ (c) $H/D=0.015$ (d) $H/D=0.025$ (e) $H/D=0.035$ (f) $H/D=0.05$	59
Figure 18. Dimensionless center radial stress versus number of elements for various thicknesses to diameter ratios (a) $H/D=0.001$ (b) $H/D=0.005$ (c) $H/D=0.015$ (d) $H/D=0.025$ (e) $H/D=0.035$ (f) $H/D=0.05$	60
Figure 19. Dimensionless center axial displacements of the simply supported circular plate under uniformly distributed load	62
Figure 20. Dimensionless center radial stresses at the bottom surface of the simply supported circular plate under uniformly distributed load.....	62
Figure 21. Geometry and elements of a cooling tower.....	66
Figure 22. The wind pressure distribution over the height of the cooling tower according to TS 498.....	68
Figure 23. The wind pressure distribution over the height of the cooling tower according to Eurocode	68
Figure 24. Circumferential wind pressure distribution coefficients according to TS 498.....	69
Figure 25. Circumferential wind pressure distribution coefficients according to Eurocode	69
Figure 26. Fourier harmonics used to represent the wind load distribution coefficient over the circular section of the cooling tower for TS 498	71
Figure 27. Real distribution and Fourier approximation of the wind load distribution coefficients using eight Fourier harmonics for TS 498	71
Figure 28. Fourier harmonics used to represent the wind load distribution coefficient.....	72
Figure 29. Real and Fourier approximations of the wind load distribution coefficients using eight Fourier harmonics for Eurocode	72
Figure 30. Acceleration versus time history record of the Düzce earthquake.....	73
Figure 31. Acceleration versus time history record of the Düzce earthquake between 5-10 seconds	74
Figure 32. Natural frequencies with respect to circumferential mode number	75
Figure 33. Circumferential mode shapes for (a) $m=0$ (b) $m=1$ (c) $m=2$ (d) $m=3$ (e) $m=4$ (f) $m=5$ (g) $m=6$ (h) $m=7$	77
Figure 34. Normalized meridional vibration modes $n=1,2,3$ for the circumferential modes (a) $m=1$ (b) $m=2$ (c) $m=3$ (d) $m=4$	78
Figure 35. Effect of curvature on the response of first five circumferential periods of vibration.....	82
Figure 36. Radial displacements at windward meridian ($\theta=0$) of the cooling tower throughout the height for each wind load harmonics according to TS 498.....	85

Figure 37. Radial displacements at windward meridian ($\theta=0$) of the cooling tower throughout the height for each wind load harmonics according to Eurocode ..	85
Figure 38. Axial displacements at windward meridian ($\theta=0$) of the cooling tower throughout the height for each wind load harmonics according to TS 498.....	86
Figure 39. Axial displacements at windward meridian ($\theta=0$) of the cooling tower throughout the height for each wind load harmonics according to Eurocode ..	86
Figure 40. Radial displacements at windward meridian ($\theta=0$) of the cooling tower under wind load throughout the height according to TS 498 and Eurocode	87
Figure 41. Axial displacements at windward meridian ($\theta=0$) of the cooling tower under wind load throughout the height according to TS 498 and Eurocode	87
Figure 42. Circumferential stresses at windward meridian ($\theta=0$) throughout the height of the cooling tower under deadweight	88
Figure 43. Meridional stresses at windward meridian ($\theta=0$) throughout the height of the cooling tower under deadweight.....	88
Figure 44. Circumferential stresses at windward meridian ($\theta=0$) throughout the height of the cooling tower for each wind load harmonics according to Eurocode	89
Figure 45. Meridional stresses at windward meridian ($\theta=0$) throughout the height of the cooling tower for each wind load harmonics according to Eurocode.....	89
Figure 46. Circumferential stresses at windward meridian ($\theta=0$) throughout the height of the cooling tower for each wind load harmonics according to TS 498.....	90
Figure 47. Meridional stresses at windward meridian ($\theta=0$) throughout the height of the cooling tower for each wind load harmonics according to TS 498	90
Figure 48. Circumferential stresses at windward meridian ($\theta=0$) throughout the height of the cooling tower under wind load according to TS 498 and Eurocode	91
Figure 49. Meridional stresses at windward meridian ($\theta=0$) throughout the height of the cooling tower under wind load according to TS 498 and Eurocode.....	91
Figure 50. Distribution of the circumferential stress around the circumference at the base of the Stanwell tower subjected to wind pressure	92
Figure 51. Distribution of the circumferential stress around the circumference at the top of the Stanwell tower subjected to wind pressure	92
Figure 52. Responses along the three different heights of hyperbolic cooling tower under Düzce earthquake loading of (a) the lateral deflection (b) the meridional stress and (c) the circumferential stress when the maximum values are reached.....	95
Figure 53. (a) Meridional and (b) Circumferential stress resultants of the three different wall thicknesses of the hyperbolic cooling tower under Düzce earthquake loading along the height when the maximum values are reached.....	96

Figure 54. (a) Meridional and (b) circumferential stress responses of two different curvatures of the hyperbolic cooling tower under Düzce earthquake loading along the height when the maximum values are reached	96
Figure 55. Meridional stress responses along the height of the Stanwell hyperbolic cooling tower under Düzce earthquake loading	97
Figure 56. Circumferential stress responses along the height of the Stanwell hyperbolic cooling tower under Düzce earthquake loading	97
Figure 57. Time history of the (a) maximum lateral (radial) displacement (b) maximum meridional stress and (c) maximum circumferential stress of the Stanwell tower under Düzce earthquake loading	98

LIST OF TABLES

	<u>Page</u>
Table 1. Parameters of some practically used revolutionary objects	7
Table 2. Cylinder deformations under various loadings	47
Table 3. Comparison of natural frequencies obtained from R4, R9 and brick elements for different modes (MR: model reduction)	48
Table 4. Dimensionless center displacement values of the simply supported circular plate under uniformly distributed load for various thickness/diameter ratios and integration techniques.....	63
Table 5. Dimensionless radial stress values at the bottom of the simply supported circular plate under uniformly distributed load for various thickness/diameter ratios and integration techniques.....	64
Table 6. Functions of pressure coefficient distribution curve in Eurocode.....	69
Table 7. Coefficients of Fourier harmonics for the circumferential distribution of the wind load according to TS 498 and Eurocode.....	70
Table 8. Natural frequencies of the Stanwell cooling tower (n:meridional mode, m:circumferential mode).....	76
Table 9. Finite element model verification; comparison of present results with those from previously established solutions	76
Table 10. Circumferential and lateral periods of vibration of hyperbolic cooling towers of the same height and curvature with variation in shell-wall thickness	80
Table 11. Circumferential and lateral periods of vibration of hyperbolic cooling towers of the same curvature and shell wall thickness with variation in height of the structure.....	81
Table 12. Circumferential and lateral periods of vibration of hyperbolic cooling tower of the same height and shell wall thickness with variation in curvature (throat diameter) of the structure	81
Table 13. Six different models analyzed for earthquake loading	93

NOTATIONS

A_m	Fourier coefficients
A_e	Element cross sectional area
B	Strain-displacement matrix
B_e	Strain-displacement matrix of bending terms
B_γ	Strain-displacement matrix of shear terms
B_m	Strain-displacement matrix for harmonic mode m
C	Global damping matrix
D	Elasticity matrix
$\bar{d}_m, \overline{\overline{d}}_m$	Symmetric and antisymmetric nodal displacements for harmonic m
dV, dS, dl	Infinitesimal volume, surface, and line
dof	Degrees of freedom
E	Modulus of elasticity
FI	Full integration
FEM	Finite element method
$\overline{[g_{\theta m}]_u}, \overline{\overline{[g_{\theta m}]_u}}$	Harmonic matrices for symmetric and antisymmetric displacement
$\overline{[g_{\theta m}]_\varepsilon}, \overline{[g_{\theta m}]_\gamma}$	Harmonic matrices for symmetric bending and shear terms
$\overline{\overline{[g_{\theta m}]_\varepsilon}}, \overline{\overline{[g_{\theta m}]_\gamma}}$	Harmonic matrices for antisymmetric bending and shear terms
h	Wall thickness
J	Jacobian matrix
J_Γ	Arc length Jacobian
K	Global stiffness matrix
k	Element stiffness matrix
k_m	Element stiffness matrix for harmonic term m
$\bar{k}_m, \overline{\overline{k}}_m$	Symmetric and antisymmetric element stiffness matrices for harmonic m
k_t	Upper curvature
k_b	Lower curvature
L	Differential operator matrix

M	Global mass matrix
m	Harmonic term number
$\bar{m}_m, \underline{m}_m$	Symmetric and antisymmetric element mass matrices for harmonic m
MR	Model reduction
N	Shape function matrix
n_{er}	Number of elements in radial direction
n_{ez}	Number of elements in axial direction
P	Global load vector
q_b, q_s, q_l	Body, surface and line load components
q_r, q_θ, q_z	Load vector components in radial, circumferential, axial directions
$\bar{q}_{rm}, \bar{q}_{\theta m}, \bar{q}_{zm}$	Symmetric load amplitudes for harmonic term m
$\underline{q}_{rm}, \underline{q}_{\theta m}, \underline{q}_{zm}$	Antisymmetric load amplitudes for harmonic term m
$q(z)$	Effective velocity pressure
R	Reduction matrix
SRI	Selectively reduced integration
T_m	Kinetic energy for harmonic m
u_r, u_θ, u_z	Displacement vectors in radial, circumferential, axial directions
$\bar{u}_{rm}, \bar{u}_{\theta m}, \bar{u}_{zm}$	Symmetric displacement amplitudes harmonic term m
$\underline{u}_{rm}, \underline{u}_{\theta m}, \underline{u}_{zm}$	Antisymmetric displacement amplitudes for harmonic term m
\dot{u}, \ddot{u}	Velocity and acceleration vectors
U_e	Element strain energy
ν	Poisson's ratio
ω	Angular frequency
λ	Eigenvalue
ϕ	Eigenvector
Γ	Inverse of Jacobian matrix
ρ	Mass density
σ	Stress vector
ε	Strain vector

1. GENERAL INFORMATION

1.1. Introduction

The treatment of axisymmetric structures has considerable practical interest in aerospace, civil, mechanical and nuclear engineering because of their simplicity of fabrication, optimality in terms of strength to weight ratio due to favorable distribution of the structural material and multipurpose usages as both structure and shelter such as containers. Specific examples of such structures are pressure vessels, containment vessels, pipes, cooling towers, and rotating machinery such as turbines and shafts (Felippa, 2004).

Finite element analysis is an extremely powerful tool for the analysis of axisymmetric structures when used correctly. Standard finite element methods have been shown to be capable, in principle, of dealing with any two or three dimensional cases. Nevertheless, the cost of solutions increases greatly with each dimension added. It is therefore always desirable to search for alternatives that may reduce computational efforts. For axisymmetric structures depending on the configuration of external loads, different types of analysis can be identified for simplicity. For example, if also external loads are themselves axisymmetric, the analysis is plane axisymmetric and mathematically two-dimensional. Another situation occurs for an axisymmetric structure under an axisymmetric loading. For example, a cylindrical body under a torsional loading becomes really one-dimensional case. Therefore, the analysis procedure for problems having axial symmetry is very similar to the procedure used for problems of plane stress and plane strain (Zienkiewicz and Taylor, 2000; Benasciutti et al., 2011).

However, in many physical axisymmetrical problems the situation is such that the geometry and material properties do not vary along circumferential coordinate but the loading terms may still exhibit a variation in that direction. Therefore, displacements and stresses are three dimensional rather than axially symmetric. Therefore, the standard plane axisymmetric analysis obviously does not apply in these situations. In such cases, the problem seems to be mathematically three dimensional. However, it is still possible to reduce the problem effectively to a two dimensional problem by expressing the loading in the form of a Fourier series. Finite element equations can be arranged in such a way that the calculations over an element are reduced to those over a two dimensional planar

longitudinal section. Thus, for each loading term in Fourier series expansion the calculations are similar to those for a plane axisymmetric analysis. The complete solution for the original non-axisymmetric loading is obtained by superimposing a reasonable number of solutions for these loading components (Bhatti, 2006; Cook et al., 1989).

Ring finite elements with 4 and 9-noded quadrilateral cross sections to be used for multi purposes such as analyses of shells of revolution, circular beams and plates and axisymmetrical structures subjected to axisymmetric or non-axisymmetric loadings are developed using the displacement based isoparametric formulations and implemented with the appropriate digital computer program, Matlab.

After the verification of the implemented program hyperbolic cooling towers which are large, thin shell reinforced concrete structures which contribute to environmental protection and to power generation efficiency and reliability are analyzed quasi-statically under wind loading and dynamically under earthquake loading. Additionally, free vibration analyses are conducted for cooling towers with different heights, wall thicknesses and curvatures. The results are presented in graphical and tabular formats.

1.2. Literature Review

Many researchers have worked to develop finite element modeling for axisymmetric structures since it has wide range of applications in engineering. Some of studies available in literature for the modeling and analysis of axisymmetric structures or bodies can be summarized as follows:

Viladkar et al. (1998), analyze a cooling tower by representing the tower shell by semi-loof shell elements and the supporting columns by semi-loof beam elements in finite element method. The column ends are assumed to be fixed at their bases. The analysis is carried out for only the dead load. Hoop forces are found to be altered significantly in the lower portion of the shell near the column-shell junction.

Baillis et al. (2000), present a 2D modeling which takes into account reinforced concrete behavior, crack distribution and geometric imperfections based on the Fourier series for rigorous numerical analyses of the behavior of cooling towers.

Kim and Kim (2000), propose a higher order hybrid-mixed C^0 harmonic shell of revolution element. Unlike existing hybrid-mixed shell of revolution elements, they

introduce additional nodeless degrees only for displacement field interpolation in order to enhance the solution convergence rate. They address some fundamental issues such as the effect of the nodeless degrees and the role of the stress field approximation consistent with the displacement field.

Busch et al. (2002), presents an overview over the tower built at the RWE power station at Niederoussem, with 200m elevation the highest cooling tower world-wide. The structural consequences of the flue gas inlets through the shell are explained as well as the needs for an advanced high performance concrete wall and the fill construction. Further, the design and structural analysis of the tower is described with respect to the German codified safety concept for these structures.

Nasir et al. (2002), examines the influence of some geometric parameters such as height and thickness on the free vibration and seismic response of shell structures using three dimensional isotropic shell elements (S4R5) to model the shell in finite element method. This element features five degrees of freedom (three displacement components and two rotations) per node and thus typically models thin shell structures.

Lang et al. (2002), present a shell ring element for the static analysis of shells of revolution of arbitrary shape under arbitrarily distributed loads, based on a displacement formulation that includes geometric and physical non-linearity.

Hong and Teng (2002), present a finite element formulation for the non-linear analysis of elastic doubly curved segmented and branched shells of revolution subjected to arbitrary loads.

Redekop (2004), uses the three-dimensional theory of elasticity to set up accurate solution for the natural frequencies of vibration of a hollow body of revolution of arbitrary geometry. A semi analytical approach is adopted, in which solutions are obtained for specified circumferential harmonic modes of vibration.

Kang and Leissa (2005), present a three dimensional method of analysis for determining the free vibration frequencies and mode shapes of thick, hyperboloidal shells of revolution.

Noorzaei et al. (2006), deals with physical and material modeling of a cooling tower-foundation-soil system. The physical modeling is carried out using solid 20-noded isoparametric element to model the cooling tower, annular raft foundation and soil media. The cooling tower-foundation-soil system is analyzed under vertical and lateral load

generated due to self-weight and wind loads. The soil nonlinearity is taken into consideration using hyperbolic nonlinear elastic constitutive law.

Viladkar (2006), deals with the numerical modeling of a column supported hyperbolic cooling tower and its supporting annular raft-soil system to study its soil-structure interaction response under the influence of symmetrical wind load acting upon it. The soil-structure interaction response of the tower is compared with that of a tower whose supporting columns are treated as fixed at the base.

Jog and Annabattula (2006), present a general procedure for the development of hybrid axisymmetric elements based on the Hellinger-Reissner principle within the context of linear elasticity.

Ahmadian and Bonakdar (2008), present a new 16-node cylindrical superelement. Static and modal analyses of laminated hollow cylinders subjected to various kinds of loading and boundary conditions are performed using this element

Florin and Sunai (2010), explain that from physical point of view, the damping represents the soil seismic excitation energy taken over process through internal absorption, rubbed between existent layers, as cracks on rocky foundations.

Higgins and Basu (2011), analyze laterally loaded piles using the Fourier finite element method which calculate the response of axisymmetric solids subjected to non-axisymmetric loads. The analysis is mostly performed for piles embedded in elastic soil with constant and linearly varying modulus.

1.3. Objectives of This Research

The main objective of the study is to perform the static, modal and dynamic analysis of axisymmetric structures under non-axisymmetric loadings such as wind and earthquake as well as axisymmetric loadings such as internal or external pressure using solid ring harmonic finite elements. A computer program is coded in Matlab for the purpose. Also, the aim of computer programming is to be master of concepts and assumptions behind the coding in commercial computer analysis programs. A verification study is done first by solving several benchmark problems and then the responses of a cooling tower are investigated under dead, wind and earthquake loading.

1.4. Selection of the Model and the Computational Technique

In the field of engineering design we come across many complex problems, the mathematical formulation of which is tedious and usually not possible by analytical methods. At such instants we resort to the use of numerical techniques. The two classical choices which are the most popular for numerical solution are finite difference method (FDM) and finite element method (FEM). Since the FDM is highly difficult to apply for complex geometries, loadings and boundary conditions the finite element method, FEM, is chosen as the powerful tool for getting the numerical solution of a wide range of axisymmetric problems.

In order to reduce the computational efforts plane axisymmetric, plane axisymmetric and harmonic finite element techniques are used in the element formulations for different types of loading for axisymmetric structures. Using these techniques three dimensional problems can be reduced to two dimensional and two dimensional ones to one dimensional. Additionally, one of the model reduction method called as ‘Guyan reduction’ is used in the free vibration and dynamic analysis of axisymmetric structures in order to save time. In free vibration analysis of axisymmetric structures QR inverse iteration technique is used to solve eigenvalue problems. Moreover, static solutions are obtained using Gauss elimination procedures and Newmark direct integration technique is applied in the dynamic analysis.

Detailed information for these numerical and computational methods is presented in the following sections.

1.5. Finite Element Modeling of Axisymmetric Structures

The basic concept in finite element modeling of axisymmetric structures is that the structure is divided into smaller solid ring elements of finite dimensions. In the context of the thesis 4-noded and 9-noded solid ring elements are used and named as Ring4 and Ring9, respectively. The original structure is then considered as an assemblage of these elements connected at a finite number of joints called as nodes. The properties of the elements are formulated and combined to obtain the properties of the entire body. Thus instead of solving the problem for the entire structure in one operation, in the method

attention is mainly devoted to the formulation of properties of the constituent elements. The properties and mathematical formulations of these ring elements are explained in the following sections. Finite element modeling is implemented with appropriate digital computer program, Matlab since it is a computer oriented procedure.

The computer implementation stages of a finite element method for linear static and dynamic analysis of axisymmetric structures using ring elements are preprocessing, processing and post-processing. The preprocessing portion involves the model definition by direct setting of the data structures such as geometry data (node coordinates), element data (connectivity, material, body and surface forces), and degree of freedom data (support boundary conditions). Also, the processing stage performs for the solution of nodal displacements and in post processing stage element stresses are computed.

1.6. Geometry Definitions of Axisymmetric Problems

An axisymmetric object or structure is generated by revolving a plane figure about an axis, and is most easily described in cylindrical coordinates r , θ and z . For these solid objects or structures the geometry is symmetric about the axis around which the plane figure is revolved.

Also, an axisymmetric object or structure can be obtained by revolving an outer curve and an inner curve about a vertical axis as shown in Fig. 1.

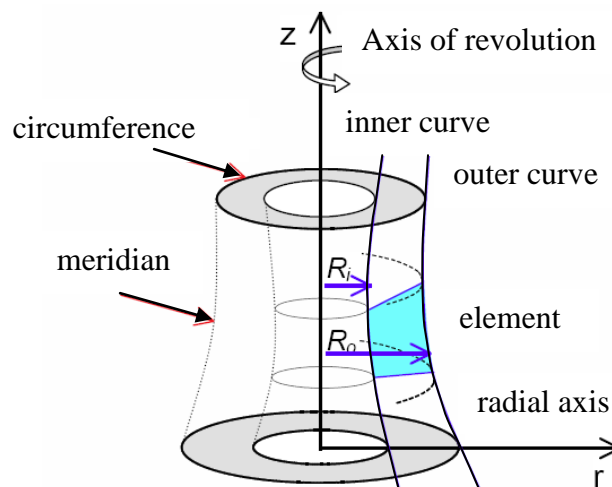


Figure 1. Generators of an axisymmetric object and an element

These curves are the generators of inner and outer surfaces of the revolutionary object. Radial coordinates of the generators are parametrically defined to produce different shapes. The radial coordinates are written as,

$$R_i = \lambda_i \rho_i^{\mu_i} + A_{i4} \quad \text{and} \quad R_o = \lambda_o \rho_o^{\mu_o} + A_{o4} \quad (1)$$

in which λ_i, μ_i and λ_o, μ_o are some constant parameters (i and o denote inner and outer generators respectively) while ρ_i and ρ_o are quadratic functions of the vertical coordinate z . These quadratic functions are defined as,

$$\rho_i = A_{i1} + A_{i2}z + A_{i3}z^2 \quad \text{and} \quad \rho_o = A_{o1} + A_{o2}z + A_{o3}z^2 \quad (2)$$

In these equations, A_{ij} and A_{oj} , where (j=1 to 4), are the parametric constants depending on shapes of generators. These parametric representations of generators can represent almost all practically used revolutionary objects, such as cylindrical, conical, spherical, ellipsoidal, hyperboloidal, paraboloidal, etc. Parameters of these objects are presented in Table 1. r_c and z_c are the coordinates of centers of objects, c_l and m_l are respectively constant and slope of the line, R is the radius of the circular generation, c_1, c_2 and c_3 are constants of the parabola, a and b are lengths of the axes of ellipse and the hyperbola. Beyond these known functions, ρ_i and ρ_o , can be used as generators of revolutionary solid objects (Karadeniz, 2009).

Table 1. Parameters of some practically used revolutionary objects

Generator	λ	μ	A_1	A_2	A_3	A_4
Linear	1	1	c_l	m_l	0	0
Circular	± 1	1/2	$R^2 - z_c^2$	$2z_c$	-1	r_c
Elliptic	$\pm a/b$	1/2	$b^2 - z_c^2$	$2z_c$	-1	r_c
Hyperbolic	$\pm a/b$	1/2	$b^2 + z_c^2$	$-2z_c$	1	r_c
Parabolic	1	1	c_1	c_2	c_2	0

1.7. Element Coordinates and Shape Functions

The elements defined are quadrilateral axisymmetric solid elements. Such elements are called as *ring* elements. These elements are most easily described in cylindrical coordinates r , θ , and z . The coordinate systems and the element nodal numbering rules for the two ring elements are depicted in Fig. 2. Coordinates of any location within the element are calculated using interpolations between nodal coordinates as stated below:

$$r = \sum_{j=1}^b N_j r_j \quad \text{and} \quad z = \sum_{j=1}^b N_j z_j \quad (3)$$

where r_j and z_j ($j=1$ to b) are nodal coordinates, b is the number of nodes and N_j are shape functions or interpolation functions given in Eqs. 4 and 5.

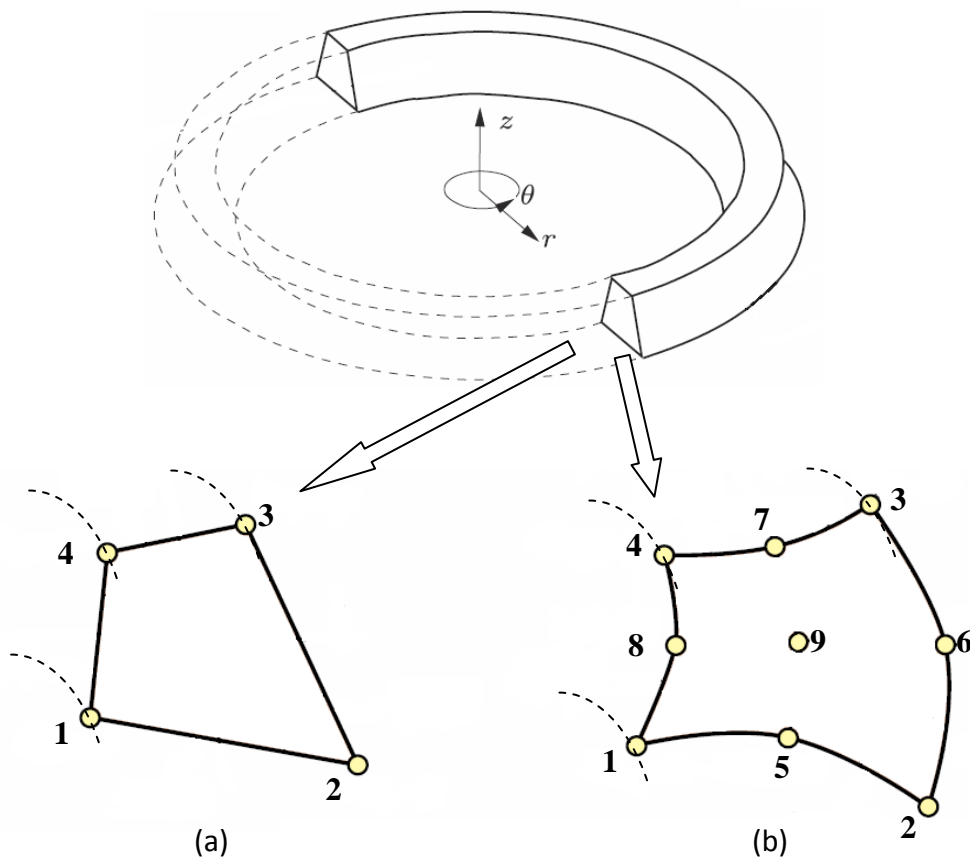


Figure 2. Nodal numbering and global cylindrical coordinate system of (a) 4-node (b) 9-node quadrilateral ring element cross sections

Since the expression of the interpolation functions in terms of the global cylindrical coordinates is algebraically complex (Hutton, 2004) and boundary of integral equations defined over the element volume or area is different for each element due to positional and geometrical configurations, for simplicity, transformation of boundary regions is applied. This procedure is called as mapping of elements. The mapping concept makes finite element computations possible for arbitrary shaped elements (Bhatti, 2006). Therefore, an area transformation is needed from cylindrical coordinates (r, z) to natural coordinates whose master area is a 2×2 square in the ξ and η coordinates as shown in Fig. 3.

In the global coordinate system cylindrical coordinates (r, θ, z) are used to determine the position vector in the element where r, θ, z are radial, tangential and axial coordinates, respectively as shown in Fig. 2. But the element formulation is completely done based on the natural coordinate system which is a local system based on each individual element. The natural coordinate system is shown in Fig. 3 as (ξ, η) .

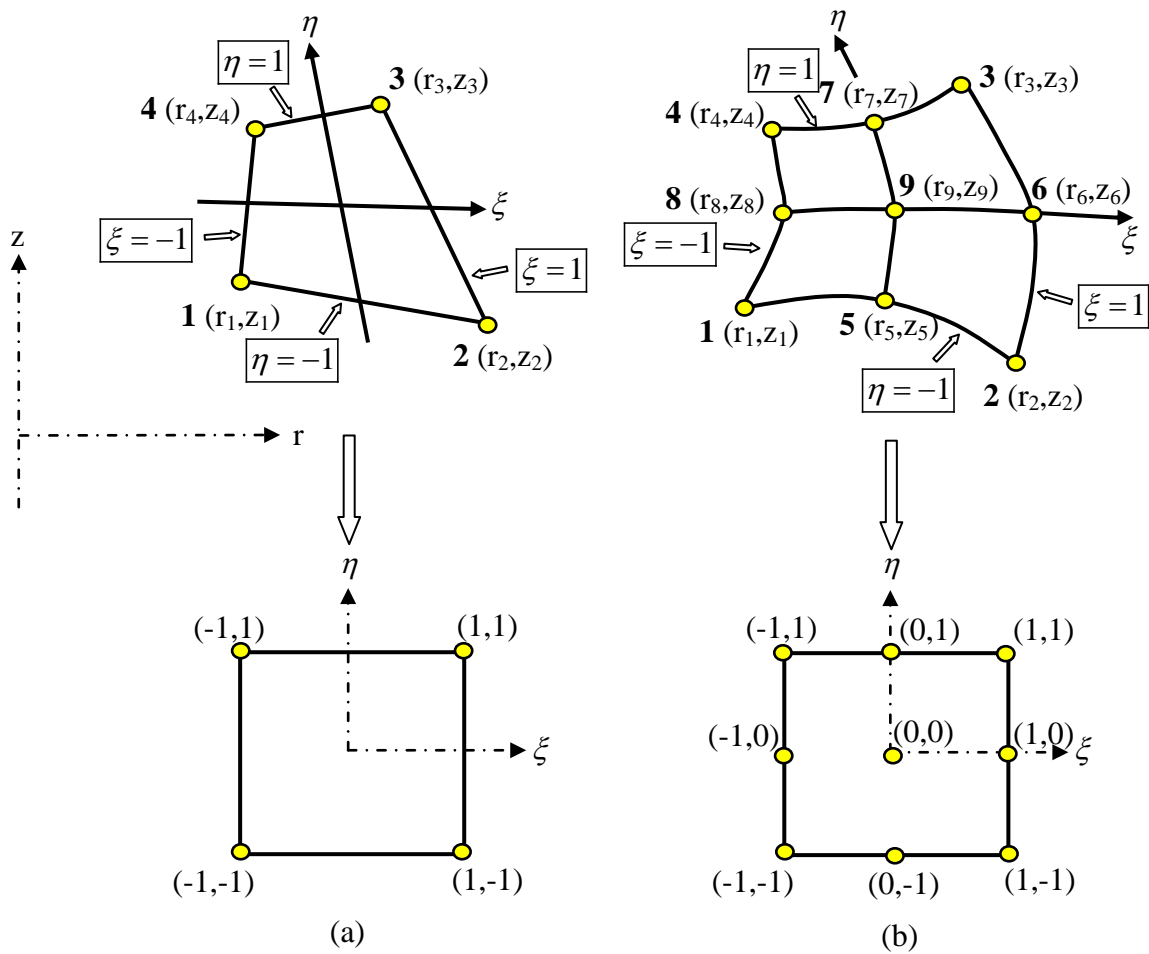


Figure 3. Coordinate transformation of (a) 4-noded (b) 9-noded quadrilateral ring elements

Shape functions for the four-node bilinear quadrilateral ring element are (Cook, 1989):

$$\begin{aligned}
 N_1 &= \frac{1}{4}(1-\xi)(1-\eta) \\
 N_2 &= \frac{1}{4}(1+\xi)(1-\eta) \\
 N_3 &= \frac{1}{4}(1+\xi)(1+\eta) \\
 N_4 &= \frac{1}{4}(1-\xi)(1+\eta)
 \end{aligned} \tag{4}$$

Shape functions for the nine-node biquadratic quadrilateral ring element are:

$$\begin{aligned}
 N_1 &= \frac{1}{4}\xi\eta[(\xi-1)(\eta-1)] \\
 N_2 &= \frac{1}{4}\xi\eta[(\xi+1)(\eta-1)] \\
 N_3 &= \frac{1}{4}\xi\eta[(\xi+1)(\eta+1)] \\
 N_4 &= \frac{1}{4}\xi\eta[(\xi-1)(\eta+1)] \\
 N_5 &= \frac{1}{2}\eta(1-\xi^2)(\eta-1) \\
 N_6 &= \frac{1}{2}\xi(1+\xi)(1-\eta^2) \\
 N_7 &= \frac{1}{2}\eta(1-\xi^2)(1+\eta) \\
 N_8 &= \frac{1}{2}\xi(\xi-1)(1-\eta^2) \\
 N_9 &= (1-\xi^2)(1-\eta^2)
 \end{aligned} \tag{5}$$

Perspective views of some shape functions for particular corner, mid-side and center nodes are shown in Fig. 4.

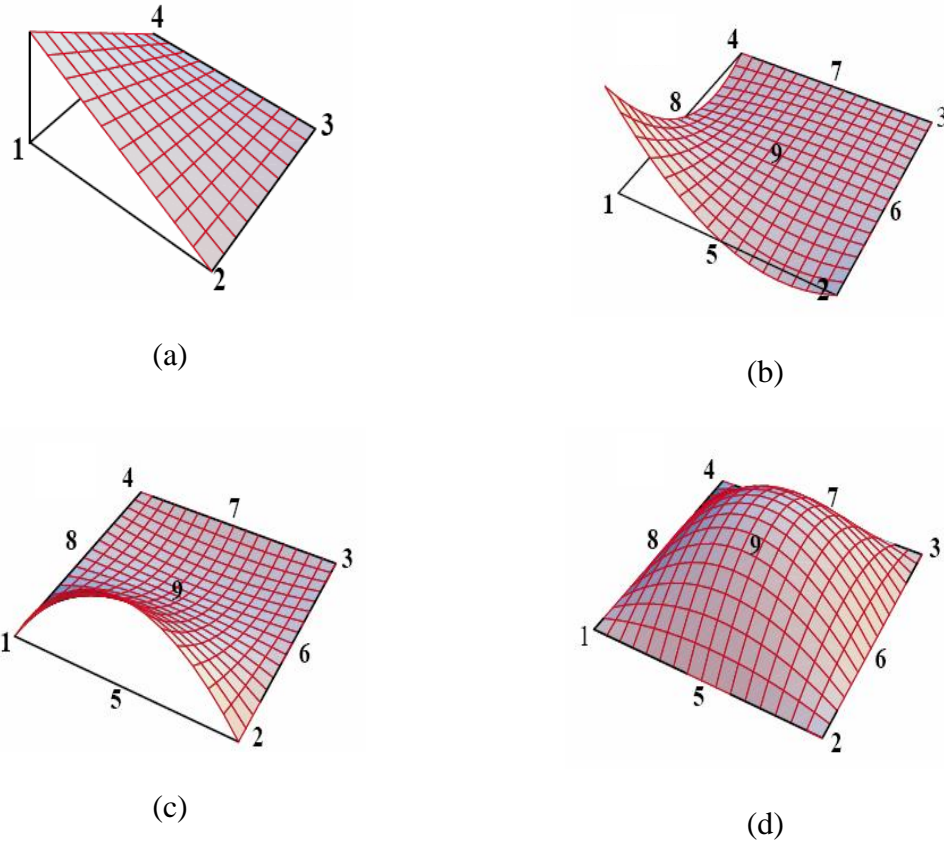


Figure 4. Perspective view of the shape functions for (a) node 1 of the 4-node bilinear quadrilateral ring and (b) node 1 (c) node 5 (d) node 9 of the 9-node biquadratic quadrilateral ring

1.8. Strains and Stresses in an Axisymmetrical Solid Element

The stress (σ) components in an axisymmetric element are shown in Fig. 5. Corresponding stresses (ϵ) are also defined in the same directions and obtained applying stress strain constitutive relationship in Eq. 8.

$$\epsilon = [\epsilon_r \quad \epsilon_\theta \quad \epsilon_z \quad \gamma_{rz} \quad \gamma_{r\theta} \quad \gamma_{\theta z}]^T \text{ and } \sigma = [\sigma_r \quad \sigma_\theta \quad \sigma_z \quad \tau_{rz} \quad \tau_{r\theta} \quad \tau_{\theta z}]^T \quad (6)$$

Having denoted the displacement components u_r , u_θ and u_z in the radial, circumferential or tangential and axial directions respectively, strain components for three dimensional elements in cylindrical coordinates are given by the Eq. 7.

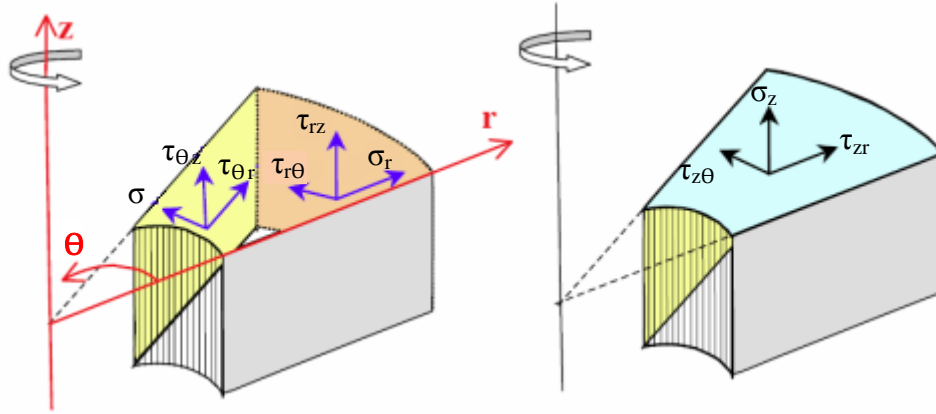


Figure 5. Stress components in an axisymmetrical solid element

$$\{\varepsilon\} = \begin{Bmatrix} \varepsilon_r \\ \varepsilon_\theta \\ \varepsilon_z \\ \gamma_{rz} \\ \gamma_{r\theta} \\ \gamma_{\theta z} \end{Bmatrix} = \begin{Bmatrix} \frac{\partial u_r}{\partial r} \\ \frac{1}{r} \left(u_r + \frac{\partial u_\theta}{\partial \theta} \right) \\ \frac{\partial u_z}{\partial z} \\ \frac{\partial u_z}{\partial r} + \frac{\partial u_r}{\partial z} \\ \frac{1}{r} \frac{\partial u_r}{\partial \theta} + \frac{\partial u_\theta}{\partial r} - \frac{u_\theta}{r} \\ \frac{\partial u_\theta}{\partial z} + \frac{1}{r} \frac{\partial u_z}{\partial \theta} \end{Bmatrix} \quad (7)$$

$$\{\sigma\} = [D]\{\varepsilon\} \quad (8)$$

where $[D]$ is the elasticity matrix given in the following sections.

1.9. Plane Axisymmetric Finite Element

In the case of axisymmetric structures loaded by axially symmetric loads, by symmetry, the two displacement components u_r and u_z in any plane section of the body along its axis of symmetry completely define the state of strain and, accordingly, the state of stress. Thus, the circumferential (hoop) displacement u_θ , the tangential stress components $\tau_{r\theta}$ and $\tau_{\theta z}$ and their corresponding shear strains $\gamma_{r\theta}$ and $\gamma_{\theta z}$ must be zero.

The analysis then reduces to a plane FE model, characterized by only radial $u_r(r, z)$ and axial $u_z(r, z)$ displacements, where r and z denote the radial and axial coordinates of a point within the structure. For an b -node finite element, the vector of displacement field in the cylindrical reference system (r, θ, z) is:

$$\{u\} = \begin{Bmatrix} u_r \\ u_z \end{Bmatrix} = \begin{Bmatrix} \sum_{j=1}^b N_j u_{rj} \\ \sum_{j=1}^b N_j u_{zj} \end{Bmatrix} = [N]\{d\} \quad (9)$$

where u_{rj} , and u_{zj} , ($j=1$ to b), are the nodal values of the of displacements, $\{d\}$ is the nodal displacement vector and $[N]$ is the shape functions matrix, which are defined as written by,

$$\{d\}^T = [\{u\}_1^T \quad \{u\}_2^T \quad \{u\}_3^T \quad \dots \quad \{u\}_b^T] \quad (10)$$

where $\{u\}_j^T$ ($j=1,2,3,\dots,b$) are the nodal displacement vectors of the element.

$$[N] = \begin{bmatrix} N_1 & 0 & N_2 & 0 & \dots & N_b & 0 \\ 0 & N_1 & 0 & N_2 & \dots & 0 & N_b \end{bmatrix} \quad (11)$$

The strain can be stated in a matrix form as

$$\{\varepsilon\} = \begin{Bmatrix} \varepsilon_r \\ \varepsilon_\theta \\ \varepsilon_z \\ \gamma_{rz} \end{Bmatrix} = \begin{Bmatrix} \frac{\partial u_r}{\partial r} \\ \frac{u_r}{r} \\ \frac{\partial u_z}{\partial z} \\ \frac{\partial u_r}{\partial z} + \frac{\partial u_z}{\partial r} \end{Bmatrix} = [L]\{u\} \quad \text{where } [L] = \begin{bmatrix} \frac{\partial}{\partial r} & 0 \\ \frac{1}{r} & 0 \\ 0 & \frac{\partial}{\partial z} \\ \frac{\partial}{\partial z} & \frac{\partial}{\partial r} \end{bmatrix}, \text{ the operator matrix} \quad (12)$$

Inserting Eq. 9 into Eq. 12 yields

$$\{\varepsilon\} = [L][N]\{d\} \quad \text{or} \quad \{\varepsilon\} = [B]\{d\} \quad (13)$$

The matrix $[B]$ is the strain-nodal displacement matrix and defined as (Cook, 1989):

$$[B] = \begin{bmatrix} [B]_{\varepsilon} \\ [B]_{\gamma} \end{bmatrix} = \begin{bmatrix} [B]_{11} & [B]_{12} & \cdots & [B]_{1b} \\ [B]_{21} & [B]_{22} & \cdots & [B]_{2b} \end{bmatrix} \quad (14)$$

where

$$[B]_{1j} = \begin{bmatrix} N_{j,r} & 0 \\ \frac{N_j}{r} & 0 \\ 0 & N_{j,z} \end{bmatrix}, \quad [B]_{2j} = [N_{j,z} \quad N_{j,r}] \quad (j=1, 2, 3, \dots, b) \quad (15)$$

It is seen from the strain-nodal displacement matrix that there are partial derivatives with respect to r and z . However, the shape functions N_i are functions of natural coordinates ξ and η as given in Eqs.4 and 5. Therefore, the transformation of derivatives must be made to natural coordinates. This transformation can be done by Jacobian matrix. The element geometry is defined by $2b$ coordinates $\{r_i, z_i\}$, $i=1,2,3,\dots, b$. These are collected in arrays as

$$r = [r_1 \quad r_2 \quad \dots \quad r_b]^T \quad \text{and} \quad z = [z_1 \quad z_2 \quad \dots \quad z_b]^T \quad (16)$$

By the chain rule, derivatives with respect to r and z can be expressed as

$$\frac{\partial N}{\partial r} = \frac{\partial N}{\partial \xi} \frac{\partial \xi}{\partial r} + \frac{\partial N}{\partial \eta} \frac{\partial \eta}{\partial r} \quad \text{and} \quad \frac{\partial N}{\partial z} = \frac{\partial N}{\partial \xi} \frac{\partial \xi}{\partial z} + \frac{\partial N}{\partial \eta} \frac{\partial \eta}{\partial z} \quad (17)$$

Unfortunately, the partial derivatives of ξ and η with respect to r and z are not directly available from above equations. An inversion is required here as shown below

$$\frac{\partial N}{\partial \xi} = \frac{\partial N}{\partial r} \frac{\partial r}{\partial \xi} + \frac{\partial N}{\partial z} \frac{\partial z}{\partial \xi} \quad \text{and} \quad \frac{\partial N}{\partial \eta} = \frac{\partial N}{\partial r} \frac{\partial r}{\partial \eta} + \frac{\partial N}{\partial z} \frac{\partial z}{\partial \eta} \quad (18)$$

$$\text{or} \quad \begin{Bmatrix} N_{,\xi} \\ N_{,\eta} \end{Bmatrix} = [J] \begin{Bmatrix} N_{,r} \\ N_{,z} \end{Bmatrix} \quad (19)$$

where $[J]$ is called as Jacobian matrix and in expanded form it is

$$[J] = \begin{bmatrix} \frac{\partial r}{\partial \xi} & \frac{\partial z}{\partial \xi} \\ \frac{\partial r}{\partial \eta} & \frac{\partial z}{\partial \eta} \end{bmatrix} = \begin{bmatrix} J_{11} & J_{12} \\ J_{21} & J_{22} \end{bmatrix} = \begin{bmatrix} N_{,\xi} r & N_{,\xi} z \\ N_{,\eta} r & N_{,\eta} z \end{bmatrix} \quad (20)$$

Finally, the derivatives of shape functions with respect to r and z can be obtained with respect to natural coordinates as

$$\begin{Bmatrix} N_{,r} \\ N_{,z} \end{Bmatrix} = [\Gamma] \begin{Bmatrix} N_{,\xi} \\ N_{,\eta} \end{Bmatrix} \text{ where } [\Gamma] = \begin{bmatrix} \Gamma_{11} & \Gamma_{12} \\ \Gamma_{21} & \Gamma_{22} \end{bmatrix} = [J]^{-1} = \frac{1}{J} \begin{bmatrix} J_{22} & -J_{12} \\ -J_{21} & J_{11} \end{bmatrix} \quad (21)$$

where J is the determinant of the Jacobian matrix, which can be regarded as a scale factor that yields area $drdz$ from $d\xi d\eta$, given as

$$J = \det[J] = J_{11}J_{22} - J_{21}J_{12} \quad (22)$$

Eq. 20 is valid for all plane isoparametric elements. Partial derivatives in the strain-nodal displacement matrix are obtained with respect to natural coordinates and can be easily implemented into the Gauss numerical integration procedures. The stress vector for a plane axisymmetric problem in the cylindrical coordinate system is related to the strain vector through the constitutive relationship for an isotropic material as follows (Bhatti, 2006):

$$\begin{Bmatrix} \sigma_r \\ \sigma_\theta \\ \sigma_z \\ \tau_{rz} \end{Bmatrix} = [D] \begin{Bmatrix} \varepsilon_r \\ \varepsilon_\theta \\ \varepsilon_z \\ \gamma_{rz} \end{Bmatrix} \quad (23)$$

in which $[D]$ is the material property matrix, which links the vectors of strains and stresses, in the hypothesis of isotropic material has the following form:

$$[D] = \begin{bmatrix} [E_\varepsilon] & 0 \\ 0 & [E_\gamma] \end{bmatrix} \quad (24)$$

$$[E_\varepsilon] = \frac{E}{(1+\nu)(1-2\nu)} \begin{bmatrix} 1-\nu & \nu & \nu \\ \nu & 1-\nu & \nu \\ \nu & \nu & 1-\nu \end{bmatrix} \text{ and } [E_\gamma] = \frac{E}{2(1+\nu)} \quad (25)$$

where E and ν are modulus of elasticity and Poisson's ratio, respectively.

1.10. Plane Axi-antisymmetric Finite Element

An interesting application is represented by the study of axisymmetric structures subjected to axi-antisymmetric loadings. An example is a shaft of variable diameter under a torsion load applied at the ends (Timoshenko and Goodier, 1951). In this configuration, load is antisymmetric with respect to each plane crossing z -axis and it is also independent of angle θ . In fact, in this configuration each node has only one degree of freedom (the hoop displacement u_θ), while radial and axial displacements u_r and u_z (warping), as well as normal stresses $\sigma_r, \sigma_\theta, \sigma_z$, shear stress τ_{rz} and their related strain components vanish. By symmetry, the hoop displacement does not depend on angle θ and only two non-null strains $\gamma_{r\theta}$ and $\gamma_{\theta z}$ are present. By analogy with Eq. 9, the displacement of a point within an b -node element is:

$$u_\theta(r, z) = \sum_{j=1}^b N_j u_{\theta j} = [N]\{d\} \quad (26)$$

where $u_{\theta j}$, ($j=1$ to b), are the nodal values of the displacements, $\{d\}$ is the nodal displacement vector and $[N]$ is the shape functions matrix, which are expressed as:

$$\{d\}^T = [u_{\theta 1} \quad u_{\theta 2} \quad u_{\theta 3} \quad \dots \dots \dots u_{\theta n}] \quad (27)$$

$$[N] = [N_1(r, z) \quad N_2(r, z) \quad \dots \dots \quad N_n(r, z)] \quad (28)$$

The strain can be stated in a vector form as

$$\{\varepsilon\} = \begin{Bmatrix} \gamma_{r\theta} \\ \gamma_{\theta z} \end{Bmatrix} = \begin{Bmatrix} \frac{\partial u_\theta}{\partial r} - \frac{u_\theta}{r} \\ \frac{\partial u_\theta}{\partial z} \end{Bmatrix} = [L]u_\theta(r, z) \text{ where } [L] = \begin{bmatrix} \frac{\partial}{\partial r} - \frac{1}{r} \\ \frac{\partial}{\partial z} \end{bmatrix} \quad (29)$$

Substituting Eq. 26 into Eq. 29 produces the followings:

$$\{\varepsilon\} = [B]\{d\} \text{ and } [B] = [L][N] \quad (30)$$

$$[B] = [[B]_1 \quad [B]_2 \quad \dots \quad [B]_n] \text{ where } [B]_j = \begin{bmatrix} (N_{j,r} - \frac{N_j}{r}) \\ N_{j,z} \end{bmatrix}, (j=1, 2, 3 \dots n) \quad (31)$$

Jacobian matrix obtained in plane axisymmetric case is also valid in this case to transform shape function derivatives from global coordinates to natural coordinates. Similar to Eq. 23 the stress- strain relationship for an axi-antisymmetric problem can be expressed as

$$\begin{Bmatrix} \tau_{r\theta} \\ \tau_{\theta z} \end{Bmatrix} = [D] \begin{Bmatrix} \gamma_{r\theta} \\ \gamma_{\theta z} \end{Bmatrix} \quad (32)$$

$$[D] = \frac{E}{2(1+\nu)} \begin{bmatrix} 1 & 0 \\ 0 & 1 \end{bmatrix} \quad (33)$$

1.11. Harmonic Finite Element

A third type of problem, of more practical interest, is when the structure is axially symmetric but the loading is not, so that the analysis is really three dimensional. A great simplification can be obtained by using a semi-analytical approach, based on a harmonic finite element model and Fourier series expansion of loads. As it will be shown, in linear analysis, a harmonic load produces a harmonic response in terms of stress and displacements. The solution is then obtained by superimposing results of each harmonic (Cook et al., 1989; Zienkiewicz and Taylor, 2000).

To start with, the nodal loads applied to the structure can be expanded in Fourier series which will be explained later on as:

$$\{q\} = \begin{Bmatrix} q_r(r, \theta, z) \\ q_\theta(r, \theta, z) \\ q_z(r, \theta, z) \end{Bmatrix} = \begin{Bmatrix} \bar{q}_{r0} + \sum_{m=1}^{\infty} \left(\bar{q}_{rm}(r, z) \cos m\theta + \bar{q}_{rm}(r, z) \sin m\theta \right) \\ \bar{q}_{\theta0} + \sum_{m=1}^{\infty} \left(\bar{q}_{\theta m}(r, z) \sin m\theta - \bar{q}_{\theta m}(r, z) \cos m\theta \right) \\ \bar{q}_{z0} + \sum_{m=1}^{\infty} \left(\bar{q}_{zm}(r, z) \cos m\theta + \bar{q}_{zm}(r, z) \sin m\theta \right) \end{Bmatrix} \quad (34)$$

in which m is the circumferential mode (harmonic) number and symbols q_r , q_θ and q_z indicate the radial, hoop and axial load components, respectively. In Eq. 34 all barred quantities are amplitudes, which are functions of r , z but not of θ . Single barred amplitudes represent symmetric load components (loads which have $\theta = 0$ as a plane of symmetry), while double barred amplitudes represent antisymmetric load terms. The sine expansion in q_θ load is necessary to ensure symmetry, as the direction of q_θ has to change for $\theta > \pi$. The constant terms \bar{q}_{r0} and \bar{q}_{z0} permit axisymmetric load condition to be described, while the term $\bar{q}_{\theta0}$ refers to the axi-antisymmetric load. It is possible to demonstrate (Cook et al., 1989) that in a linear analysis, when the loads are expanded as in Eq. 34, displacement components are described by Fourier series as well:

$$\{u\} = \begin{Bmatrix} u_r(r, \theta, z) \\ u_\theta(r, \theta, z) \\ u_z(r, \theta, z) \end{Bmatrix} = \begin{Bmatrix} \sum_{m=0}^{\infty} \bar{u}_{rm} \cos m\theta + \sum_{m=0}^{\infty} \bar{u}_{rm} \sin m\theta \\ \sum_{m=0}^{\infty} \bar{u}_{\theta m} \sin m\theta - \sum_{m=0}^{\infty} \bar{u}_{\theta m} \cos m\theta \\ \sum_{m=0}^{\infty} \bar{u}_{zm} \cos m\theta + \sum_{m=0}^{\infty} \bar{u}_{zm} \sin m\theta \end{Bmatrix} \quad (35)$$

All three displacements are needed because the physical problem is three dimensional. The motivation of the arbitrarily chosen negative sign in the u_θ series is that it greatly simplifies the computation of the element stiffness matrix, as it will be explained later on. As for the loads, the single and double barred terms refer to amplitudes of symmetric and

antisymmetric displacement components. A Fourier series expansion similar to Eq. 35 can be equally used also for the nodal displacements of a finite element. Within a finite element, one can thus interpolate the amplitudes \bar{u}_{rm} , $\bar{u}_{\theta m}$, \bar{u}_{zm} , etc. of the displacements components in Eq. 35 from the corresponding nodal amplitudes (\bar{u}_{rim} , $\bar{u}_{\theta im}$, \bar{u}_{zim}), where subscript im specifies that amplitude refers to node i and harmonic m . Therefore, the vector of displacement field within the element can be described in the following form:

$$\{u\} = \begin{Bmatrix} u_r \\ u_\theta \\ u_z \end{Bmatrix} = \sum_{m=0}^{\infty} \sum_{i=1}^b N_i(r, z) \left[\overline{g_{\theta m}} \right]_u \{ \bar{u}_{im} \} + \sum_{m=0}^{\infty} \sum_{i=1}^b N_i(r, z) \left[\overline{\overline{g_{\theta m}}} \right]_u \{ \bar{\bar{u}}_{im} \} \quad (36)$$

where the harmonic functions for harmonic m

$$\left[\overline{g_{\theta m}} \right]_u = \begin{bmatrix} \cos m\theta & 0 & 0 \\ 0 & \sin m\theta & 0 \\ 0 & 0 & \cos m\theta \end{bmatrix} \quad (37)$$

and

$$\left[\overline{\overline{g_{\theta m}}} \right]_u = \begin{bmatrix} \sin m\theta & 0 & 0 \\ 0 & -\cos m\theta & 0 \\ 0 & 0 & \sin m\theta \end{bmatrix} \quad (38)$$

$$\{ \bar{u}_{im} \} = \begin{Bmatrix} \bar{u}_{rim} \\ \bar{u}_{\theta im} \\ \bar{u}_{zim} \end{Bmatrix} \quad \text{and} \quad \{ \bar{\bar{u}}_{im} \} = \begin{Bmatrix} \bar{\bar{u}}_{rim} \\ \bar{\bar{u}}_{\theta im} \\ \bar{\bar{u}}_{zim} \end{Bmatrix} \quad (39)$$

Also it can be expressed as:

$$\{u\} = \begin{Bmatrix} u_r(r, \theta, z) \\ u_\theta(r, \theta, z) \\ u_z(r, \theta, z) \end{Bmatrix} = \sum_{m=0}^{\infty} \left(\left[\overline{g_{\theta m}} \right]_u [N] \{ \bar{d}_m \} + \left[\overline{\overline{g_{\theta m}}} \right]_u [N] \{ \bar{\bar{d}}_m \} \right) \quad (40)$$

where $\{\bar{d}\}_m$ and $\{\bar{\bar{d}}\}_m$ are the nodal displacement vectors for the Fourier term (mode) m and $[N]$ is the shape functions matrix, which are defined as written by,

$$\begin{aligned} \{\bar{d}\}_m &= \left[\{\bar{u}_{1m}\}^T \quad \{\bar{u}_{2m}\}^T \quad \dots \quad \{\bar{u}_{bm}\}^T \right]^T \\ \{\bar{\bar{d}}\}_m &= \left[\{\bar{\bar{u}}_{1m}\}^T \quad \{\bar{\bar{u}}_{2m}\}^T \quad \dots \quad \{\bar{\bar{u}}_{bm}\}^T \right]^T \end{aligned} \quad (41)$$

$$[N] = [[N]_1 \quad [N]_2 \quad \dots \quad [N]_b] \quad \text{where} \quad [N]_i = \begin{bmatrix} N_i & 0 & 0 \\ 0 & N_i & 0 \\ 0 & 0 & N_i \end{bmatrix} \quad (42)$$

The strain vector can be expressed as:

$$\{\varepsilon\} = [L]\{u\} = \sum_{m=0}^{\infty} \left([\bar{B}]_m \{\bar{d}\}_m + [\bar{\bar{B}}]_m \{\bar{\bar{d}}\}_m \right) \quad (43)$$

where $[L]$ is the differential operator matrix, with dimension 6x3 as given below:

$$[L] = \begin{bmatrix} [L]_1 \\ [L]_2 \end{bmatrix} \quad (44)$$

where

$$[L]_1 = \begin{bmatrix} \frac{\partial}{\partial r} & 0 & 0 \\ \frac{1}{r} & \frac{\partial}{(r\partial\theta)} & 0 \\ 0 & 0 & \frac{\partial}{\partial z} \end{bmatrix} \quad \text{and} \quad [L]_2 = \begin{bmatrix} \frac{\partial}{\partial z} & 0 & \frac{\partial}{\partial r} \\ \frac{\partial}{(r\partial\theta)} & \left(\frac{\partial}{\partial r} - \frac{1}{r}\right) & 0 \\ 0 & \frac{\partial}{\partial z} & \frac{\partial}{(r\partial\theta)} \end{bmatrix}$$

Therefore, also strains are expanded in Fourier series and the contribution of m^{th} harmonic thus is:

$$\{\varepsilon\}_m = \left(\{\bar{\varepsilon}\}_m + \{\bar{\bar{\varepsilon}}\}_m \right) = \left([\bar{B}]_m \{\bar{d}\}_m + [\bar{\bar{B}}]_m \{\bar{\bar{d}}\}_m \right) \quad (45)$$

Eq. 45 defines, for harmonic m , the strain displacement matrices as follows:

$$\begin{bmatrix} \overline{B} \end{bmatrix}_m = \begin{bmatrix} \overline{g_{\theta m}} \end{bmatrix} [B]_m = \begin{bmatrix} \overline{g_{\theta m}} \end{bmatrix} \begin{bmatrix} [B_m]_{\varepsilon} \\ [B_m]_{\gamma} \end{bmatrix} = \begin{bmatrix} \overline{g_{\theta m}} \end{bmatrix} \begin{bmatrix} [B]_{11m} & [B]_{12m} & \cdots & [B]_{1bm} \\ [B]_{21m} & [B]_{22m} & \cdots & [B]_{2bm} \end{bmatrix} \quad (46)$$

$$\begin{bmatrix} \overline{\overline{B}} \end{bmatrix}_m = \begin{bmatrix} \overline{\overline{g_{\theta m}}} \end{bmatrix} [B]_m = \begin{bmatrix} \overline{\overline{g_{\theta m}}} \end{bmatrix} \begin{bmatrix} [B_m]_{\varepsilon} \\ [B_m]_{\gamma} \end{bmatrix} = \begin{bmatrix} \overline{\overline{g_{\theta m}}} \end{bmatrix} \begin{bmatrix} [B]_{11m} & [B]_{12m} & \cdots & [B]_{1bm} \\ [B]_{21m} & [B]_{22m} & \cdots & [B]_{2bm} \end{bmatrix} \quad (47)$$

where the matrices $\begin{bmatrix} \overline{g_{\theta m}} \end{bmatrix}$ and $\begin{bmatrix} \overline{\overline{g_{\theta m}}} \end{bmatrix}$ of the harmonic functions for the harmonic m are:

$$\begin{bmatrix} \overline{g_{\theta m}} \end{bmatrix} = [L] \begin{bmatrix} \overline{g_{\theta m}} \end{bmatrix}_u = \begin{bmatrix} \begin{bmatrix} \overline{g_{\theta m}} \end{bmatrix}_{\varepsilon} & 0 \\ 0 & \begin{bmatrix} \overline{g_{\theta m}} \end{bmatrix}_{\gamma} \end{bmatrix} \quad (48)$$

and

$$\begin{bmatrix} \overline{\overline{g_{\theta m}}} \end{bmatrix} = [L] \begin{bmatrix} \overline{\overline{g_{\theta m}}} \end{bmatrix}_u = \begin{bmatrix} \begin{bmatrix} \overline{\overline{g_{\theta m}}} \end{bmatrix}_{\varepsilon} & 0 \\ 0 & \begin{bmatrix} \overline{\overline{g_{\theta m}}} \end{bmatrix}_{\gamma} \end{bmatrix} \quad (49)$$

where

$$\begin{bmatrix} \overline{g_{\theta m}} \end{bmatrix}_{\varepsilon} = \cos m\theta \begin{bmatrix} 1 & 0 & 0 \\ 0 & 1 & 0 \\ 0 & 0 & 1 \end{bmatrix} \quad (50)$$

$$\begin{bmatrix} \overline{g_{\theta m}} \end{bmatrix}_{\gamma} = \begin{bmatrix} \cos m\theta & 0 & 0 \\ 0 & \sin m\theta & 0 \\ 0 & 0 & \sin m\theta \end{bmatrix} \quad (51)$$

$$\begin{bmatrix} \overline{\overline{g_{\theta m}}} \end{bmatrix}_{\varepsilon} = \sin(m\theta) \begin{bmatrix} 1 & 0 & 0 \\ 0 & 1 & 0 \\ 0 & 0 & 1 \end{bmatrix} \quad (52)$$

$$\left[\overline{\overline{g_{\theta m}}} \right]_{\gamma} = \begin{bmatrix} \sin m\theta & 0 & 0 \\ 0 & -\cos m\theta & 0 \\ 0 & 0 & -\cos m\theta \end{bmatrix} \quad (53)$$

and for the i^{th} node, submatrices are given as:

$$[B]_{1im} = \begin{bmatrix} N_{i,r} & 0 & 0 \\ \frac{N_i}{r} & \frac{mN_i}{r} & 0 \\ 0 & 0 & N_{i,z} \end{bmatrix} \quad (54)$$

$$[B]_{2im} = \begin{bmatrix} N_{i,z} & 0 & N_{i,r} \\ -\frac{mN_i}{r} & (N_{i,r} - \frac{N_i}{r}) & 0 \\ 0 & N_{j,z} & -\frac{mN_i}{r} \end{bmatrix} \quad (55)$$

and complete forms of strain displacement matrices for the i^{th} node can be expressed as:

$$[\overline{B}]_{im} = \begin{bmatrix} N_{i,r} \cos m\theta & 0 & 0 \\ \frac{N_i}{r} \cos m\theta & \frac{mN_i}{r} \cos m\theta & 0 \\ 0 & 0 & N_{i,z} \cos m\theta \\ N_{i,z} \cos m\theta & 0 & N_{i,r} \cos m\theta \\ -\frac{mN_i}{r} \sin m\theta & (N_{i,r} - \frac{N_i}{r}) \sin m\theta & 0 \\ 0 & N_{i,z} \sin m\theta & -\frac{mN_i}{r} \sin m\theta \end{bmatrix} \quad (56)$$

and

$$\left[\overline{\overline{B}} \right]_{im} = \begin{bmatrix} N_{i,r} \sin m\theta & 0 & 0 \\ \frac{N_i}{r} \sin m\theta & \frac{mN_i}{r} \sin m\theta & 0 \\ 0 & 0 & N_{i,z} \sin m\theta \\ N_{i,z} \sin m\theta & 0 & N_{i,r} \sin m\theta \\ \frac{mN_i}{r} \cos m\theta & \left(\frac{N_i}{r} - N_{i,r} \right) \cos m\theta & 0 \\ 0 & -N_{i,z} \cos m\theta & \frac{mN_i}{r} \cos m\theta \end{bmatrix} \quad (57)$$

It can be seen from $\left[\overline{g_{\theta m}} \right]$ and $\left[\overline{\overline{g_{\theta m}}} \right]$ that $\sin m\theta$ and $\cos m\theta$ are interchanged and, in addition, there is an algebraic sign change in the last two rows of $\left[\overline{\overline{g_{\theta m}}} \right]$, that is to say $\left[\overline{\overline{B}} \right]_{im}$ can be obtained from that of $\left[\overline{B} \right]_{im}$ by simply substituting $(-\sin m\theta)$ with $(\cos m\theta)$ and $\cos m\theta$ with $\sin m\theta$. Shape functions depend on ξ and η . Therefore, strain displacement matrices are functions of ξ, η, θ , and m . The usual transformation of derivatives from global coordinates to natural coordinates can be made as:

$$N_{i,r} = \Gamma_{11}N_{i,\xi} + \Gamma_{12}N_{i,\eta} \quad \text{and} \quad N_{i,z} = \Gamma_{21}N_{i,\xi} + \Gamma_{22}N_{i,\eta} \quad (58)$$

where the matrix $[\Gamma]$ is as defined in Eq. 21 in the plane axisymmetric finite element section. The stress vector for the m^{th} harmonic in the cylindrical coordinate system related to the strain vector through the constitutive equations is given for an isotropic material as follows (Bhatti, 2006):

$$\left\{ \begin{array}{c} \overline{\sigma}_{rm} \\ \overline{\sigma}_{\theta m} \\ \overline{\sigma}_{zm} \\ \overline{\tau}_{rzm} \\ \overline{\tau}_{r\theta m} \\ \overline{\tau}_{\theta zm} \end{array} \right\} = [D] \left\{ \begin{array}{c} \overline{\varepsilon}_{rm} \\ \overline{\varepsilon}_{\theta m} \\ \overline{\varepsilon}_{zm} \\ \overline{\gamma}_{rzm} \\ \overline{\gamma}_{r\theta m} \\ \overline{\gamma}_{\theta zm} \end{array} \right\}, \quad \{\overline{\sigma}\}_m = [D]\{\overline{\varepsilon}\}_m \quad (59)$$

in which $[D]$ is the material property matrix for isotropic material given by the following equation where E and ν are as defined before.

$$[D] = \begin{bmatrix} [E_\varepsilon] & 0 \\ 0 & [E_\gamma] \end{bmatrix} \quad (60)$$

where $[E_\varepsilon]$ is given in Eq. 25 and

$$[E_\gamma] = \frac{E}{2(1+\nu)} \begin{bmatrix} 1 & 0 & 0 \\ 0 & 1 & 0 \\ 0 & 0 & 1 \end{bmatrix} \quad (61)$$

1.12. Element Stiffness Matrix

The element stiffness matrix of a ring element, which is used in the analyses of axisymmetric structures in the content of the thesis, is based on displacement fields. The stiffness matrix of a linear system is calculated from the derivation of the strain energy of an axisymmetrical solid element (Karadeniz, 2009). The strain energy is expressed for one element as:

$$U_e = \frac{1}{2} \int \{\varepsilon\}^T \{\sigma\} dV \quad (62)$$

Now to obtain element stiffness matrix an interpolation scheme must be substituted into the strain energy expression. Substitution of Eq. 8 and Eq. 13 into strain energy expression yields the following:

$$U_e = \frac{1}{2} \int \{d\}^T [B]^T [D] [B] \{d\} dV = \frac{1}{2} \{d\}^T [k] \{d\} \quad (63)$$

and the element stiffness matrix can be obtained from Eq. 63 as

$$[k] = \int [B]^T [D] [B] dV = \int_{A_e} \int_0^{2\pi} [B]^T [D] [B] r d\theta dA \quad (64)$$

The element stiffness matrix is calculated as an integral over the element volume, which for axial symmetry coincides with the whole ring of material. A_e is the cross-sectional area of the element on a plane section. It is necessary to find out the element stiffness matrix for each Fourier harmonics for the analysis. Therefore, we have to express the strain-nodal displacement matrix for each harmonic in Eq. 64 as:

$$[B] = \sum_{m=0}^{\infty} \left[\overline{[g_{\theta m}]} [B]_m + \overline{\overline{[g_{\theta m}]} [B]_m} \right] \quad (65)$$

So two stiffness matrices $[\overline{k}_m]$ and $[\overline{\overline{k}}_m]$ have to be defined according to Eq. 64 for both single and double barred terms in Fourier series expansion:

$$[\overline{k}_m] = \iint [B_m]^T \left(\int_0^{2\pi} \begin{bmatrix} \overline{[g_{\theta m}]}_{\varepsilon}^T [E_{\varepsilon}] \overline{[g_{\theta m}]}_{\varepsilon} & 0 \\ 0 & \overline{[g_{\theta m}]}_{\gamma}^T [E_{\gamma}] \overline{[g_{\theta m}]}_{\gamma} \end{bmatrix} d\theta \right) [B_m] r dr dz \quad (66)$$

$$[\overline{\overline{k}}_m] = \iint [B_m]^T \left(\int_0^{2\pi} \begin{bmatrix} \overline{\overline{[g_{\theta m}]}_{\varepsilon}}^T [E_{\varepsilon}] \overline{\overline{[g_{\theta m}]}_{\varepsilon}} & 0 \\ 0 & \overline{\overline{[g_{\theta m}]}_{\gamma}}^T [E_{\gamma}] \overline{\overline{[g_{\theta m}]}_{\gamma}} \end{bmatrix} d\theta \right) [B_m] r dr dz \quad (67)$$

It can be observed that each term in the products of $\overline{[g_{\theta m}]}_{\varepsilon}^T [E_{\varepsilon}] \overline{[g_{\theta m}]}_{\varepsilon}$, $\overline{[g_{\theta m}]}_{\gamma}^T [E_{\gamma}] \overline{[g_{\theta m}]}_{\gamma}$, $\overline{\overline{[g_{\theta m}]}_{\varepsilon}}^T [E_{\varepsilon}] \overline{\overline{[g_{\theta m}]}_{\varepsilon}}$, $\overline{\overline{[g_{\theta m}]}_{\gamma}}^T [E_{\gamma}] \overline{\overline{[g_{\theta m}]}_{\gamma}}$ will be a function of (E, ν) multiplied by either $\cos^2 m\theta$ or $\sin^2 m\theta$. Thus, integration over the

circumferential direction θ can be carried out explicitly using the following orthogonality property of trigonometric functions when integrated from 0 to 2π :

$$\int_0^{2\pi} \cos^2(m\theta) d\theta = \begin{cases} \pi & \text{for } m > 0 \\ 2\pi & \text{for } m = 0 \end{cases} \quad (68)$$

$$\int_0^{2\pi} \sin^2(m\theta) d\theta = \begin{cases} \pi & \text{for } m > 0 \\ 0 & \text{for } m = 0 \end{cases} \quad (69)$$

Then,

$$\left. \begin{aligned} \int_0^{2\pi} \left[\overline{g_{\theta m}} \right]_{\varepsilon}^T [E_{\varepsilon}] \left[\overline{g_{\theta m}} \right]_{\varepsilon} d\theta &= \pi [E_{\varepsilon}] \\ \int_0^{2\pi} \left[\overline{g_{\theta m}} \right]_{\gamma}^T [E_{\gamma}] \left[\overline{g_{\theta m}} \right]_{\gamma} d\theta &= \pi [E_{\gamma}] \end{aligned} \right\} \text{if } m > 0 \quad (70)$$

$$\left. \begin{aligned} \int_0^{2\pi} \left[\overline{g_{\theta m}} \right]_{\varepsilon}^T [E_{\varepsilon}] \left[\overline{g_{\theta m}} \right]_{\varepsilon} d\theta &= 2\pi \begin{bmatrix} 1 & 0 & 0 \\ 0 & 1 & 0 \\ 0 & 0 & 1 \end{bmatrix} [E_{\varepsilon}] = 2\pi [\overline{E}_{\varepsilon 0}] \\ \int_0^{2\pi} \left[\overline{g_{\theta m}} \right]_{\gamma}^T [E_{\gamma}] \left[\overline{g_{\theta m}} \right]_{\gamma} d\theta &= 2\pi \begin{bmatrix} 1 & 0 & 0 \\ 0 & 0 & 0 \\ 0 & 0 & 0 \end{bmatrix} [E_{\gamma}] = 2\pi [\overline{E}_{\gamma 0}] \end{aligned} \right\} \text{if } m = 0 \quad (71)$$

$$\left. \begin{aligned} \int_0^{2\pi} \left[\overline{\overline{g_{\theta m}}} \right]_{\varepsilon}^T [E_{\varepsilon}] \left[\overline{\overline{g_{\theta m}}} \right]_{\varepsilon} d\theta &= \pi [E_{\varepsilon}] \\ \int_0^{2\pi} \left[\overline{\overline{g_{\theta m}}} \right]_{\gamma}^T [E_{\gamma}] \left[\overline{\overline{g_{\theta m}}} \right]_{\gamma} d\theta &= \pi [E_{\gamma}] \end{aligned} \right\} \text{if } m > 0 \quad (72)$$

$$\left. \begin{aligned} \int_0^{2\pi} \left[\overline{\overline{g_{\theta m}}} \right]_{\varepsilon}^T [E_{\varepsilon}] \left[\overline{\overline{g_{\theta m}}} \right]_{\varepsilon} d\theta &= 2\pi \begin{bmatrix} 0 & 0 & 0 \\ 0 & 0 & 0 \\ 0 & 0 & 0 \end{bmatrix} [E_{\varepsilon}] = 2\pi [\overline{\overline{E}}_{\varepsilon 0}] \\ \int_0^{2\pi} \left[\overline{\overline{g_{\theta m}}} \right]_{\gamma}^T [E_{\gamma}] \left[\overline{\overline{g_{\theta m}}} \right]_{\gamma} d\theta &= 2\pi \begin{bmatrix} 0 & 0 & 0 \\ 0 & 1 & 0 \\ 0 & 0 & 1 \end{bmatrix} [E_{\gamma}] = 2\pi [\overline{\overline{E}}_{\gamma 0}] \end{aligned} \right\} \text{if } m = 0 \quad (73)$$

The integration results in a factor π that multiplies each term for each Fourier series harmonics except for zeroth ($m=0$) harmonic. For zeroth harmonic the factor will be 2π for the integration. It should also be mentioned that, due to choice of negative sign in the second expression in Eq. 35, the stiffness matrix for double barred terms is identical to that of single barred terms, that is $[\bar{k}_m] = [\bar{\bar{k}}_m] = [k_m]$ for $m>0$. Additionally, $[\bar{k}_0]$ and $[\bar{\bar{k}}_0]$ can be used for particular cases of plane axisymmetric and plane axi-antisymmetric cases respectively. So, for the m^{th} harmonic the stiffness matrices are obtained from the following expressions as:

$$[\bar{k}_0] = 2\pi \iint \left([B_0]_{\varepsilon}^T [\bar{E}_{\varepsilon 0}] [B_0]_{\varepsilon} + [B_0]_{\gamma}^T [\bar{E}_{\gamma 0}] [B_0]_{\gamma} \right) r dr dz \quad (74)$$

$$[\bar{\bar{k}}_0] = 2\pi \iint \left([B_0]_{\varepsilon}^T [\bar{\bar{E}}_{\varepsilon 0}] [B_0]_{\varepsilon} + [B_0]_{\gamma}^T [\bar{\bar{E}}_{\gamma 0}] [B_0]_{\gamma} \right) r dr dz \quad (75)$$

$$[k_m] = \pi \iint \left([B_m]_{\varepsilon}^T [E_{\varepsilon}] [B_m]_{\varepsilon} + [B_m]_{\gamma}^T [E_{\gamma}] [B_m]_{\gamma} \right) r dr dz \quad \text{for } m>0 \quad (76)$$

The stiffness matrix of a quadrilateral ring element is to be numerically integrated by Gauss quadrature rule which is most suitable for FEM applications since such rules use a minimal number of points to achieve a desired level of accuracy. Denote by ξ_k and η_l the Gauss points abscissae whereas w_k and w_l denote the corresponding integration weights, with indices k and l running from 1 to number of gauss points used. If both the bending (ε) and shear terms (γ) in the stiffness matrix are integrated using p Gauss points then it is called full integration (FI). In the element formulation, a constant shear locking for 4 node ring element and a linear shear locking for 9 node ring element is used to solve shear locking problem in some particular problems such as thin circular plates. In other words, selectively reduced integration (SRI) technique in which the bending terms are integrated using (p) -point Gauss quadrature rule and the shear terms are integrated using $(p-1)$ -point Gauss quadrature rule is used in such problems. The stiffness matrices are calculated from the following expressions for selectively reduced integration technique used in the thesis:

$$[\bar{k}_0] = 2\pi \left(\begin{array}{l} \sum_{k=1}^p \sum_{l=1}^p w_k w_l [B_0]_{\varepsilon}^T (\xi_k, \eta_l) [\bar{E}_{\varepsilon 0}] [B_0]_{\varepsilon} (\xi_k, \eta_l) r(\xi_k, \eta_l) J(\xi_k, \eta_l) \\ + \sum_{k=1}^{p-1} \sum_{l=1}^{p-1} w_k w_l [B_0]_{\gamma}^T (\xi_k, \eta_l) [\bar{E}_{\gamma 0}] [B_0]_{\gamma} (\xi_k, \eta_l) r(\xi_k, \eta_l) J(\xi_k, \eta_l) \end{array} \right) \quad (77)$$

$$[\bar{k}_0] = 2\pi \left(\begin{array}{l} \sum_{k=1}^p \sum_{l=1}^p w_k w_l [B_0]_{\varepsilon}^T (\xi_k, \eta_l) [\bar{E}_{\varepsilon 0}] [B_0]_{\varepsilon} (\xi_k, \eta_l) r(\xi_k, \eta_l) J(\xi_k, \eta_l) \\ + \sum_{k=1}^{p-1} \sum_{l=1}^{p-1} w_k w_l [B_0]_{\gamma}^T (\xi_k, \eta_l) [\bar{E}_{\gamma 0}] [B_0]_{\gamma} (\xi_k, \eta_l) r(\xi_k, \eta_l) J(\xi_k, \eta_l) \end{array} \right) \quad (78)$$

for $m > 0$

$$[k_m] = \pi \left(\begin{array}{l} \sum_{k=1}^p \sum_{l=1}^p w_k w_l [B_m]_{\varepsilon}^T (\xi_k, \eta_l) [E_{\varepsilon}] [B_m]_{\varepsilon} (\xi_k, \eta_l) r(\xi_k, \eta_l) J(\xi_k, \eta_l) \\ + \sum_{k=1}^{p-1} \sum_{l=1}^{p-1} w_k w_l [B_m]_{\gamma}^T (\xi_k, \eta_l) [E_{\gamma}] [B_m]_{\gamma} (\xi_k, \eta_l) r(\xi_k, \eta_l) J(\xi_k, \eta_l) \end{array} \right) \quad (79)$$

Here $[B_m]_{\varepsilon}(\xi_k, \eta_l)$ and $[B_m]_{\gamma}(\xi_k, \eta_l)$ mean that these matrices are evaluated at Gauss points; likewise for $r(\xi_k, \eta_l)$, the radius of the Gauss point and $J(\xi_k, \eta_l)$, the Jacobian determinant that maps the area element in global coordinates (r, z) to area in the natural coordinates (ξ, η) as discussed previously. In general a unidimensional Gauss rule with p points integrates exactly polynomials of order up to $2p-1$. Therefore, $p=2$ points in each direction for quadratic integrand of 4 node ring element and $p=3$ points in each direction for fourth order integrand of 9 node ring element are used in numerical integrations.

1.13. Element Mass Matrix

A mass matrix is a discrete representation of a continuous distribution of mass. A consistent element mass matrix is to be determined in the finite element formulation. It is termed “consistent” because shape functions used are the same functions used to generate the element stiffness matrix in Eq. 64 (Cook, 1989). The consistent mass matrix of an element is calculated from the derivation of the kinetic energy. For an axisymmetric solid element the kinetic energy can be expressed as:

$$T = \frac{1}{2} \int \rho \{\dot{u}\}^T \{\dot{u}\} dV \quad (80)$$

where ρ is the mass density of the element and $\{\dot{u}\}$ is the velocity vector at a point in the element (Karadeniz, 2009). The velocity vector at a point for the Fourier term m can be expressed using Eq. 40 as:

$$\{\dot{u}\} = \sum_{m=0}^{\infty} \left(\left[\overline{g_{\theta m}} \right]_u [N] \left\{ \overline{\dot{d}}_m \right\} + \left[\overline{\overline{g_{\theta m}}} \right]_u [N] \left\{ \overline{\overline{\dot{d}}}_m \right\} \right) \quad (81)$$

Then the kinetic energy becomes for single and double barred terms and for m^{th} harmonic as stated by:

$$\overline{T}_m = \frac{1}{2} \int \rho \left\{ \overline{\dot{d}}_m \right\}^T [N]^T \left(\left[\overline{g_{\theta m}} \right]_u^T \left[\overline{g_{\theta m}} \right]_u \right) [N] \left\{ \overline{\dot{d}}_m \right\} dV = \frac{1}{2} \left\{ \overline{\dot{d}}_m \right\}^T \left[\overline{m}_m \right] \left\{ \overline{\dot{d}}_m \right\} \quad (82)$$

$$\overline{\overline{T}}_m = \frac{1}{2} \int \rho \left\{ \overline{\overline{\dot{d}}}_m \right\}^T [N]^T \left(\left[\overline{\overline{g_{\theta m}}} \right]_u^T \left[\overline{\overline{g_{\theta m}}} \right]_u \right) [N] \left\{ \overline{\overline{\dot{d}}}_m \right\} dV = \frac{1}{2} \left\{ \overline{\overline{\dot{d}}}_m \right\}^T \left[\overline{\overline{m}}_m \right] \left\{ \overline{\overline{\dot{d}}}_m \right\} \quad (83)$$

From Eqs. 82 and 83 the mass matrices for single and double barred terms of an element for the Fourier term m can be taken out by expressing the infinitesimal volume in cylindrical coordinates as:

$$\left[\overline{m}_m \right] = \iint \rho [N]^T [N] \left(\int_0^{2\pi} \left(\left[\overline{g_{\theta m}} \right]_u^T \left[\overline{g_{\theta m}} \right]_u \right) d\theta \right) r dr dz \quad (84)$$

$$\left[\overline{\overline{m}}_m \right] = \iint \rho [N]^T [N] \left(\int_0^{2\pi} \left(\left[\overline{\overline{g_{\theta m}}} \right]_u^T \left[\overline{\overline{g_{\theta m}}} \right]_u \right) d\theta \right) r dr dz \quad (85)$$

It can be observed that each term in the product $\left[\overline{g_{\theta m}}\right]_u^T \left[\overline{g_{\theta m}}\right]_u$ and $\left[\overline{\overline{g_{\theta m}}}\right]_u^T \left[\overline{\overline{g_{\theta m}}}\right]_u$ will be a function of either $\cos^2 m\theta$ or $\sin^2 m\theta$. Thus, integration with respect to θ can be carried out explicitly using orthogonality property of trigonometric functions. The integration will result in a factor π that multiplies each term for each Fourier series harmonics except for zeroth ($m=0$) harmonic for both single and double barred terms. Therefore, $\left[\overline{m_m}\right] = \left[\overline{\overline{m_m}}\right] = \left[m_m\right]$ is valid for $m>0$. For zeroth harmonic the factor will be 2π for the integration. Thus, for the m th harmonic the mass matrix is obtained as (Bhatti, 2006):

$$\left[\overline{m_0}\right] = 2\pi \iint \rho [N]^T \begin{bmatrix} 1 & 0 & 0 \\ 0 & 0 & 0 \\ 0 & 0 & 1 \end{bmatrix} [N] r dr dz \quad (86)$$

$$\left[\overline{\overline{m_0}}\right] = 2\pi \iint \rho [N]^T \begin{bmatrix} 0 & 0 & 0 \\ 0 & 1 & 0 \\ 0 & 0 & 0 \end{bmatrix} [N] r dr dz \quad (87)$$

$$\left[m_m\right] = \pi \iint \rho [N]^T [N] r dr dz \quad (m>0) \quad (88)$$

Using Gauss quadrature rule to take the integrals above we have the following expressions for the element mass matrices for Fourier harmonics as:

$$\left[\overline{m_0}\right] = 2\pi \sum_{k=1}^p \sum_{l=1}^p w_k w_l \rho N^T(\xi_k, \eta_l) \begin{bmatrix} 1 & 0 & 0 \\ 0 & 0 & 0 \\ 0 & 0 & 1 \end{bmatrix} N(\xi_k, \eta_l) r(\xi_k, \eta_l) J(\xi_k, \eta_l) \quad (89)$$

$$\left[\overline{\overline{m_0}}\right] = 2\pi \sum_{k=1}^p \sum_{l=1}^p w_k w_l \rho N^T(\xi_k, \eta_l) \begin{bmatrix} 0 & 0 & 0 \\ 0 & 1 & 0 \\ 0 & 0 & 0 \end{bmatrix} N(\xi_k, \eta_l) r(\xi_k, \eta_l) J(\xi_k, \eta_l) \quad (90)$$

$$\left[m_m\right] = \pi \sum_{k=1}^p \sum_{l=1}^p w_k w_l \rho N^T(\xi_k, \eta_l) N(\xi_k, \eta_l) r(\xi_k, \eta_l) J(\xi_k, \eta_l) \quad \text{for } (m>0) \quad (91)$$

1.14. Element Nodal Force Vectors

In harmonic finite element analysis of axisymmetric structures under non-axisymmetric loading, the loading must be expressed in the form of Fourier series. Each load component is either symmetric or antisymmetric. The complete solution for the original non-axisymmetric loading is obtained by superimposing a reasonable number of solutions for these symmetric and antisymmetric terms (Bhatti, 2006).

1.14.1. Fourier Series Representation of Loading

If the applied loading is a function of θ , using a Fourier series it can be expressed as:

$$T(\theta) = a_0 + \sum_{m=1}^{\infty} a_m \cos m\theta + \sum_{m=1}^{\infty} b_m \sin m\theta \quad (92)$$

For a given loading, the coefficients a_0, a_m, b_m for $m = 1, 2, \dots$, are obtained as follows:

$$\begin{aligned} a_0 &= \frac{1}{2\pi} \int_{-\pi}^{\pi} T(\theta) d\theta \\ a_m &= \frac{1}{\pi} \int_{-\pi}^{\pi} T(\theta) \cos(m\theta) d\theta \\ b_m &= \frac{1}{\pi} \int_{-\pi}^{\pi} T(\theta) \sin(m\theta) d\theta \end{aligned} \quad (93)$$

The a_0 term represents the usual plane axisymmetric or axi-antisymmetric loading since it is independent of θ . A function $f(\theta)$ is called symmetric if $f(\theta) = f(-\theta)$. It is called asymmetric or antisymmetric if $f(\theta) = -f(-\theta)$. For applied loads in the r and z directions, the cosine terms represent symmetric loads with respect to the horizontal axis ($\theta=0$) and the sine terms represent antisymmetric load (Bhatti, 2006). This can be seen from Fig. 6 which shows the symmetric and antisymmetric load components in an axisymmetric body and Fig. 7 shows the plots of constant and the first two cosine and sine terms.

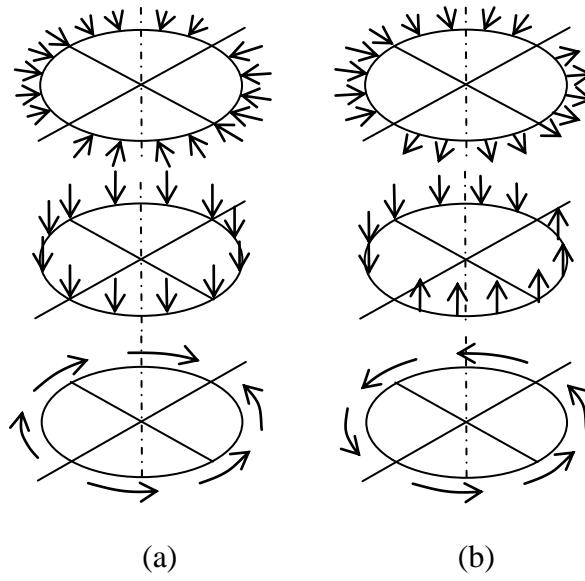


Figure 6. Load components in an axisymmetric body:
 (a) symmetric (b) antisymmetric

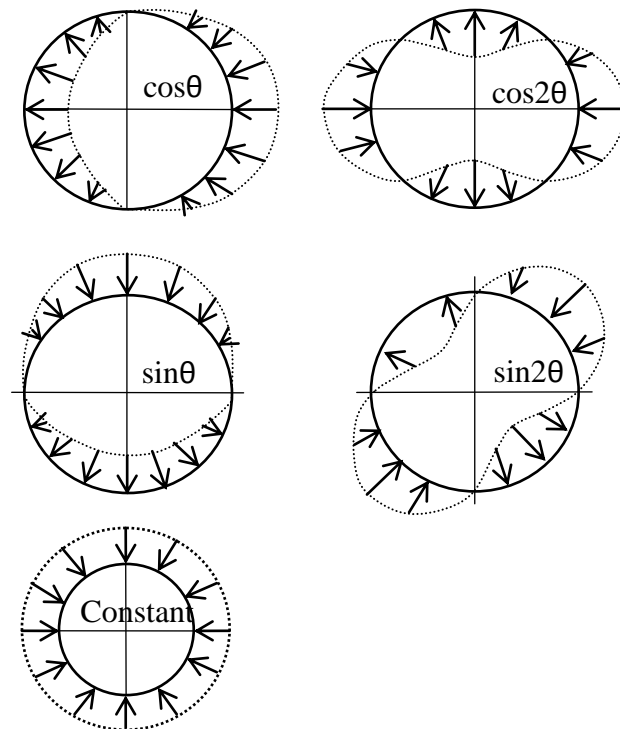


Figure 7. Plots of constant and the first two cosine and sine terms

1.14.2. Consistent Body Force Vector

Body forces (also called volume forces) arise frequently in analysis of structures of revolution. The most important loads of this type are:

1. Gravity (own weight).
2. Centrifugal forces in rotating structures.
3. Thermal, shrinkage and pre-stress effects.

The consistent body force is calculated from the derivation of the external work done by body load. For an axisymmetric solid element the external work done by body force is expressed as (Karadeniz, 2009)

$$W_b = \int \{u_b\}^T \{q_b\} dV = \sum_{m=0}^{\infty} \left(\{\bar{d}_{bm}\} \{\bar{f}_{bm}\} + \{\bar{\bar{d}}_{bm}\} \{\bar{\bar{f}}_{bm}\} \right) \quad (94)$$

where $\{\bar{f}_{bm}\}$ and $\{\bar{\bar{f}}_{bm}\}$ are the consistent body force vectors for the Fourier term m of symmetric and antisymmetric terms.

$$\{u_b\} = \sum_{m=0}^{\infty} \left(\left[\overline{g_{\theta m}} \right]_u [N] \{\bar{d}_{bm}\} + \left[\overline{\bar{g}_{\theta m}} \right]_u [N] \{\bar{\bar{d}}_{bm}\} \right) \quad (95)$$

$$\{q_b\} = \sum_{m=0}^{\infty} \left(\left[\overline{g_{\theta m}} \right]_u \{\bar{q}_{bm}\} + \left[\overline{\bar{g}_{\theta m}} \right]_u \{\bar{\bar{q}}_{bm}\} \right) \quad (96)$$

where $\{\bar{q}_{bm}\}$ and $\{\bar{\bar{q}}_{bm}\}$ are the body load amplitude vectors for the Fourier term m of symmetric and antisymmetric loadings respectively.

$$\{\bar{q}_{bm}\} = \begin{Bmatrix} \bar{q}_{brm} \\ \bar{q}_{b\theta m} \\ \bar{q}_{bzm} \end{Bmatrix} \quad \text{and} \quad \{\bar{\bar{q}}_{bm}\} = \begin{Bmatrix} \bar{\bar{q}}_{brm} \\ \bar{\bar{q}}_{b\theta m} \\ \bar{\bar{q}}_{bzm} \end{Bmatrix} \quad (97)$$

Then having used Eqs. 95 and 96 in Eq. 94 the consistent force vectors for the Fourier term m due to body load can be expressed as:

$$\{\bar{f}_{bm}\} = \int [N]^T \left(\left[\overline{g_{\theta m}} \right]_u^T \left[\overline{g_{\theta m}} \right]_u \right) \{\bar{q}_{bm}\} dV \quad (98)$$

$$\{\bar{f}_{bm}\} = \int [N]^T \left(\left[\overline{\overline{g_{\theta m}}} \right]_u^T \left[\overline{\overline{g_{\theta m}}} \right]_u \right) \{\bar{q}_{bm}\} dV \quad (99)$$

Expressing Eqs. 98 and 99 in terms of cylindrical coordinates and taking integral with respect to the circumferential direction θ produces the following expressions:

$$\{\bar{f}_{b0}\} = 2\pi \int [N]^T \begin{bmatrix} 1 & 0 & 0 \\ 0 & 0 & 0 \\ 0 & 0 & 1 \end{bmatrix} \{\bar{q}_{bm}\} r dr dz \quad (m=0) \quad (100)$$

$$\{\bar{f}_{b0}\} = 2\pi \int [N]^T \begin{bmatrix} 0 & 0 & 0 \\ 0 & 1 & 0 \\ 0 & 0 & 0 \end{bmatrix} \{\bar{q}_{bm}\} r dr dz \quad (m=0) \quad (101)$$

$$\{\bar{f}_{bm}\} = \pi \int [N]^T \{\bar{q}_{bm}\} r dr dz \quad \text{and} \quad \{\bar{f}_{bm}\} = \pi \int [N]^T \{\bar{q}_{bm}\} r dr dz \quad \text{for } (m>0) \quad (102)$$

where $[N]$ is defined in Eq. 42. Using p-point two dimensional Gauss quadrature rule to take the integrals above we have the following expressions for the consistent body force vector for Fourier harmonics as:

$$\{\bar{f}_{b0}\} = 2\pi \sum_{k=1}^p \sum_{l=1}^p w_k w_l N^T(\xi_k, \eta_l) \begin{bmatrix} 1 & 0 & 0 \\ 0 & 0 & 0 \\ 0 & 0 & 1 \end{bmatrix} \{\bar{q}_{b0}\} r(\xi_k, \eta_l) J(\xi_k, \eta_l) \quad \text{for } m=0 \quad (103)$$

$$\{\bar{f}_{b0}\} = 2\pi \sum_{k=1}^p \sum_{l=1}^p w_k w_l N^T(\xi_k, \eta_l) \begin{bmatrix} 0 & 0 & 0 \\ 0 & 1 & 0 \\ 0 & 0 & 0 \end{bmatrix} \{\bar{q}_{b0}\} r(\xi_k, \eta_l) J(\xi_k, \eta_l)$$

$$\begin{aligned} \{\bar{f}_{bm}\} &= \pi \sum_{k=1}^p \sum_{l=1}^p w_k w_l [N]^T (\xi_k, \eta_l) \{\bar{q}_{bm}\} r(\xi_k, \eta_l) J(\xi_k, \eta_l) \\ \{\bar{f}_{bm}\} &= \pi \sum_{k=1}^p \sum_{l=1}^p w_k w_l [N]^T (\xi_k, \eta_l) \{\bar{q}_{bm}\} r(\xi_k, \eta_l) J(\xi_k, \eta_l) \end{aligned} \quad \text{for } m>0 \quad (104)$$

1.14.3. Consistent Surface Force Vector

The consistent surface force vector is calculated from the derivation of the external work done by surface load. For an axisymmetric solid element the external work done by surface force is expressed as (Karadeniz, 2009)

$$W_s = \int \{u_s\}^T \{q_s\} dS = \sum_{m=0}^{\infty} \left(\{\bar{d}_{sm}\} \{\bar{f}_{sm}\} + \{\bar{d}_{sm}\} \{\bar{f}_{sm}\} \right) \quad (105)$$

where $\{u_s\}$ is the displacement vector at a point on the surface of loads, $\{q_s\}$ is the applied surface load vector and dS denotes an infinitesimal surface on which surface loads apply.

$$\{u_s\} = \sum_{m=0}^{\infty} \left(\left[\overline{g_{\theta m}} \right]_u [N] \{\bar{d}_{sm}\} + \left[\overline{g_{\theta m}} \right]_u [N] \{\bar{d}_{sm}\} \right) \quad (106)$$

$$\{q_s\} = \sum_{m=0}^{\infty} \left(\left[\overline{g_{\theta m}} \right]_u \{\bar{q}_{sm}\} + \left[\overline{g_{\theta m}} \right]_u \{\bar{q}_{sm}\} \right) \quad (107)$$

where $\{\bar{q}_{sm}\}$ and $\{\bar{q}_{sm}\}$ are the surface load amplitude vectors for the Fourier term m .

$$\{\bar{q}_{sm}\} = \begin{Bmatrix} \bar{q}_{srm} \\ \bar{q}_{s\theta m} \\ \bar{q}_{szm} \end{Bmatrix} \quad \text{and} \quad \{\bar{q}_{sm}\} = \begin{Bmatrix} \bar{q}_{srm} \\ \bar{q}_{s\theta m} \\ \bar{q}_{szm} \end{Bmatrix} \quad (108)$$

Then the consistent force vector for the Fourier term m due to surface force can be expressed as:

$$\begin{aligned}
\{\bar{f}_{sm}\} &= \int [N]_s^T \left(\begin{bmatrix} \overline{g_{\theta m}} \\ \overline{g_{\theta m}} \end{bmatrix}_u^T \right) \{\bar{q}_{sm}\} dS \\
\{\bar{\bar{f}}_{sm}\} &= \int [N]_s^T \left(\begin{bmatrix} \overline{\overline{g_{\theta m}}} \\ \overline{\overline{g_{\theta m}}} \end{bmatrix}_u^T \right) \{\bar{\bar{q}}_{sm}\} dS
\end{aligned} \tag{109}$$

where $[N]_s$ is the values of $[N]$ at locations of surface load vectors. Expressing Eq. 106 in terms of cylindrical coordinates and taking integral with respect to the circumferential direction θ produces the following expressions:

$$\begin{aligned}
\{\bar{f}_{s0}\} &= 2\pi \int [N]_s^T \begin{bmatrix} 1 & 0 & 0 \\ 0 & 0 & 0 \\ 0 & 0 & 1 \end{bmatrix} \{\bar{q}_{s0}\} r ds \\
\{\bar{\bar{f}}_{s0}\} &= 2\pi \int [N]_s^T \begin{bmatrix} 0 & 0 & 0 \\ 0 & 1 & 0 \\ 0 & 0 & 0 \end{bmatrix} \{\bar{\bar{q}}_{s0}\} r ds
\end{aligned} \quad (m=0) \tag{110}$$

$$\begin{aligned}
\{\bar{f}_{sm}\} &= \pi \int [N]_s^T \{\bar{q}_{sm}\} r ds \\
\{\bar{\bar{f}}_{sm}\} &= \pi \int [N]_s^T \{\bar{\bar{q}}_{sm}\} r ds
\end{aligned} \quad (m>0) \tag{111}$$

where, $ds = \sqrt{dr^2 + dz^2}$. Unidimensional numerical integration can be applied for the consistent force vector associated with surface traction. Then we have the following expressions in which J_Γ is the associated arc length Jacobian.

$$\begin{aligned}
\{\bar{f}_{s0}\} &= 2\pi \sum_{k=1}^p w_k [N]_s^T(\xi_k) \begin{bmatrix} 1 & 0 & 0 \\ 0 & 0 & 0 \\ 0 & 0 & 1 \end{bmatrix} \{q_{b0}\} r(\xi_k) J_\Gamma(\xi_k) \\
\{\bar{\bar{f}}_{s0}\} &= 2\pi \sum_{k=1}^p w_k [N]_s^T(\xi_k) \begin{bmatrix} 0 & 0 & 0 \\ 0 & 1 & 0 \\ 0 & 0 & 0 \end{bmatrix} \{q_{b0}\} r(\xi_k) J_\Gamma(\xi_k)
\end{aligned} \quad \text{for } m=0 \tag{112}$$

$$\begin{aligned}
\{\bar{f}_{sm}\} &= \pi \sum_{k=1}^1 w_k [N]_s^T (\xi_k) \{\bar{q}_{bm}\} r(\xi_k) J_\Gamma(\xi_k) \\
\{\bar{f}_{sm}\} &= \pi \sum_{k=1}^1 w_k [N]_s^T (\xi_k) \{\bar{q}_{bm}\} r(\xi_k) J_\Gamma(\xi_k)
\end{aligned}
\quad \text{for } m > 0 \quad (113)$$

1.14.4. Consistent Line and Concentrated Load Vectors

The consistent line force vector is calculated from the derivation of the external work done by line load. For an axisymmetric solid element the external work done by line load is expressed as (Karadeniz, 2009)

$$W_l = \int \{u_l\}^T \{q_l\} dl = \sum_{m=0}^{\infty} \left(\{\bar{d}_{lm}\}^T \{\bar{f}_{lm}\} + \{\bar{d}_{lm}\}^T \{\bar{f}_{lm}\} \right) \quad (114)$$

$$\{u_l\} = \sum_{m=0}^{\infty} \left(\left[\overline{g_{\theta m}} \right]_u [N] \{\bar{d}_{lm}\} + \left[\overline{g_{\theta m}} \right]_u [N] \{\bar{d}_{lm}\} \right) \quad (115)$$

$$\{q_l\} = \sum_{m=0}^{\infty} \left(\left[\overline{g_{\theta m}} \right]_u \{\bar{q}_{lm}\} + \left[\overline{g_{\theta m}} \right]_u \{\bar{q}_{lm}\} \right) \quad (116)$$

where $\{u_l\}$ is the displacement vector at a point on the line of loads and $\{q_l\}$ is the applied line load vector and dl denotes an infinitesimal line in the element on which line loads apply. Substituting Eqs. 115 and 116 into Eq. 114 gives the following expressions of the consistent line force vectors for the Fourier term m of symmetric and antisymmetric series expansions:

$$\begin{aligned}
\{\bar{f}_{lm}\} &= \int [N]_l^T \left(\left[\overline{g_{\theta m}} \right]_u^T \left[\overline{g_{\theta m}} \right]_u \right) \{\bar{q}_{lm}\} dl \\
\{\bar{f}_{lm}\} &= \int [N]_l^T \left(\left[\overline{g_{\theta m}} \right]_u^T \left[\overline{g_{\theta m}} \right]_u \right) \{\bar{q}_{lm}\} dl
\end{aligned}
\quad (117)$$

where $[N]_l$ is the shape function matrix defined at locations of line load vectors and $\{\bar{q}_{lm}\}$ and $\{\bar{\bar{q}}_{lm}\}$ are the line load amplitude vectors for symmetric and antisymmetric loading respectively. Expressing Eq. 117 in terms of cylindrical coordinates and taking integral with respect to the circumferential direction θ produces the following expressions:

$$\{\bar{f}_{l0}\} = 2\pi r_l [N]_l^T \begin{bmatrix} 1 & 0 & 0 \\ 0 & 0 & 0 \\ 0 & 0 & 1 \end{bmatrix} \{\bar{q}_{l0}\} \quad \text{for } (m=0) \quad (118)$$

$$\{\bar{\bar{f}}_{l0}\} = 2\pi r_l [N]_l^T \begin{bmatrix} 0 & 0 & 0 \\ 0 & 1 & 0 \\ 0 & 0 & 0 \end{bmatrix} \{\bar{\bar{q}}_{l0}\}$$

$$\{\bar{f}_{lm}\} = \pi r_l [N]_l^T \{\bar{q}_{lm}\} \quad \text{and} \quad \{\bar{\bar{f}}_{lm}\} = \pi r_l [N]_l^T \{\bar{\bar{q}}_{lm}\} \quad \text{for } (m>0) \quad (119)$$

where r_l is the radial distance at which line load is applied. With the same manner, consistent force vectors due to concentrated joint forces can be expressed as follows:

$$\{\bar{f}_{j0}\} = 2\pi r_{jp} \begin{bmatrix} 1 & 0 & 0 \\ 0 & 0 & 0 \\ 0 & 0 & 1 \end{bmatrix} \{\bar{P}_{j0}\} \quad \text{for } (m=0) \quad (120)$$

$$\{\bar{\bar{f}}_{j0}\} = 2\pi r_{jp} \begin{bmatrix} 0 & 0 & 0 \\ 0 & 1 & 0 \\ 0 & 0 & 0 \end{bmatrix} \{\bar{\bar{P}}_{j0}\}$$

$$\{\bar{f}_{jm}\} = \pi r_{jp} \{\bar{P}_{jm}\} \quad \text{for } (m>0) \quad (121)$$

$$\{\bar{\bar{f}}_{jm}\} = \pi r_{jp} \{\bar{\bar{P}}_{jm}\}$$

where r_{jp} is the radial distance of the joint j at which the concentrated force vector $\{P_{jm}\}$ for the Fourier term m , is applied.

1.15. Modal Analysis

The goal of modal analysis in structural mechanics is to determine the natural mode shapes and frequencies of a structure during free vibration using structure's overall mass and stiffness. In other words, modal analysis investigates how a structure vibrates. To start with the equation of motion for free and undamped vibrations is of the form

$$[M]\{\ddot{u}\}+[K]\{u\}=0 \quad (122)$$

where $\{u\}$ is the global degree of freedom vector and $[M]$ and $[K]$ are, respectively, the system mass and stiffness matrices. When vibrating in one of the mode shapes all the points in the system undergo simple harmonic motion with the corresponding natural frequency ω_i , which can be stated as (Weaver and Johnston, 1984)

$$u = \phi_i \sin(\omega_i t) \quad (123)$$

in which ϕ_i is the nodal amplitude vector (or mode shape) with each component corresponding to the specific degree of freedom. By differentiating Eq. 123 twice with respect to the time t , we also find

$$\{\ddot{u}\} = -\omega_i^2 \phi_i \sin(\omega_i t) \quad (124)$$

Substitution of Eqs. 123 and 124 into Eq. 122 allows cancellation of the term $\sin(\omega_i t)$, which leaves:

$$(K - \omega_i^2 M)\phi_i = 0 \quad (125)$$

This is the basic statement of the free vibration problem. Eq. 125 is called a generalized eigenvalue problem (Cook, 1989). To avoid a nontrivial solution for the Eq. 125, it follows that the determinant of the coefficient matrix $(K - \omega_i^2 M)$ should vanish:

$$\det([K] - \lambda_i[M]) = 0 \quad (126)$$

where $\lambda_i = \omega_i^2$ and the lowest nonzero ω_i is called as the fundamental vibration frequency. Solving Eq. 126 actually leads the eigenvalues, λ_i , $i=1, \dots, s$, where s is the size of the mass or stiffness matrices which equals the number of degrees of freedom (dof) of the entire system. In fact the eigenvalue problem in Eq. 125 leads the square of natural frequencies (Ahmed and Bonakdar, 2008). The Eq. 125 is satisfied by eigenvalues, ω_i^2 , and corresponding eigenvectors ϕ_i . The physical interpretation of the eigenvalues and eigenvectors which come from solving the system are that they represent the frequencies and corresponding mode shapes. The solution of Eq. 125 is obtained using QR inverse iteration method as explained in the reference (Bathe, 1996).

1.16. Static Analysis

In this section we are concerned with the solution of the simultaneous equations that arise in the static analysis of axisymmetric structures using finite element method. The matrix equation for static problems is given by

$$Ku = P \quad (127)$$

where K is the stiffness matrix, u is the displacement vector, and P is the load vector of the finite element system. Since P and u may be functions of time t , we may also consider the equation above as the dynamic equilibrium equations of a finite element system in which inertia and velocity dependent damping forces have been neglected (Bathe, 1996).

Solution of the equations by direct inversion of the stiffness matrix is inefficient and generally impractical for large problems. The most efficient static solution routines are based on the Gauss elimination procedure (Smith, 1988).

1.17. Linear Dynamic Analysis

A structural dynamic problem differs from its static loading counterpart in various important respects. The main difference to be noted, by definition, is the time varying nature of the dynamic problem. Because the load and the response vary with time, it is evident that a dynamic problem does not have a single solution, as a static problem does; instead the analyst must establish a succession of solutions corresponding to all times of interest in the response history. Thus a dynamic analysis is clearly more complex and time consuming than a static analysis (Clough and Penzien, 1975).

The equations of equilibrium governing the linear dynamic response of a system of finite elements can be expressed as:

$$M\ddot{u} + C\dot{u} + Ku = P \quad (128)$$

where M , C , and K are the mass, damping, and stiffness matrices; P is the vector of externally applied loads; and u , \dot{u} , and \ddot{u} are the displacement, velocity, and acceleration vectors of the finite element assemblage. In dynamic analysis, in principle, static equilibrium at time t , which includes the effect of acceleration-dependent inertia forces and velocity-dependent damping forces, is considered.

Mathematically, Eq. 128 represents a system of linear differential equations of second order and, in principle; the solution to the equations can be obtained by standard procedures for the solution of differential equations with constant coefficients. However, the procedures proposed can become very expensive if the order of the matrices is large. In practical finite element analysis, we are therefore mainly interested in a few effective numerical methods (Bathe, 1996). Newmark direct integration method is used in this study for dynamic solution of the equations. In direct integration the differential equations represented by Eq. 128 are integrated using a numerical step-by-step procedure as explained in the following section.

1.17.1. The Newmark Method

Newmark has expressed the velocities and displacements at the end of a time increment in terms of the known parameters at the beginning and the unknown acceleration at the end of the time step as (Smith, 1988):

$$\dot{u}_{t+\Delta t} = \dot{u}_t + [(1-\delta)\ddot{u}_t + \delta\ddot{u}_{t+\Delta t}]\Delta t \quad (129)$$

$$u_{t+\Delta t} = u_t + \dot{u}_t\Delta t + \left[\left(\frac{1}{2} - \beta\right)\ddot{u}_t + \beta\ddot{u}_{t+\Delta t}\right]\Delta t^2 \quad (130)$$

where δ and β are weighting factors. Careful study of these equations will reveal that the standard rules of kinematics are being used to predict the velocity and displacement at the end of an interval given the conditions at the start of the interval. The difference is that the acceleration is not constant and therefore weighting factors are used to obtain an average acceleration over the interval. Using Eq. 130 the acceleration at the end of the interval is

$$\ddot{u}_{t+\Delta t} = (1/\beta\Delta t^2)[u_{t+\Delta t} - u_t - \dot{u}_t\Delta t - \left(\frac{1}{2} - \beta\right)\ddot{u}_t\Delta t^2] \quad (131)$$

Substituting in Eq. 129, we obtain the velocity

$$\dot{u}_{t+\Delta t} = (\delta/\beta\Delta t)(u_{t+\Delta t} - u_t) + (1-\delta/\beta)\dot{u}_t + (1-\delta/2\beta)\Delta t\ddot{u}_t \quad (132)$$

The equation of motion at the end of the interval is given by

$$M\ddot{u}_{t+\Delta t} + C\dot{u}_{t+\Delta t} + Ku_{t+\Delta t} = P_{t+\Delta t} \quad (133)$$

Therefore, by substituting Eqs. 131 and 132 into Eq. 133 the following equation is obtained and used for forward integration of the displacements from time t to $t + \Delta t$. Then Eqs. 131 and 132 are used to obtain the velocities and accelerations.

$$\begin{aligned}
& \left[K + \frac{1}{\beta \Delta t^2} M + \frac{\delta}{\beta \Delta t} C \right] u_{t+\Delta t} \\
& = P_{t+\Delta t} + \left(\frac{1}{\beta \Delta t^2} M + \frac{\delta}{\beta \Delta t} C \right) u_t \\
& \quad + \left[\frac{1}{\beta \Delta t} M - \left(1 - \frac{\delta}{\beta} \right) C \right] \dot{u}_t \\
& \quad + \left[\left(\frac{1}{2\beta} - 1 \right) M - \left(1 - \frac{\delta}{2\beta} \right) \Delta t C \right] \ddot{u}_t
\end{aligned} \tag{134}$$

It should be apparent that Eq. 134 takes the form of an equilibrium equation, $Ku = P$, with the structural motion at time t modifying the load on the right-hand side. On the left-hand side the stiffness matrix is modified correspondingly. No special starting procedure is required. In the case of dynamic response of a linear system the modified stiffness need only be determined and factorized at the start of the solution. Then the right-hand side, which will vary with time, can be treated as a new load vector at each time step. Rapid evaluation of the full response history is therefore possible (Smith, 1988).

1.18. Model Reduction for Linear Systems

Model reduction is a computational cost saving tool that enables an analyst to extract dynamic quantities of interest from a reduced dynamic model. The reduction consists of condensing out some degree of freedoms called as slave from the full size finite element model and remaining ones are called as master degrees of freedom. In model reduction for linear systems, the reduced system matrices are obtained using a linear coordinate reduction matrix, $[R]$, developed by Guyan from the full model stiffness matrix as explained in (Rhee, 2000). Using the reduction matrix the desired reduced model matrices are defined by (Cook, 1989)

$$[K_r] = [R]^T [K] [R] \tag{135}$$

$$[M_r] = [R]^T [M] [R] \tag{136}$$

If damping matrix $[C]$ and external loads $\{P\}$ appear in the equation of motion, then condensed damping matrix $[C_r]=[R]^T[C][R]$ and condensed external loads $\{P_r\}=[R]^T\{P\}$ appear in the reduced equation of motion as below:

$$[M_r]\{\ddot{u}_m\}+[C_r]\{\dot{u}_m\}+[K_r]\{u_m\}=\{P_r\} \quad (137)$$

where $\{u_m\}$ represents the displacements of master degrees of freedom.

2. NUMERICAL EXAMPLES AND RESULTS

2.1. Accuracy Verification of the Program

The program coded in this study for the static, dynamic and free vibration analysis of axisymmetric structures is checked for different loadings. The static deformation results of a hollow cylinder under various loadings, an internally pressurized thick cylinder, and a rotating thin disc are compared with the analytical solutions. Additionally, the modal results of a hollow cylinder are compared with the results obtained using hexagonal elements in SAP2000 commercial computer program.

2.1.1. Hollow Cylinder Under Various Loadings

Consider a hollow cylinder with length $L=0.6\text{m}$, inner radius $a=0.05\text{m}$ and outer radius $b=0.06\text{m}$ with modulus of elasticity $E=2\times 10^{11}\text{Pa}$ and Poisson's ratio $\nu=0.3$, that is subjected to three separate loading conditions which are axial normal load, axial torque and lateral point load. In the cases of axial load, axial torque and lateral load forces of magnitude $F_z=8\times 10^3\text{N}$, $T_z=4.4\times 10^3\text{N}$ and $P=1\times 10^3\text{N}$ are applied, respectively. The boundary condition of the cylinder is completely fixed at one end and free at the other end.

When the cylinder of length, L , and cross-sectional area, A , is subjected to axial load of magnitude, F_z , the exact solution for cylinder elongation, δ , is obtained from Eq.138

$$\delta = \frac{F_z L}{EA} \quad (138)$$

In the case of torsion one end of the cylinder is completely fixed and the other end is free with the external torque applied at the free end. The exact solution for the rotation of free end is obtained from Eq. 138.

$$\theta = \frac{T_z L}{JG} \quad (139)$$

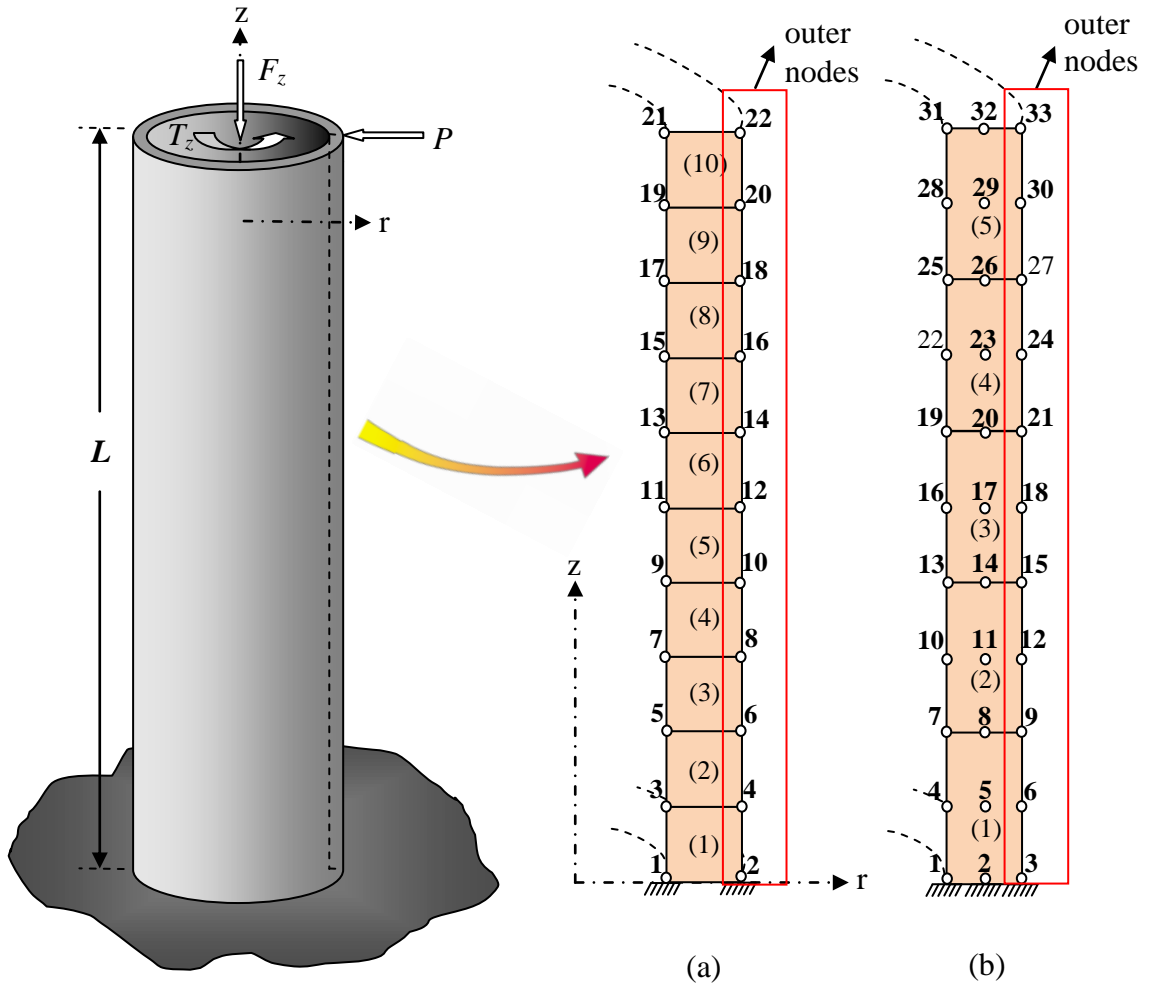


Figure 8. FEM discretization for the hollow cylinder under various loadings (a) 10-element Ring4 discretization (b) 5-element Ring9 discretization

in which T_z is the axial torque, J is polar moment of inertia and G is the shear modulus. The rotation is obtained using the following equation in coded program

$$\theta = \frac{u_\theta|_a}{a} = \frac{u_\theta|_b}{b} \quad (140)$$

where $u_\theta|_a$ and $u_\theta|_b$ are the circumferential displacements and r_1 and r_2 are the radius of an inner and outer node, respectively. The exact solution for the free end deflection, δ , using the Euler beam theory is obtained from Eq. 141.

$$\delta = \frac{PL^3}{3EI} \quad (141)$$

where P is the lateral point load and I is the area moment of inertia of the cylinder section.

Finite element discretizations of the cylinder are shown in Fig.8. 10 Ring4 and 5 Ring9 elements are used in the static deformation analysis under various loadings. The analytical results are compared with the ones obtained from Ring4 and Ring9 elements and given in Table 2. All relative errors are measured with respect to the analytical method. The bracketed number indicates the number of elements used in each method.

Table 2. Cylinder deformations under various loadings

	Method			Relative error	
	Ring4 (10)	Ring9 (5)	Analytical	Ring4	Ring9
Axial elongation(m)	6.870×10^{-6}	6.882×10^{-6}	6.945×10^{-6}	1.1%	0.8%
Rotation (rad)	3.255×10^{-3}	3.255×10^{-3}	3.256×10^{-3}	0.03%	0.03%
Tip deflection(m)	6.597×10^{-5}	6.835×10^{-5}	6.831×10^{-5}	3.4%	0.06%

When the relative errors are considered it can be concluded that both the ring elements produces close results compare with the analytical solutions. However, in the case of bending in which the lateral deflection is a cubic function of the longitudinal or axial coordinate, more elements are required to produce an accurate result which is attributed to the first order shape functions used in the axial direction of the Ring4. It seems from Table 2 that Ring9 gives better results when relative errors are considered. Also, it should be noted that mesh refinement can decrease the relative errors.

2.1.2. Modal Analysis of a Hollow Cylinder

In this section modal analysis is carried out for the single layer hollow cylinder used in the previous section and natural frequencies for basic mode shapes are compared with the results obtained in SAP2000. Finite element models with and without model reduction (MR) are used in the modal analysis of the cylinder. The aim of using model reduction is to save time in modal analysis using QR inverse iteration technique. Using model reduction in QR inverse iteration technique all nodes but the outer ones as shown in Fig.8 are

condensed out from the full finite element model to check whether the model reduction procedure yields inaccurate eigenvalue solutions. The natural frequencies using Ring4 without model reduction (R4), Ring9 without model reduction (R9), Ring4 with model reduction (R4 (MR)), Ring9 with model reduction (R9 (MR)) and brick elements and their relative errors are listed in Table 3 for basic mode shapes. Relative errors are measured with respect to results obtained using brick elements in SAP2000. Sufficiently large numbers of elements (1350 brick elements) are used to assure precise frequency results while the model is meshed using 30 Ring4 (R4) and 15 Ring9 (R9) elements in the axial direction and 1 Ring4 and 1 Ring9 element in radial direction. As it is seen from Table 3 results obtained using ring elements with and without model reduction in coded program and brick elements in SAP2000 are in good agreement, which verifies that the solid ring elements with model reduction can be used successfully for the modal analysis of axisymmetric structures.

Table 3. Comparison of natural frequencies obtained from R4, R9 and brick elements for different modes (MR: model reduction)

Mode shape	Natural frequency (Hz)					Relative error			
	R4(MR) (30)	R9(MR) (15)	R4 (30)	R9 (15)	Brick (1350)	R4(MR) (%)	R9(MR) (%)	R4 (%)	R9 (%)
Bending	295	293	294	293	292	1.02	0.34	0.68	0.34
Torsional	1308	1308	1308	1308	1302	0.46	0.46	0.46	0.46
Bending	1459	1453	1459	1447	1443	1.10	0.69	1.10	0.27
Axial	2119	2115	2119	2117	2118	0.04	0.14	0.04	0.04
Bending	3331	3269	3307	3267	3250	2.5	0.58	1.75	0.52
Torsional	3931	3929	3929	3925	3900	0.8	0.74	0.74	0.64

2.1.3. Internally Pressurized Thick Cylinder

The problem in this part is the analysis of a cylindrical hollow tube of inner radius $a=160mm$ and outer radius $b=320mm$ subjected to internal pressure $P=150 MPa$. The tube is as shown in Fig. 9. The tube extends indefinitely along the z axis and is in a plane strain state along that direction. The material is isotropic with elastic modulus $E=2 \times 10^5 MPa$ and

Poisson's ratio $\nu=0.2$. A slice of thickness d is extracted and discretized as shown in Fig. 9 using N_{er} Ring4 and Ring9 elements along the radial direction r and one along the axial direction z (In that figure, N_{er} are 4 and 2 for Ring4 and Ring9, respectively). Nodes move in radial direction only, which results in the support conditions as drawn in Fig.9(a, b).

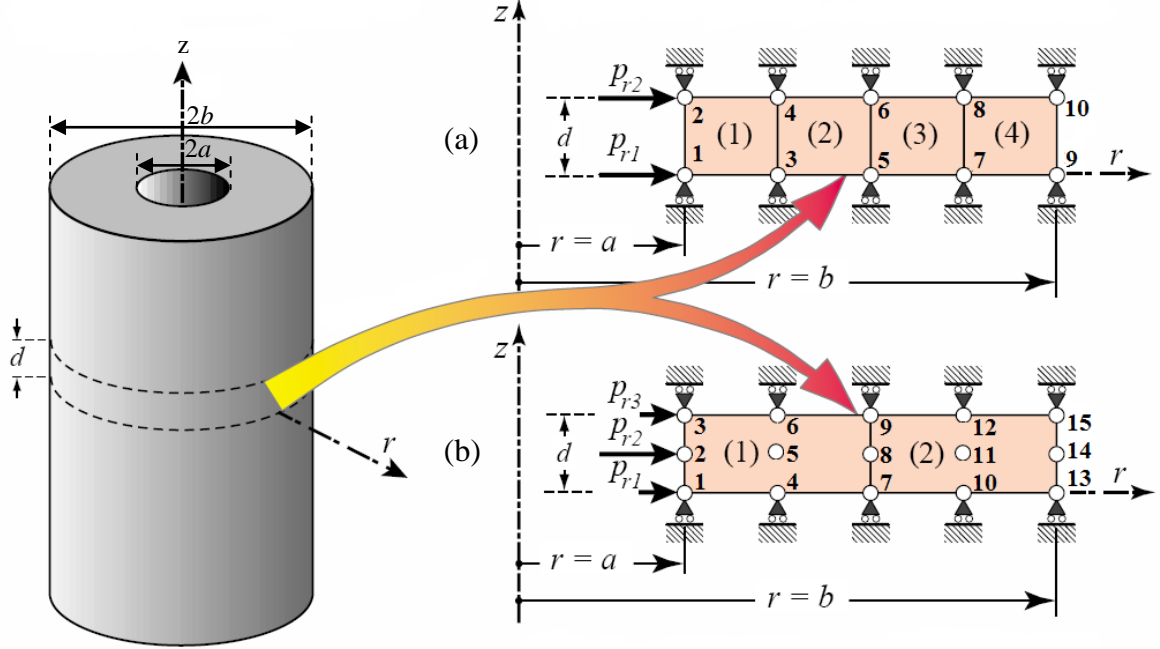
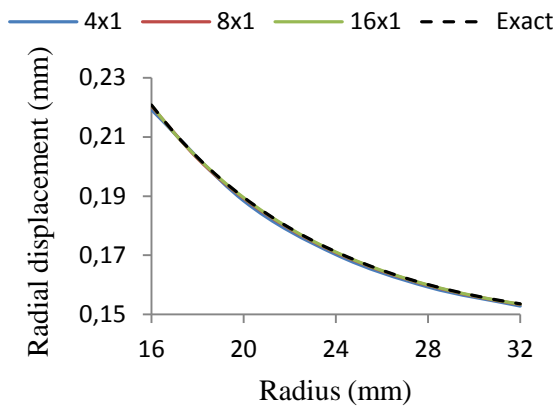


Figure 9. Two example FEM discretization for the pressurized thick cylinder (a) 4-element Ring4 discretization of a slice (b) 2-element Ring9 discretization of a slice

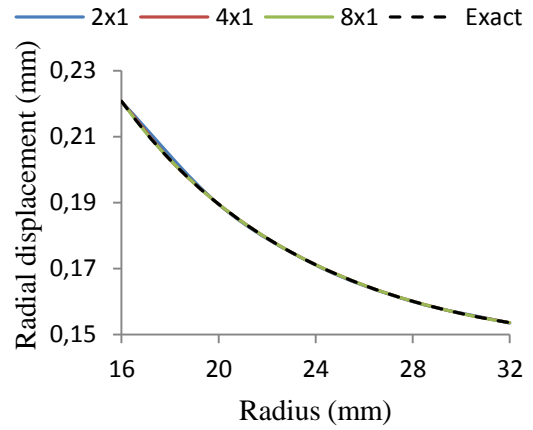
The exact stress distributions and radial displacement across the wall for a condition of plane strain in the z direction are (Timoshenko and Goodier, 1951):

$$\sigma_r = P \frac{a^2}{b^2 - a^2} \left(1 - \frac{b^2}{r^2} \right) \text{ and } \sigma_\theta = P \frac{a^2}{b^2 - a^2} \left(1 + \frac{b^2}{r^2} \right) \quad (142)$$

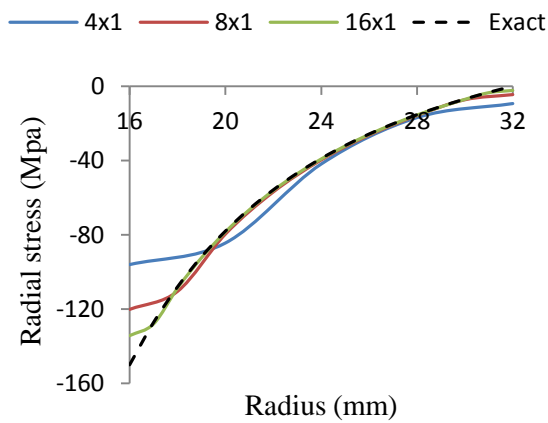
$$u_r = P \frac{a^2 (1 + \nu) (b^2 + r^2 (1 - 2\nu))}{E (b^2 - a^2) r} \quad (143)$$



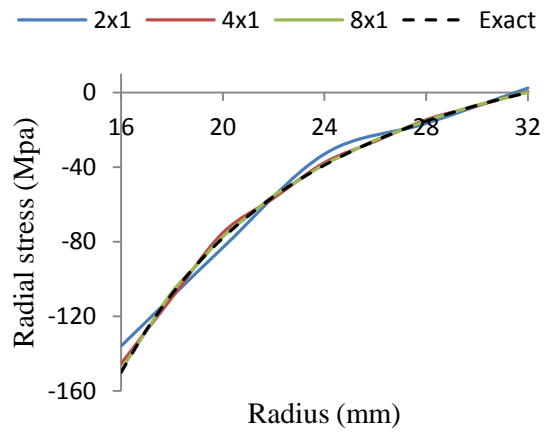
(a)



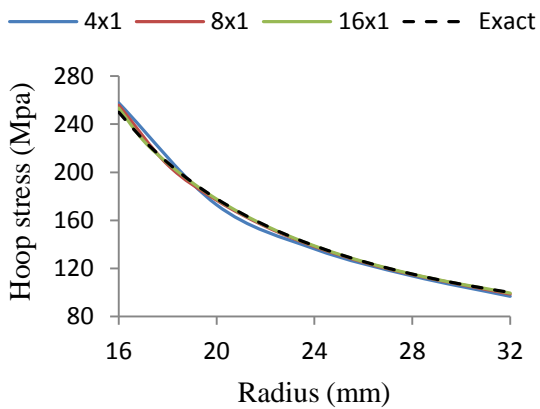
(d)



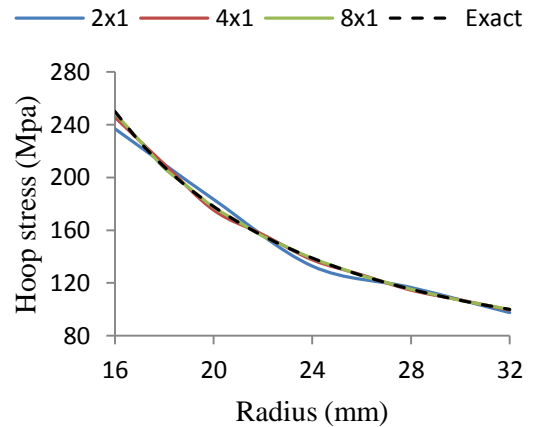
(b)



(e)



(c)



(f)

Figure 10. Computed versus exact (a) radial displacements (b) radial stresses (c) hoop stresses using Ring4 and (d) radial displacements (e) radial stresses (f) hoop stresses using Ring9 for different meshes of the pressurized hollow cylinder

The pressure lumping to the nodes on the inner radius $r = a$ depends on the type of the element such as $P_{r1} = P_{r2}$ for Ring4 and $P_{r2} = 4P_{r1} = 4P_{r3}$ for Ring9 elements. The subfigures in Fig.10 are obtained using two types of element (Ring4 and Ring9) with three radial discretizations. The numbers ($n_{er} \times n_{ez}$) given at the top of the figures show the number of elements used in radial (n_{er}) and axial (n_{ez}) directions. The latter is assumed to be 1 since the solution only depends on r . Example meshes are pictured in Fig.9 (a, b). Radial displacements u_r , radial stresses σ_r and hoop stresses or circumferential stresses σ_θ are graphically compared over the wall $a \leq r \leq b$ with the exact solutions in Fig.10.

As can be seen radial displacements and hoop stresses are satisfactorily predicted using both ring elements. The hole-edge radial stresses, however, are significantly underestimated using Ring4. For instance, for the 8x1 mesh of Ring4 radial stress $\sigma_r = -120\text{MPa}$ is obtained but the exact stress is $\sigma_r = -150\text{MPa}$. It seems to be a consequence of the impossibility of doing interelement stress averaging at that high stress gradient edge. For this low order model the variation of radial stress in r direction is limited to be constant within the element. Thus $\sigma_r = -120\text{MPa}$ may represent the stress at the center of the element. Increasing the number of elements in radial direction results better solutions as shown in Fig.10(b). The higher accuracy of the hoop stress is incidental, reflecting a property of plane axisymmetric solids under: the hoop strain $\varepsilon_\theta = u_r / r$ is not obtained through displacement differentiation. It thus attains the same accuracy as u_r . Ring9 produces closer radial stress results to the exact solution even for 2x1 mesh type as shown in Fig. 10(e). In other words, the computed radial stress is as good as can be expected from a linear variation over the element. Using eight Ring9 elements both radial and hoop stresses agree everywhere with the exact solution at plot accuracy.

If Poisson ratio is increased over zero, Ring4 results gradually lose accuracy if the number of elements are kept as 16 as shown in Fig. 11(a, b). In the limit $\nu \rightarrow 1/2$ the material approaches incompressibility, and the computed solution deterioration accelerates. This phenomenon is known as volumetric locking in FEM literature. Radial and hoop stresses are graphically compared over $a \leq r \leq b$ with the exact solution in Fig. 11(a, b). Serious deficiencies can be observed. All stress components violently oscillate as getting closer the inner boundary and the values taken are nonsensical. A minor stress oscillation can be observed at the outer boundary. For example, for $\nu = 0.485$ the radial stress

$\sigma_r = 48$ MPa at $r = a$ whereas it should be -150 MPa, so it even has the wrong sign. Using Ring9 elements in FEM modeling makes a big difference. For an 8-element mesh radial and hoop stresses are graphically compared over $a \leq r \leq b$ with the exact solution in Fig. 11(c, d). As can be seen neither volumetric locking nor stress oscillations are observed, and the stresses are well predicted everywhere. The agreement with the exact solution is excellent as shown in Fig. 11(c, d).

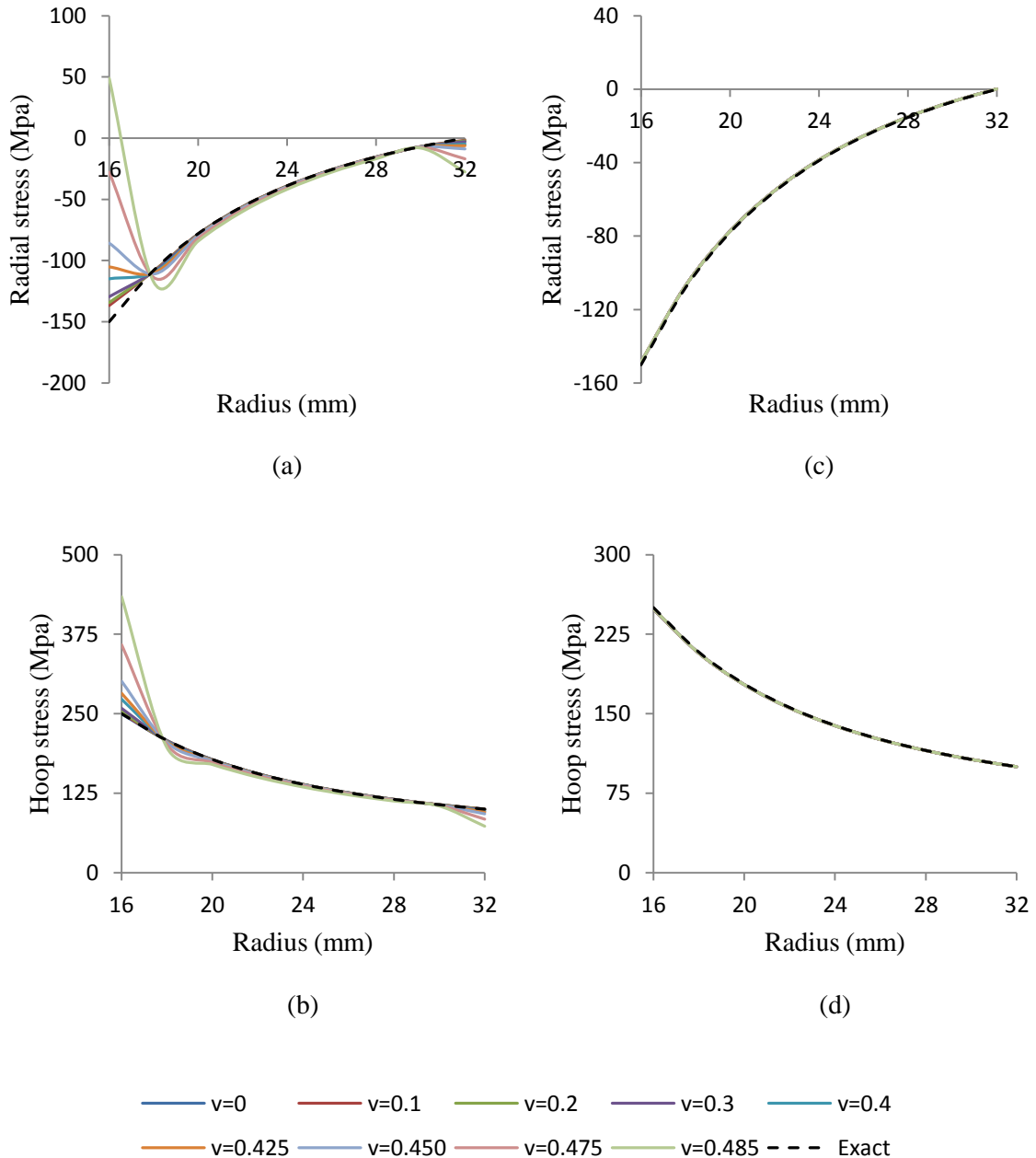


Figure 11. Computed versus exact (a) radial stresses (b) hoop stresses using Ring4 (c) radial stresses (d) hoop stresses using Ring9 for different Poisson's ratio

2.1.4. Rotating Thin Disc

The third verification problem is a hollow, thin circular disc of thickness $h=10\text{mm}$ inner radius $a=40\text{mm}$ and outer radius $b=100\text{mm}$, which spins about the z axis with constant angular frequency $\omega=1000$ rad/s. The material is isotropic with elastic modulus of $E=2 \times 10^{11}$ Pa and Poisson's ratio $\nu=0.3$ and mass density $\rho=7800$ kg/m³. The sample FEM discretizations are pictured in Fig. 12(a, b). The number of elements in radial direction is 4, 8 and 16 for Ring4 and 2, 4, and 8 for Ring9. Only one element is used in axial direction. Nodes are allowed to move radially. Unlike previous example movement in the axial direction is permitted to allow for disc thickness contraction due to Poisson ratio (Felippa, 2011). This motion is accommodated by constraining nodes in one of the constant z surfaces to be on rollers as shown in Fig.12 (a, b). All other nodes are left free. The only load is a centrifugal body force acting along direction r .

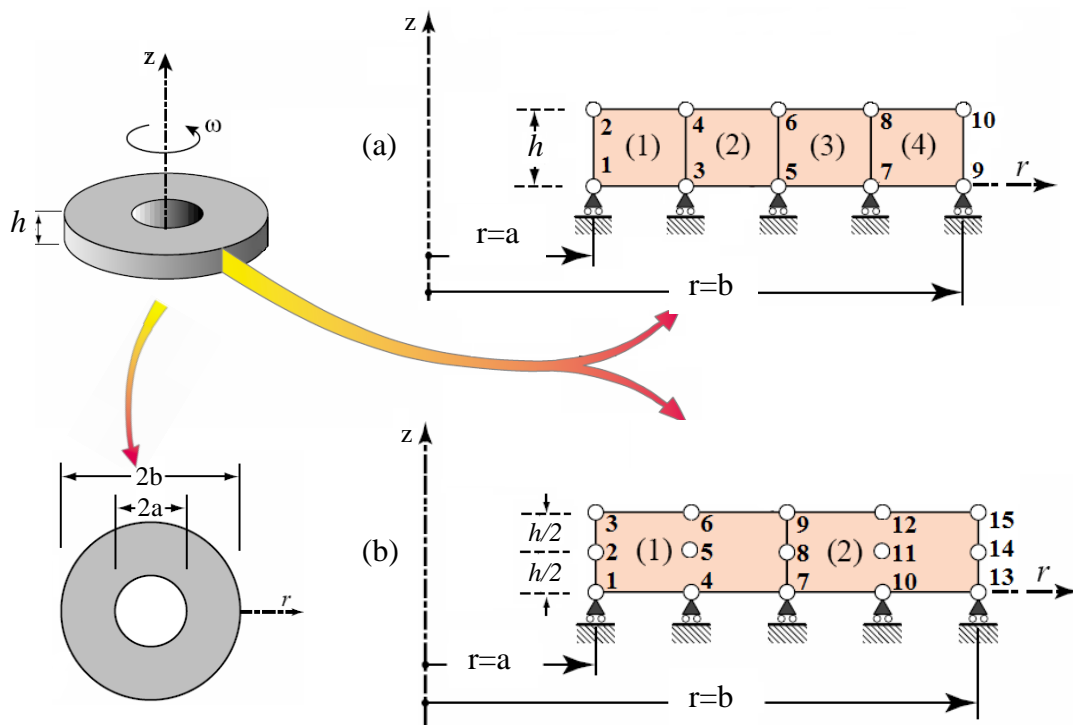


Figure 12. Two example FEM discretization for the rotating thin disc (a) 4-Ring4
(b) 2-Ring9 element discretization of disc section

When rotating about its axis with the angular velocity, all the particles of the disc will undergo a center-wise force. It is evident that the axial and tangential components of body force are zero in a spinning cylinder.

The exact radial displacement and stress distributions for a condition of plane stress in the z direction are (Timoshenko and Goodier, 1951):

$$u_r = \rho\omega^2 \frac{a^2(3+\nu)(r^2(1-\nu)+b^2(1+\nu))+r^2(1-\nu)(b^2(3+\nu)-r^2(1+\nu))}{8Er} \quad (144)$$

$$\sigma_r = \rho\omega^2 \frac{3+\nu}{8} \left(b^2 + a^2 - \frac{a^2b^2}{r^2} - r^2 \right) \quad (145)$$

$$\sigma_\theta = \rho\omega^2 \frac{3+\nu}{8} \left(b^2 + a^2 + \frac{a^2b^2}{r^2} - \frac{(1+3\nu)r^2}{3+\nu} \right) \quad (146)$$

Radial displacements u_r , radial stresses σ_r and hoop stresses σ_θ are graphically compared over $a \leq r \leq b$ with the exact solution in Fig. 13 for two ring types (Ring4 and Ring9) and three different meshes given at the top of the sub-figures. As can be seen for Ring4 with a mesh of 4×1 u_r and σ_θ are satisfactorily predicted as shown in Fig. 13(a, c). However, the radial stress is way of especially at the inner and outer boundaries, at which it should be zero. This may be again a consequence of the impossibility of doing interelement stress averaging there. Increasing number of element will result closer approximation to the exact solution as shown in Fig. 13(b). The analysis is redone with Ring9 again the same parameters are graphically compared over the radius with the exact solution as shown in Fig. 13(d, e, f). The computed radial stress is as good as can be expected from a linear variation over the element. The computed and exact radial displacements are agreed at nodes and therefore the hoop stress should also be exact at the nodes since $\sigma_\theta = Eu_r/r$. However, the extrapolation from Gauss points introduces discrepancies as can be seen in Fig. 13(f). In this example the effect of Poisson ratio is not considered. However, it should be noted that the volumetric locking is less of a problem in such case since the plane stress condition allows lateral expansion and contraction (Felippa, 2011).

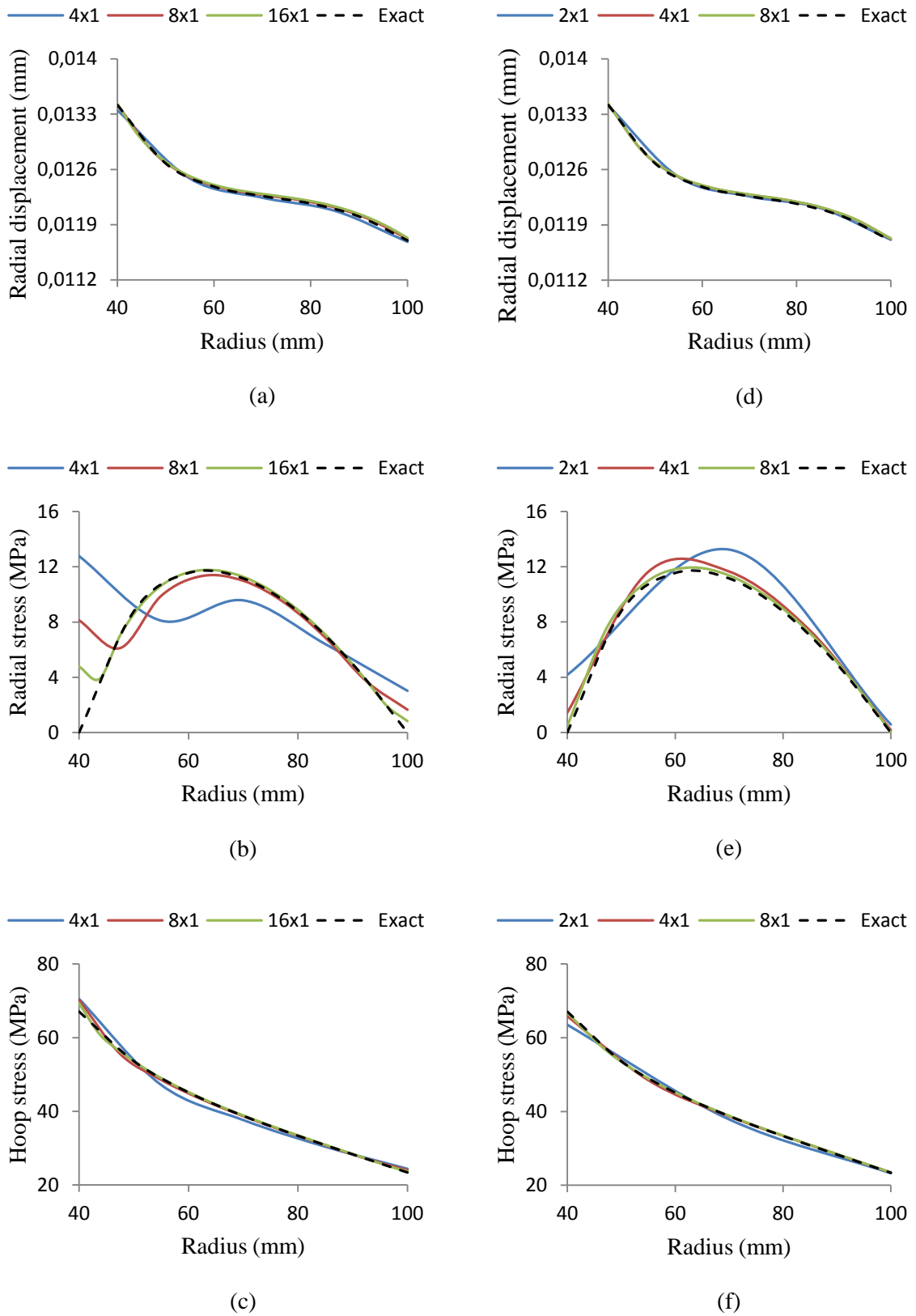


Figure 13. Computed versus exact (a) radial displacements (b) radial stresses (c) hoop stresses using Ring4 and (d) radial displacements (e) radial stresses (f) hoop stresses using Ring9 for different meshes of the rotating thin disc

2.1.5. Circular Plate Bending

The last verification problem is a simply supported circular plate bent by a lateral point load and uniformly distributed load. The plate has radius of $R=10m$. and thickness $h=1m$. The point load of magnitude $P=500\text{ kN}$ acts downward at the plate center and uniformly distributed load of magnitude $P_o=5\text{ kN/m}^2$ acts downward. The material is isotropic with elastic modulus $E=30000\text{ MPa}$ and Poisson's ratio $\nu=0.2$. Two FEM discretizations are pictured in Fig. 14(a, b). For the Ring4 element type 4x2, 8x2 and 16x2 discretizations are used, whereas for Ring9 the meshes are 2x1, 4x1 and 8x1. Nodes are allowed to move in the z direction except those on the edge at $r=R$. The nodes at $r=0$ must be constrained against radial motion because of axial symmetry. The resulting support conditions are shown in Fig. 14(a, b). The central point load appropriately lumped to the nodes on the z axis.

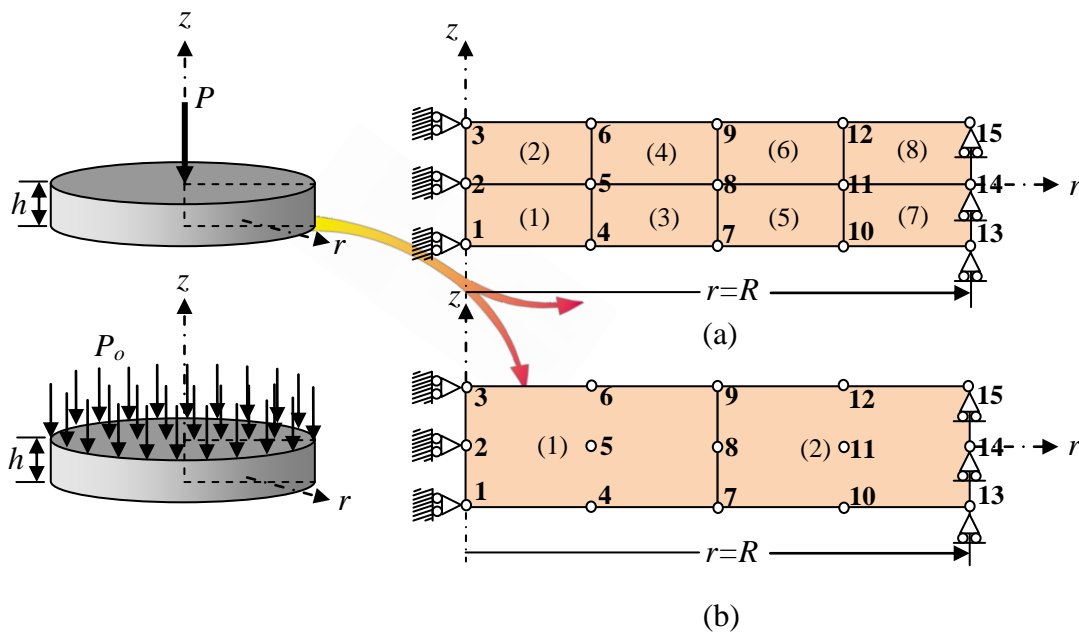


Figure 14. Two example FEM discretization for the circular plate bending (a) 8-Ring4 (b) 2-Ring9 element discretization

The exact solution for a Kirchhoff plate model of this problem for centered point load gives axial displacement and radial stress as (Ugural, 1981):

$$u_z = \frac{P}{16\pi D^*} \left[2r^2 \ln \frac{r}{R} + \frac{3+\nu}{1+\nu} (R^2 - r^2) \right] \quad \text{where } D^* = \frac{Eh^3}{12(1-\nu^2)} \quad (147)$$

$$\sigma_r = \frac{3Pz}{\pi h^3} (1+\nu) \ln \frac{R}{r} \quad (148)$$

The axial displacement u_z does not depend on z , which follows from the Kirchhoff thin plate theory assumptions. The values shown as exact for radial stresses are actually evaluated from Kirchhoff solution using Eq.12 at $r=R/1000=1/100$, since this equation have logarithmic singularity as $r \rightarrow 0$. And radial stresses are computed at the lower or upper plate surfaces $z = h/2$. Axial displacements and radial stresses are graphically compared over $a \leq r \leq b$ with the exact solution in Fig. 15 and Fig. 16 for the point load at the center of the circular plate, respectively.

The axial displacements have the right shape but are under-predicted using Ring4 elements as shown in Fig. 15(a). This is a mild case of the so-called “shear locking”: a significant amount of element energy is spend in shear resulting in over stiffness (Felippa, 2011). The effect would get worse if the thickness-to-diameter ratio is decreased. This shear locking effect will be investigated in detail for different thicknesses-to-diameter ratios. Considering the coarse mesh the stress predictions seem to be good sufficiently away from the plate center, say for $r > 2m$. Increasing element mesh alleviates the shear locking but the displacement is still somewhat under-predicted. The stress distributions away from the center are improved but the singularity is still poorly captured using 16x2 mesh of Ring4 element as shown in Fig. 16(a).

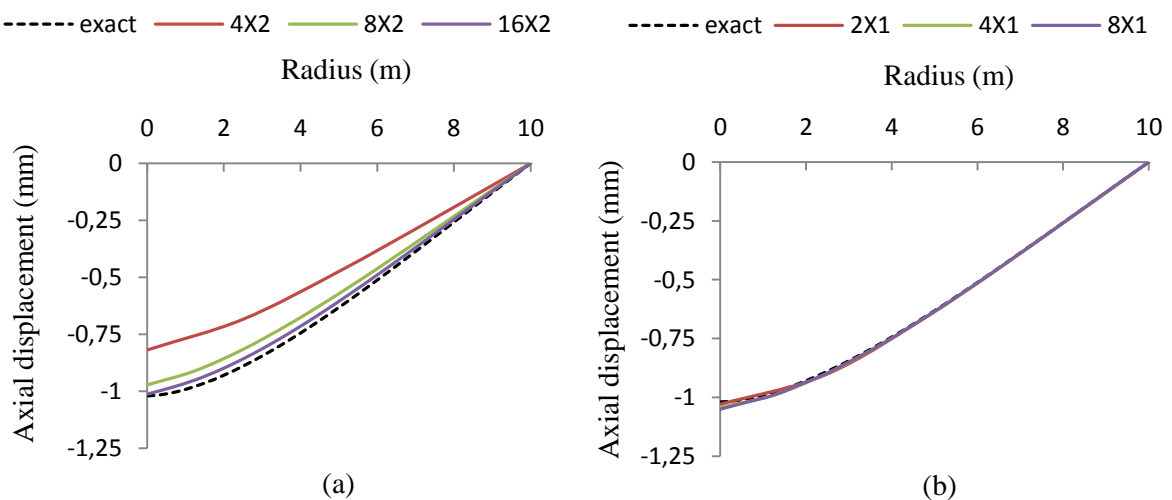


Figure 15. Point loaded circular plate: axial displacements for (a) element meshes of Ring4 and (b) element meshes of Ring9

The analysis is repeated for Ring9 with half the elements: 2, 4 and 8 respectively in radial direction, and only one element in the axial direction. From Fig. 15(b) it can be seen that the transverse or axial displacement is well captured since the element does not suffer from shear locking. The stress distribution is fine away from the center. Capturing the singularity is obviously difficult with 2 elements. Increasing number of elements results stresses fairly close to the singularity as shown in Fig. 16(b).

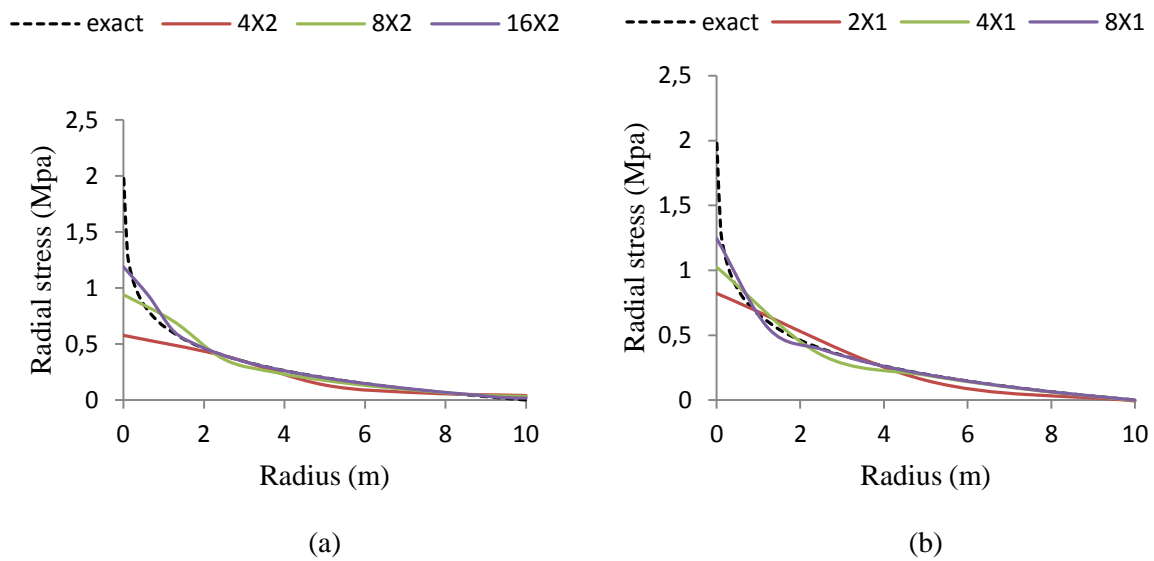


Figure 16. Point loaded circular plate: radial stresses for (a) element meshes of Ring4 and (b) element meshes of Ring9

As briefly explained before the shear locking phenomenon is characterized by a severe underestimation of the displacements, i.e. the structure is too stiff. The word “locking” means that the structure “locks” itself against deformations. Also, locking means the effect of a reduced rate of convergence for coarse meshes in dependence of a critical parameter (Felippa, 2011). In our case the critical parameter is the ratio of thickness to diameter of the circular plate, H/D . To investigate the effect of the parameter, a circular plate under uniformly distributed load with simple supports along the edge is analyzed for different thicknesses to diameter ratios. The Figs. 17 and. 18 show the convergence rates of the center deflection and center radial stress at the bottom of the plate with increasing number of elements for four different ring elements, respectively. These are the bilinear 4 node element with full integration Ring4(FI) and selectively reduced integration

Ring4(SRI) and the biquadratic 9 node element with full integration Ring9(FI) and selective reduced integration Ring9(SRI).

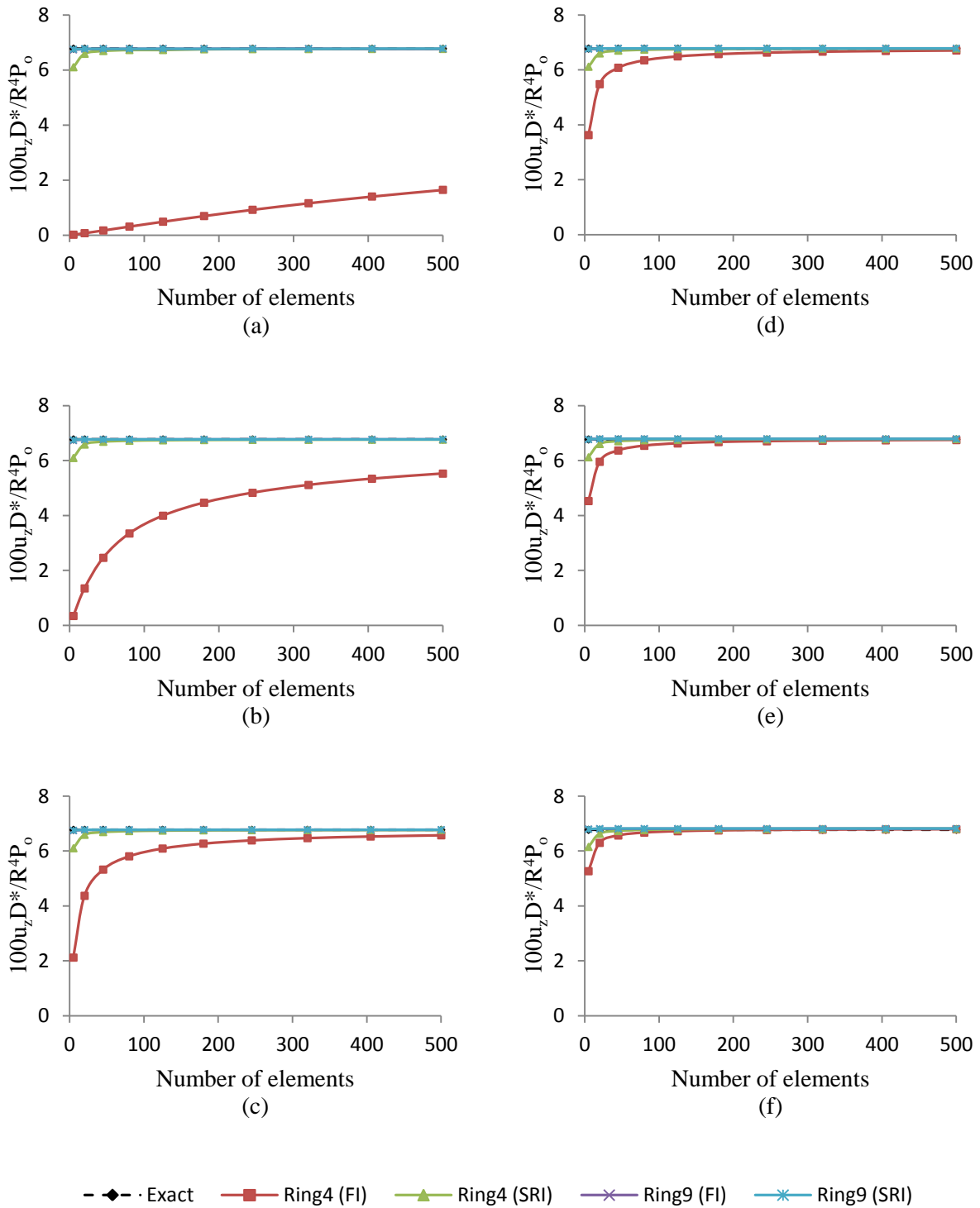


Figure 17. Dimensionless center axial displacement versus number of elements for various thickness to diameter ratios (a) $H/D=0.001$ (b) $H/D=0.005$ (c) $H/D=0.015$ (d) $H/D=0.025$ (e) $H/D=0.035$ (f) $H/D=0.05$

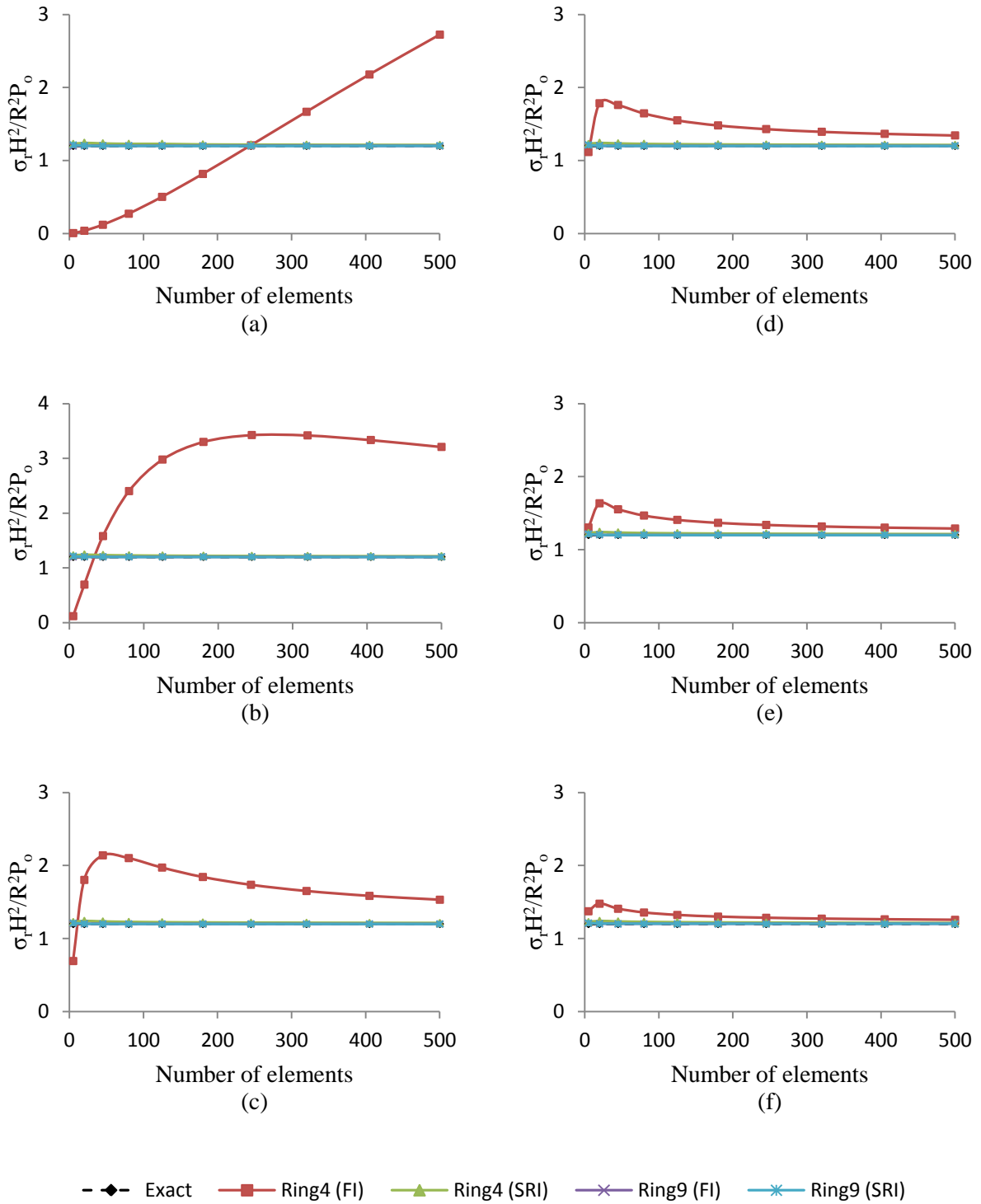


Figure 18. Dimensionless center radial stresses versus changing number of elements for various thickness to diameter ratios (a) $H/D=0.001$ (b) $H/D=0.005$ (c) $H/D=0.015$ (d) $H/D=0.025$ (e) $H/D=0.035$ (f) $H/D=0.05$

In selectively reduced integration procedure the shear strain terms are integrated using reduced Gauss points. In other words, in the stiffness formulations the normal strain terms are integrated using 2x2 and 3x3 Gauss points whereas the shear strain terms are integrated using 1x1 and 2x2 points for Ring4 and Ring9, respectively. In full integration technique all terms are integrated using the same number of Gauss points required for the exact evaluation of integrals i.e. 2x2 and 3x3 Gauss points for Ring4 and Ring9, respectively.

For practical applications the most important efficiency aspect of a certain finite element scheme is coarse mesh accuracy. This is important for the absolute error to be small at low computational expense. However, as shown in Figs. 17 and 18 the rate of convergence of the Ring4 (FI) is too slow below a certain limit of thickness to diameter ratio. In Fig. 17(a) it can be easily seen that the required number of elements for an acceptable convergence of the element Ring4(FI) to the exact solution is too large for the small ratio of $H/D=0.001$. As this number is often beyond available computer capacities there is strong interest to avoid such locking effects. As can be seen from Figs. 17 and 18 increasing the ratio of thickness to diameter accelerates the convergence rate of the Ring4 (FI). However, it possible to reach an optimal rate of convergence for coarse meshes using the selectively reduced element Ring4(SRI) in the analysis of even very thin plates as shown in Figs. 17(a) and 18(a). It can be realized from Figs. 17 and 18 that the convergence of Ring4(SRI) is uniform with respect to thickness to diameter H/D ratio.

It is a fact that rate of convergence is still smaller than the elements Ring9(FI) and Ring9(SRI) since these are the higher-order elements based on quadratic shape functions. As can be seen from Figs. 17 and 18 the performance of Ring9(FI) is extremely good, showing no signs of shear locking. However, for different loading and boundary conditions its performance can be improved when its shear strain energies are integrated in a selective sense as explained previously. Using Ring9(FI) or Ring9(SRI) in the analysis of circular plate, displacement and radial stresses can be obtained with the same accuracy and rate of convergence for coarse meshes. The rate of convergence of these elements is independent of the thicknesses to diameter ratios, H/D .

The exact solutions plotted in Figs. 17, 18, 19, and 20 are obtained using Kirchhoff thin plate theory. In Figs. 19 and 20, dimensionless center displacements and radial stresses are plotted versus the thickness to diameter ratios, respectively.

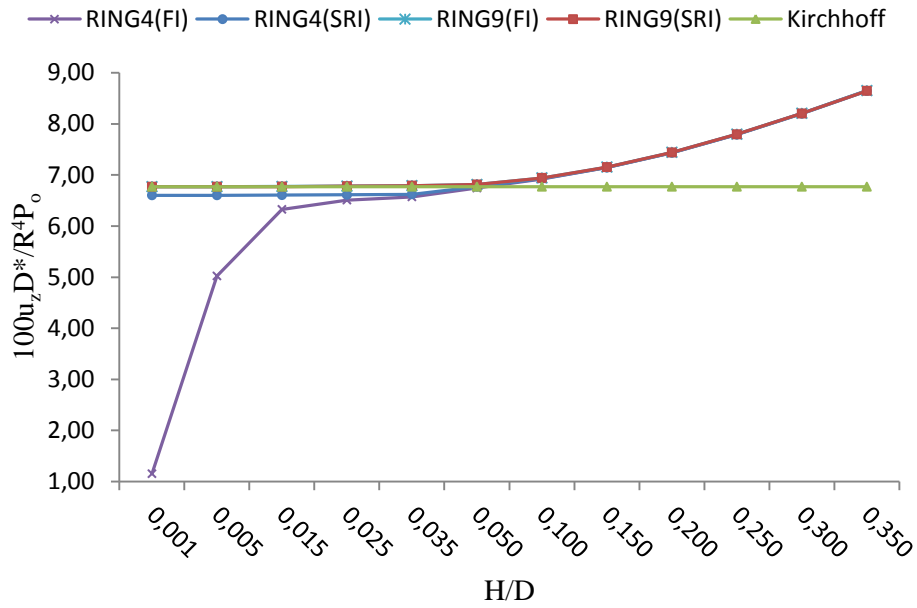


Figure 19. Dimensionless center axial displacements of the simply supported circular plate under uniformly distributed load

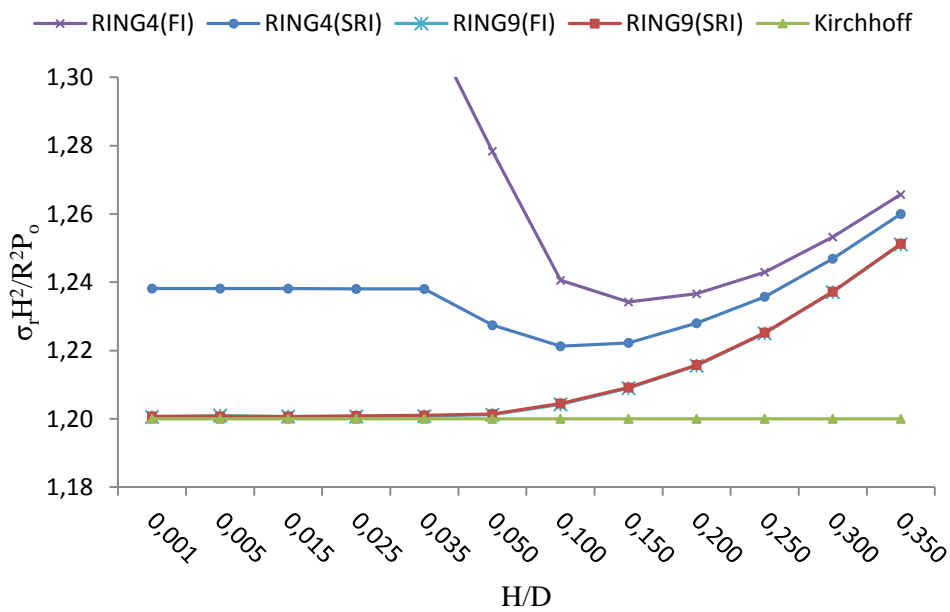


Figure 20. Dimensionless center radial stresses at the bottom surface of the the simply supported circular plate under uniformly distributed load

Again four types of ring elements are used in the analysis of the circular plate for different thicknesses. As can be seen from Figs. 19 and 20 that all lines intersect or come so close to each other at the ratio of $H/D=0.05$ for center displacements and $H/D=0.1$ for

radial stresses. That means that above these certain limits shear locking disappears for elements that suffer from locking. Also it can be observed from Figs. 19 and 20 that below the limit of $H/D=0.05$ the displacement and stress values of elements Ring9(FI) and Ring9(SRI) coincide with the values of Kirchhoff thin plate theory while above this limit values obtained using these elements move away from the Kirchhoff solution. Therefore, it can be concluded that the ignorance of the transverse shear deformations for circular plates above the limit ratio $H/D=0.05$ produces incorrect results in Kirchhoff thin plate theory. Moreover from Figs. 19 and 20 it can be concluded that Ring4(SRI) can be used as a locking free element. However, the absolute errors of locking free elements such as Ring9(FI) and Ring9(SRI) are much smaller due to the order of the shape functions used in the formulations as shown in Figs. 19 and 20. Table 4 and 5 present the dimensionless values of center axial displacements and center radial stresses at the bottom of the circular plates respectively for various thicknesses to diameter ratios or for different thin circular plates (below $H/D=0.05$) and for thick circular plates (above $H/D=0.05$) with the given number of elements in axial and radial directions.

Table 4. Dimensionless center displacement values of the simply supported circular plate under uniformly distributed load for various thickness/diameter ratios and integration techniques

H/D	RING4	RING9	RING4	RING9	RING4	RING9
	FI	FI	SRI	SRI	Mesh ($n_{er} \times n_{ez}$)	Mesh ($n_{er} \times n_{ez}$)
$100u_z D^* / (P_0 R^4)$						
0,001	1,1527	6,7674	6,6027	6,7698	40x2	20x1
0,005	5,0230	6,7686	6,6030	6,7702	40x2	20x1
0,015	6,3267	6,7726	6,6063	6,7731	40x2	20x1
0,025	6,5085	6,7805	6,6128	6,7807	40x2	20x3
0,035	6,5703	6,7910	6,6225	6,7911	40x2	20x3
0,050	6,7442	6,8131	6,7686	6,8132	40x4	20x3
0,100	6,9233	6,9426	6,9259	6,9426	40x7	20x6
0,150	7,1460	7,1541	7,1444	7,1541	40x10	20x6
0,200	7,4366	7,4415	7,4334	7,4415	40x12	20x6
0,250	7,7941	7,7956	7,7898	7,7956	40x16	20x7
0,300	8,2039	8,2037	8,1991	8,2037	40x20	20x8
0,350	8,6488	8,6474	8,6434	8,6473	40x24	20x10

Table 5. Dimensionless radial stress values at the bottom of the simply supported circular plate under uniformly distributed load for various thickness/diameter ratios and integration techniques

H/D	RING4	RING9	RING4	RING9	RING4	RING9
	FI	FI	SRI	SRI	Mesh	Mesh
$\sigma_r H^2 / P_0 R^2$					($n_{er} \times n_{ez}$)	($n_{er} \times n_{ez}$)
0,001	1,7466	1,2006	1,2382	1,2007	40x2	20x1
0,005	3,4882	1,2010	1,2382	1,2007	40x2	20x1
0,015	1,6564	1,2007	1,2381	1,2007	40x2	20x1
0,025	1,3942	1,2007	1,2381	1,2009	40x2	20x3
0,035	1,3183	1,2008	1,2380	1,2010	40x2	20x3
0,050	1,2784	1,2012	1,2274	1,2014	40x4	20x3
0,100	1,2406	1,2042	1,2213	1,2045	40x7	20x6
0,150	1,2342	1,2090	1,2223	1,2092	40x10	20x6
0,200	1,2366	1,2156	1,2280	1,2158	40x12	20x6
0,250	1,2430	1,2251	1,2358	1,2253	40x16	20x7
0,300	1,2532	1,2371	1,2469	1,2372	40x20	20x8
0,350	1,2657	1,2511	1,2600	1,2513	40x24	20x10

2.2. Analysis of a Cooling Tower

The algorithms utilized in the analyses of some simple axisymmetric structures are employed towards demonstration of their applicability to an important practical problem. For this, the natural draught hyperbolic cooling tower is considered. The natural draught cooling tower is a very important and essential component in the thermal nuclear power stations and industrial power plants. Due to their complexities in geometry, the analysis of such type of structures has attracted attention of many researchers throughout the world.

Static responses under quasi-static wind loading, free vibration and seismic responses of an existing hyperbolic cooling tower at Stanwell Power Station, located west of Rockhampton in Queensland (Australia) are investigated. Additionally, the influences of thickness, height and curvature on free vibration and seismic responses are examined.

For the finite element discretization of the cooling tower Ring 9 element is used due to its advantages over the Ring4 as explained in the previous sections.

2.2.1. Geometry and Material Properties of the Cooling Tower

The cooling tower is a 121.5 m-high with base, throat and top radii of 45.30 m, 27.89 m and 29.02 m respectively, with the throat located 95.6 m above the base of the shell. A constant shell-wall thickness of 240 mm, and reinforced concrete with a unit weight of 25 kN/m³, Poisson's ratio of 0.2 and elastic modulus of 39 GPa are considered for the finite element numerical model. The geometry and some elements of the hyperbolic cooling tower are depicted in Fig. 21.

The equation of the generating curve of the cooling tower in the form of a hyperboloid of revolution is obtained by setting the parameters $a=27.89\text{m}$, is the throat radius, since the hyperbolic curve has double curvature meeting at the throat the characteristic dimension is evaluated for the upper and lower portions of the curve as $b_H=90.07\text{ m}$ and $b_U=74.69\text{ m}$, by substituting the base (d_U, Z_U) and the top (d_H, Z_H) coordinates.

$$b_H = \frac{aZ_H}{\sqrt{(d_H/2)^2 - a^2}} \quad \text{and} \quad b_U = \frac{aZ_U}{\sqrt{(d_U/2)^2 - a^2}} \quad (149)$$

and the origin is located on the shell axis at the throat level as $r_c=0\text{ m}$, and $z_c=95.6\text{ m}$ in Table 1. The shape parameter

$$K=k^2 = \left(1 + \frac{a^2}{b^2} \right) \quad (150)$$

is an indicator of the deviation of the profile from the degenerate case of the cylinder ($k^2=1$), with a larger k corresponding to a more pronounced curvature of the meridian.

This form falls into the class of structures known as thin shells. The cross section as shown in Fig. 21 depicts the ideal profile of the shell generated by rotating the hyperboloid $R=f(Z)$ about the vertical z axis. The coordinate z is measured from the lintel base. All dimensions in the r - z plane are specified on the reference surface, the inner surface of the shell. Dimensions through the thickness are then referred to this surface. The important elements of the shell include the columns at the base, which provide the necessary opening

for the air; the lintel, either a discrete member or more often a thickened portion of the shell, which is designed to distribute the concentrated column reactions into the shell wall; the shell wall which may be with varying thickness; and the cornice, which like the lintel may be discrete or a thickened portion of the wall designed to stiffen the top against ovaling.

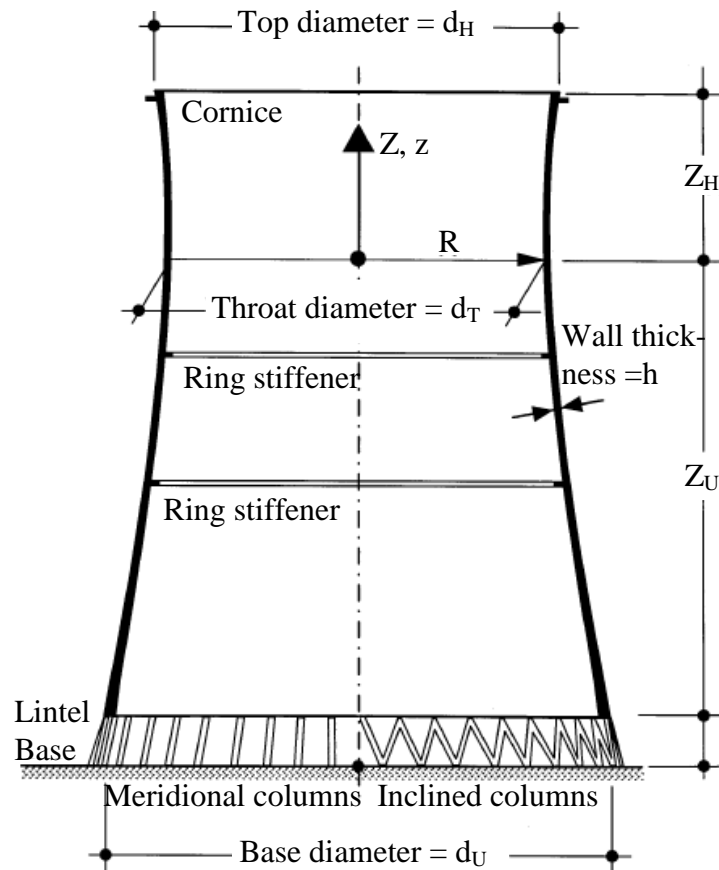


Figure 21. Geometry and elements of a cooling tower

2.2.2. Loadings of the Cooling Tower

Hyperbolic cooling towers may be subjected to a variety of loading conditions. Most commonly, these are dead load, wind load, earthquake load, temperature variations, construction loads, and settlement. In the scope of this study dead, wind and earthquake loads are considered. Dead load consists of the self-weight of the shell wall only.

2.2.2.1. Wind Loadings

Wind loading is extremely important in cooling tower design for several reasons. First of all, the amount of reinforcement, beyond a prescribed minimum level, is often controlled by the net difference between the tension due to wind loading and the dead load compression, and is therefore especially sensitive to variations in the tension. Secondly, the quasi-static velocity pressure on the shell wall is sensitive to the vertical variation of the wind, as it is for most structures, and also to the circumferential variation of the wind around the tower, which is peculiar to cylindrical bodies. Vertical and circumferential variations of the wind loading to be considered in the static analysis of the cooling tower are obtained in accordance with two codes or standards, Turkish Standards (TS 498) and Eurocode (EN 1991-1-4:2005).

The external wind pressure acting at any point on the shell surface is computed as

$$q(z, \theta) = q(z)H(\theta) \quad (151)$$

in which $q(z)$ is the effective velocity pressure at a height z above the ground level and $H(\theta)$ is the coefficient for circumferential distribution of the external wind pressure. As mentioned above $q(z)$ and $H(\theta)$ are obtained from applicable codes TS 498 and Eurocode. Figs. 22 and 23 depict the vertical variations of effective velocity pressure, $q(z)$ in accordance with TS 498 and Eurocode, respectively. While the effective velocity pressure distribution throughout the height of the cooling tower varies uniformly in stepwise as shown in Fig. 22 according to TS 498 the pressure distribution changes parabolically according to Eurocode as shown in Fig. 23. Additionally, the maximum effective velocity pressure is calculated as 2080 N/m/m according to TS 498 whereas it is 1634 N/m/m according to Eurocode at the top of the cooling tower.

The circumferential distribution of the wind pressure is denoted by $H(\theta)$ and is shown in Figs. 24 and 25 in accordance with TS 498 and Eurocode respectively for the half portion of the cooling tower since it is symmetric with respect to plane passing through the key region, the windward meridian $\theta = 0^\circ$. The wind pressure distribution coefficient over a circular section is sinusoidal in the first and fourth quadrant in TS 498 as depicted in Fig.24.

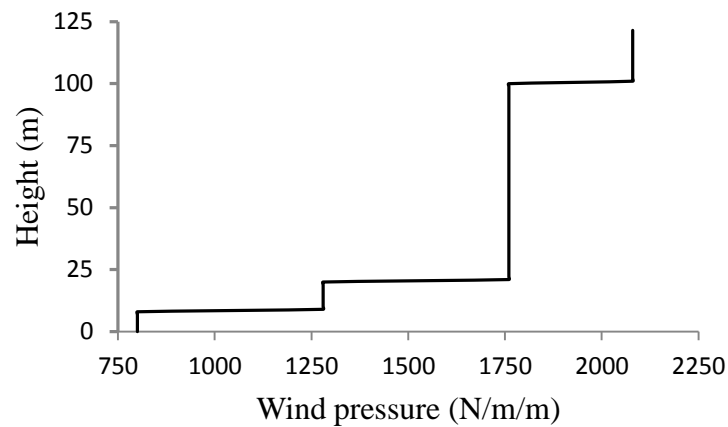


Figure 22. The wind pressure distribution over the height of the cooling tower according to TS 498

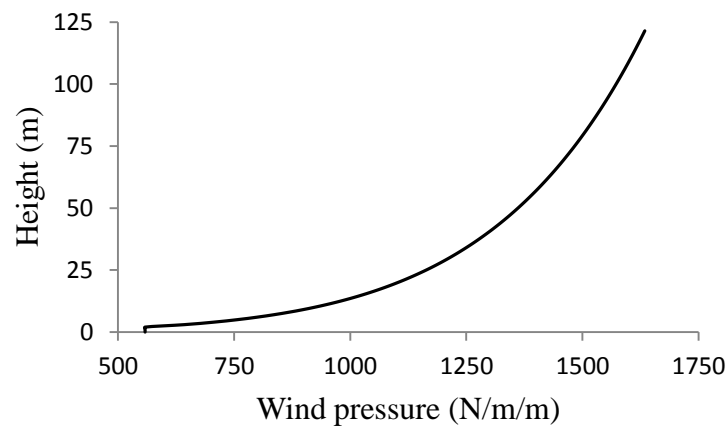


Figure 23. The wind pressure distribution over the height of the cooling tower according to Eurocode

There is no suction over the circular section and compressive pressure is applied over the half of the section according to TS 498 as shown in Fig. 24 whereas in Eurocode the large portion of the load over the circular section is suction as shown in Fig. 25. It should be noted that the wind pressure distribution coefficients do not change with the height of the cooling tower for the simplicity. For quantitative purposes, the equations of the pressure distribution curve for Eurocode are given in Table 6. In Eurocode the functions of the pressure distribution curve change according to surface roughness. The curve called as K1.3 is chosen and shown in Fig. 25.

Table 6. Functions of pressure coefficient distribution curve in Eurocode

Curve	Minimum pressure	$\theta \leq 73^\circ$	$\theta \leq 93^\circ$	$\theta > 93^\circ$
K1.3	-1.3	$1 - 2.3 \left(\sin \frac{90}{73} \theta \right)^{2.166}$	$-1.3 - 0.8 \left[\sin \left[\frac{90}{73} (\theta - 73) \right] \right]^{2.395}$	-0.5

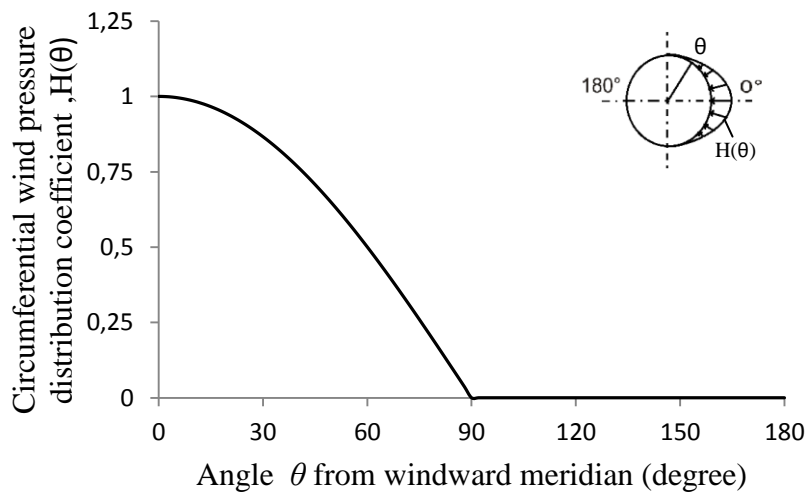


Figure 24. Circumferential wind pressure distribution coefficients according to TS 498

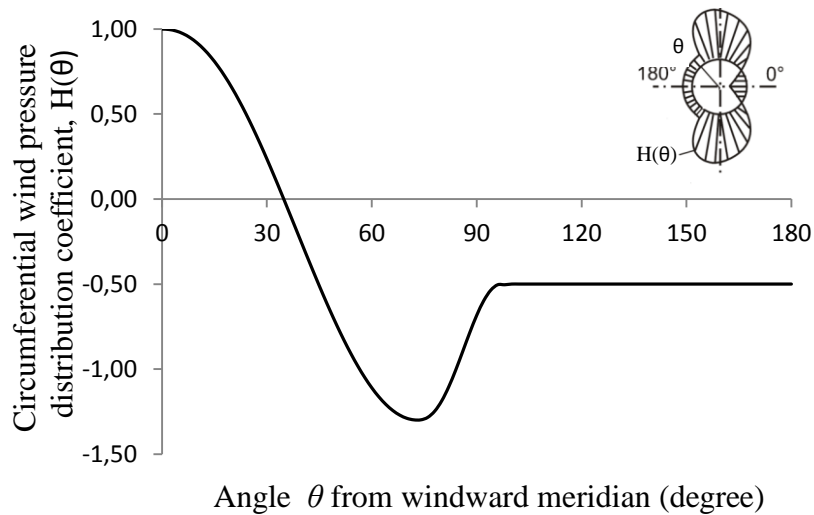


Figure 25. Circumferential wind pressure distribution coefficients according to Eurocode

If the distribution $H(\theta)$ is represented in a Fourier cosine series of the form

$$H(\theta) = \sum_{m=0}^{\infty} A_m \cos m\theta \quad (152)$$

the Fourier coefficients A_m for distributions most similar to curves shown in Figs. 24 and 25 are given in Table 7.

Table 7. Coefficients of Fourier harmonics for the circumferential distribution of the wind load according to TS 498 and Eurocode

m	TS 498	EN 1991-1-4: 2005
	A_m	
0	0.3183	-0.3922
1	0.4937	0.2602
2	0.2122	0.6024
3	0	0.5046
4	-0.0424	0.1064
5	0	-0.0948
6	0.0182	-0.0186
7	0	0.0468

The distributions are approximated by using eight harmonics with the given coefficients in Table 7. The relatively large Fourier coefficients associated with $m=2,3,4,5$ for Eurocode indicate that a significant portion of the loading will cause shell deformations in these modes to be explained later. In turn, the corresponding local forces are significantly higher than a beam-like response would produce. On the contrary, for TS 498 the largest coefficient is obtained for $m=1$ which is the translational mode causes beam-like response.

The Fourier harmonics of the wind load distribution over the circumferential direction according to TS 498 and Eurocode are plotted in Fig. 26 and Fig. 28, respectively. The Fig. 27 and Fig. 29 depict the combination of these eight harmonics or

Fourier approximation and the actual wind load distribution. It can be concluded that good approximations are obtained using eight harmonics with the given coefficients in Table 7 for both TS 498 and Eurocode.

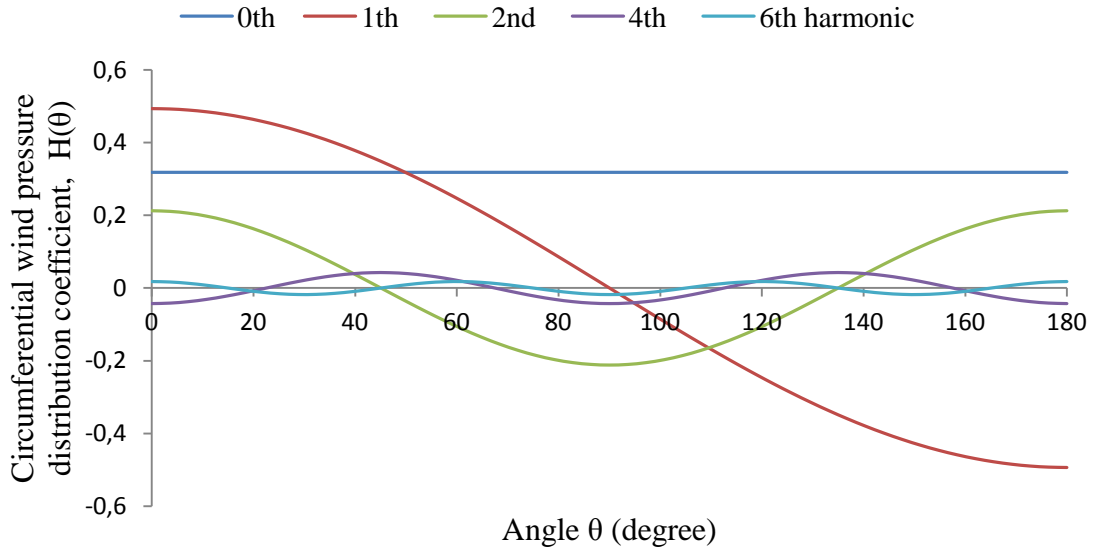


Figure 26. Fourier harmonics used to represent the wind load distribution coefficient over the circular section of the cooling tower for TS 498

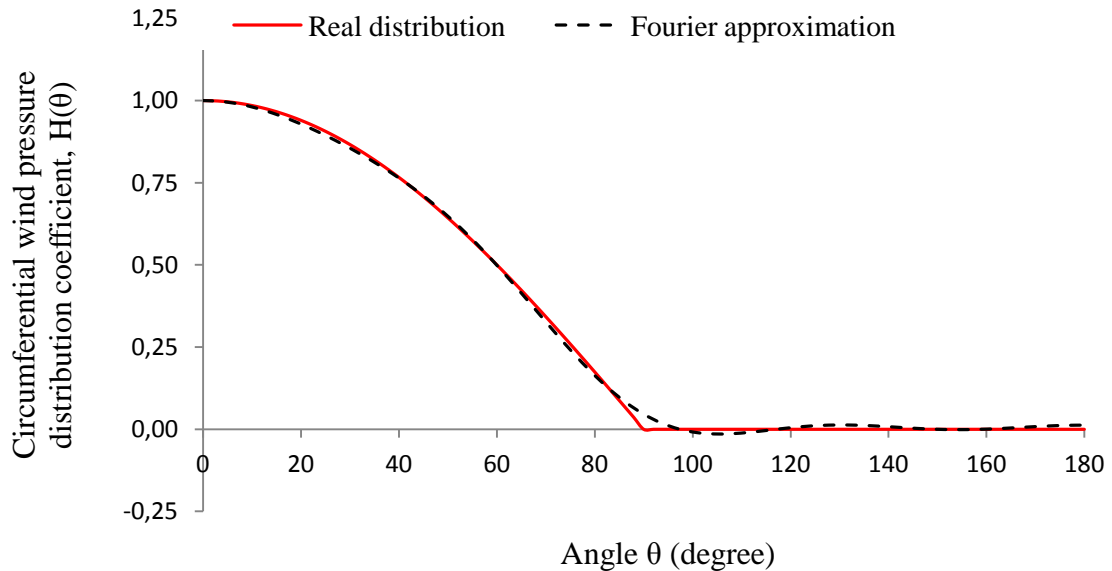


Figure 27. Real distribution and Fourier approximation of the wind load distribution coefficients using eight Fourier harmonics for TS 498

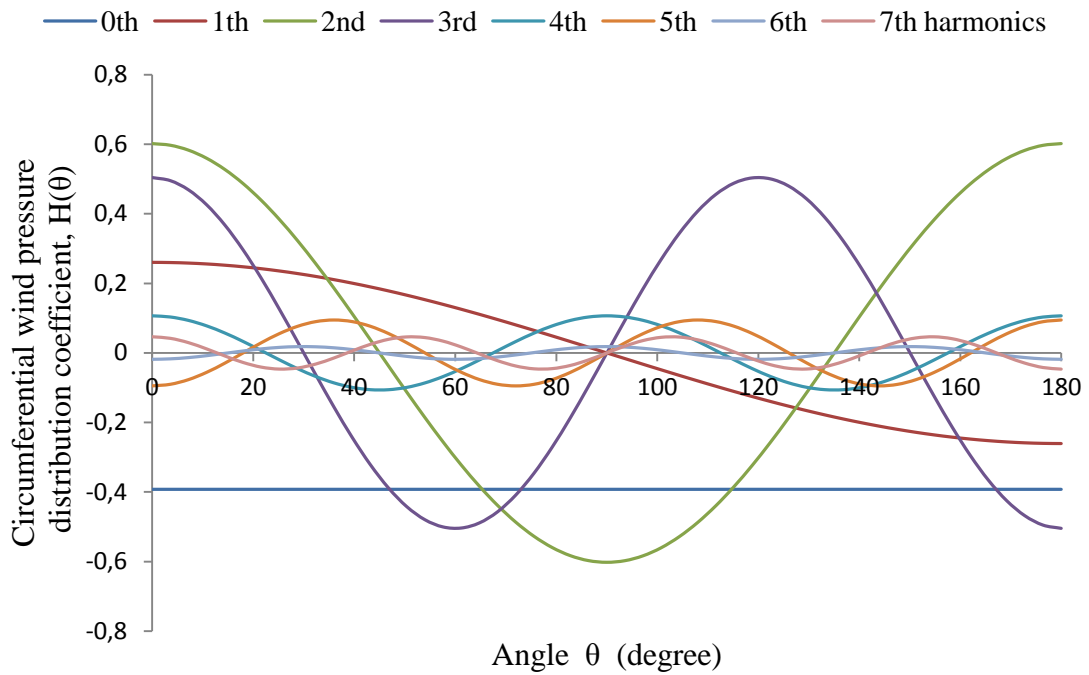


Figure 28. Fourier harmonics used to represent the wind load distribution coefficient over the circular section of the cooling tower for Eurocode

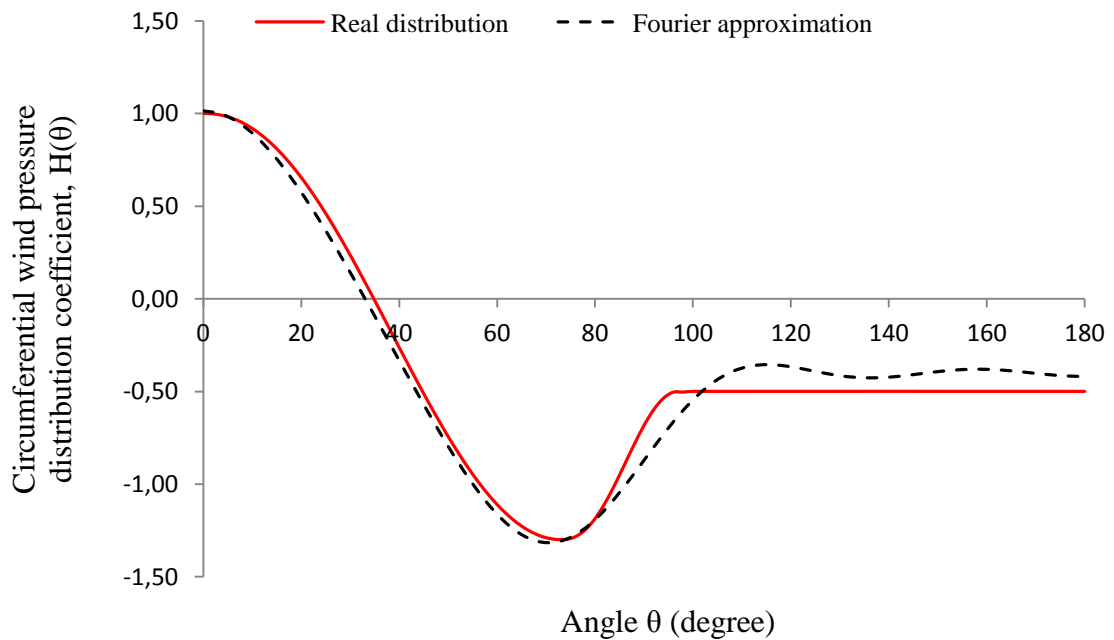


Figure 29. Real and Fourier approximations of the wind load distribution coefficients using eight Fourier harmonics for Eurocode

2.2.2.2. Earthquake Loading

Earthquake loading on hyperbolic cooling towers is produced by ground motions transmitted from the foundation through the supporting columns and the lintel into the shell. If the base motion is assumed to be uniform vertically and horizontally, the circumferential effects are axisymmetrical ($m=0$) and antisymmetrical ($m=1$), respectively. The magnitude of the earthquake induced forces is a function of the mass of the tower and the acceleration produced by the earthquake at the base of the structure. Seismic loads are modeled in the finite element time history analysis as ground accelerations applied at the base of the structure, and the response is analyzed by direct integration, Newmark integration, using time history records. Transient response of the Stanwell hyperbolic cooling tower to earthquake loading is analyzed by direct integration using time history records of Düzce earthquakes as plotted in Fig. 30. The Düzce earthquake occurred on 12th November, 1999 in Turkey, and had the peak accelerations between 5.-10.seconds of the record as seen from Fig. 30. The maximum acceleration is 3.73 m/s^2 in the East-West direction. The time step of the record is 0.005s. Since the dynamic analysis is time consuming for small time steps and large period of time accelerations between 5-10 seconds of the complete record are considered in the dynamic analysis of the cooling tower. The considered time history of the Düzce earthquake is shown in Fig. 31.

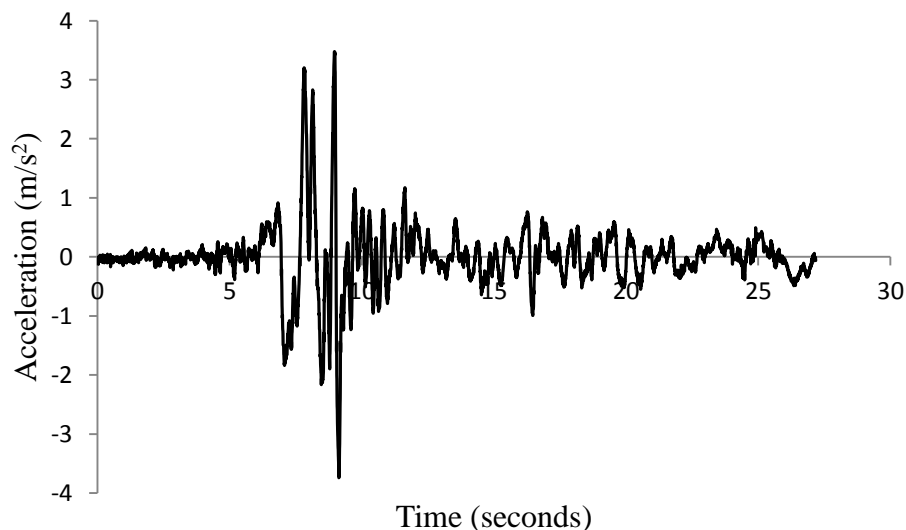


Figure 30. Acceleration versus time history record of the Düzce earthquake

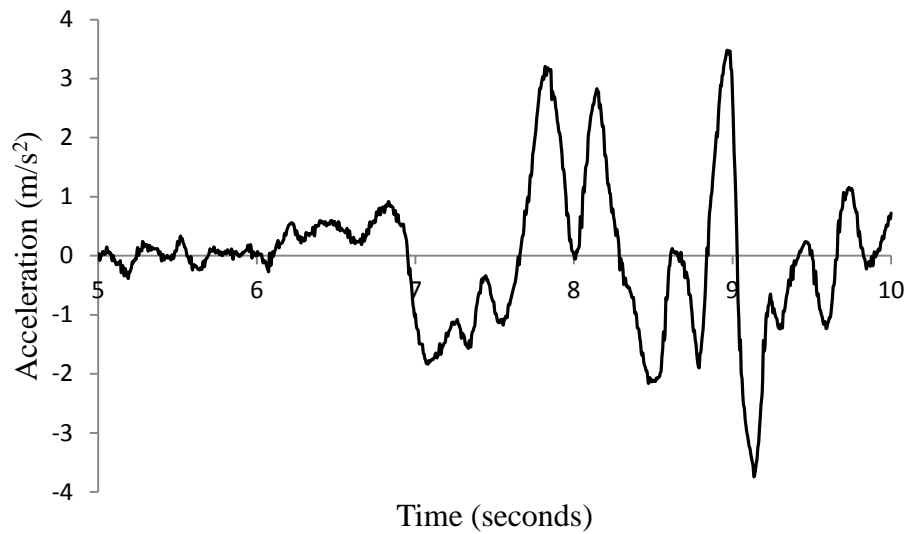


Figure 31. Acceleration versus time history record of the Düzce earthquake between 5-10 seconds

2.2.3. Free Vibration Analysis of the Cooling Tower

In this chapter basic natural frequencies and associated mode shapes of the free vibration of the Stanwell tower are presented and a parametric study is conducted to investigate the influence of various parameters such as height, thickness and curvature. Ring9 elements are used in the QR inverse iteration technique with Guyan reduction in order to obtain eigenvalues (frequencies) and eigenvectors (mode shapes). In Guyan reduction only outermost nodes are chosen as the master nodes. A convergence study is carried out to determine the required number of elements to provide an acceptable level of accuracy in the modal analysis. From convergence study 40 Ring9 elements seemed to be good enough in axial direction and one in radial direction for the modal analysis of the cooling tower.

Natural frequencies for circumferential modes of $m=0,1,2,\dots,10$ and meridional or longitudinal modes of $n=1,2,\dots,5$ for a fixed base boundary condition are presented in Table 8. This model may be regarded as preliminary in that the relatively soft column supports are not properly represented, but it illustrates the salient characteristics of the modes of vibration. Most interesting are the frequency curves on Fig. 32 for the first 10 harmonics. It should be noted that the natural frequencies decrease with increasing circumferential mode number, m until a minimum is reached whereupon they increase. It

seems to be a very typical behavior for cylindrical type shells. Looking at the Table 8 it can be seen that the first five significant circumferential modes are in the order of 4, 3, 5, 4, and 2. Therefore, it can be concluded that the behavior of the cooling tower is not a beam-like structure in which the first mode is the circumferential mode of $m=1$ corresponds a bending about a diametrical axis resulting in translation of the cross section. Also, contraction, expansion, and torsional mode shape frequencies for $m=0$ are the largest frequencies as given in Table 8. This behavior might be based on the small height to diameter ratio of the cooling tower.

Representative circumferential mode shapes are shown in Fig. 33. The $m=0$ mode represents uniform expansion and contraction of the circumference as shown in Fig. 33(a), while $m=1$ corresponds to beam-like bending about a diametrical axis resulting in translation of the cross section as shown in Fig.33(b). The higher circumferential modes $m>1$ are peculiar to shells in that they produce undulating deformations around the cross section with no net translation as shown in Fig.33(c, d, e, f, g, h). Specifically for earthquake effects, only the first mode participates in a linear analysis for uniform horizontal base motion ($m=1$). Fig. 34 depicts the first three meridional or longitudinal mode shapes along the z axis ($n=1,2,3$) corresponding to eight circumferential modes ($m=1,2,3,4,5,6,7,8$). Also, normalized radial amplitudes of vibration are shown in Fig. 34. It can be easily seen that the meridional mode shapes ($n=1,2,3$) for circumferential mode shape ($m=1$) are similar to the first three mode shapes of a cantilever beam.

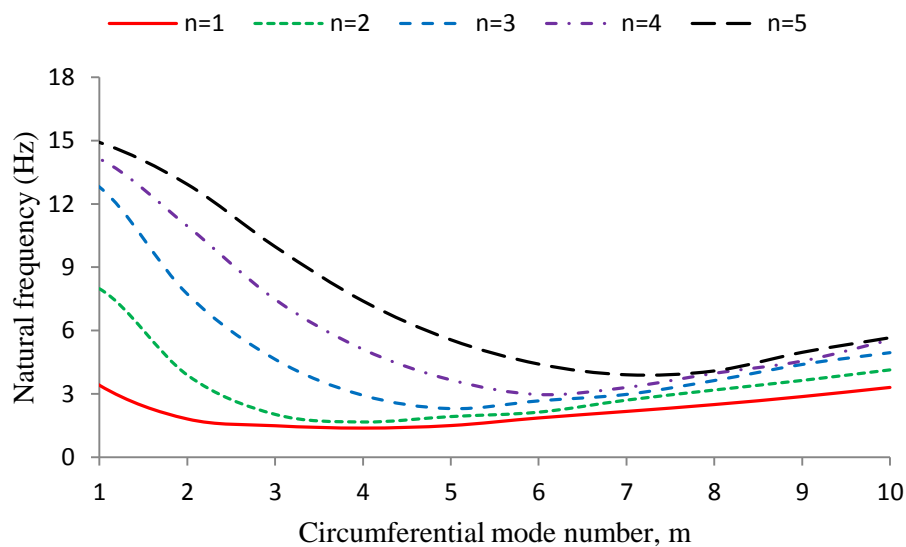


Figure 32. Natural frequencies with respect to circumferential mode number

Table 8. Natural frequencies of the Stanwell cooling tower (n:meridional mode, m:circumferential mode)

m	Natural frequency (Hz)				
	n				
	1	2	3	4	5
0	6,67	8,59	14,29	14,99	15,74
1	3,40	7,98	12,79	14,13	14,91
2	1,80	3,89	7,73	10,95	12,93
3	1,48	2,03	4,64	7,47	9,97
4	1,37	1,67	2,93	5,11	7,40
5	1,49	1,93	2,30	3,66	5,56
6	1,85	2,13	2,67	2,97	4,41
7	2,16	2,70	2,97	3,30	3,90
8	2,49	3,18	3,63	3,97	4,08
9	2,87	3,64	4,39	4,55	4,96
10	3,30	4,14	4,95	5,55	5,65

The finite element numerical method is verified with respect to the first five circumferential mode periods and the first lateral mode of the Stanwell tower obtained by (Nasir et al., 2002) using three dimensional isotropic shell elements to model the shell. An optimum mesh size is adopted after a convergence study and periods are given in Table 9.

Table 9. Finite element model verification; comparison of present results with those from previously established solutions

Method of solution	Periods of vibration (s)					
	1	2	3	4	5	6 (lateral)
Nasir et al.	0.723	0.666	0.662	0.593	0.549	0.294
Present study	0.729	0.671	0.669	0.597	0.553	0.294
Relative error	0.82%	0.75%	1.00%	0.67%	0.72%	0%

Once the finite element numerical model was verified, a parametric study is conducted on the Stanwell tower to investigate the effect of three parameters namely wall thickness, height and meridional curvature on the free vibration response of the tower.

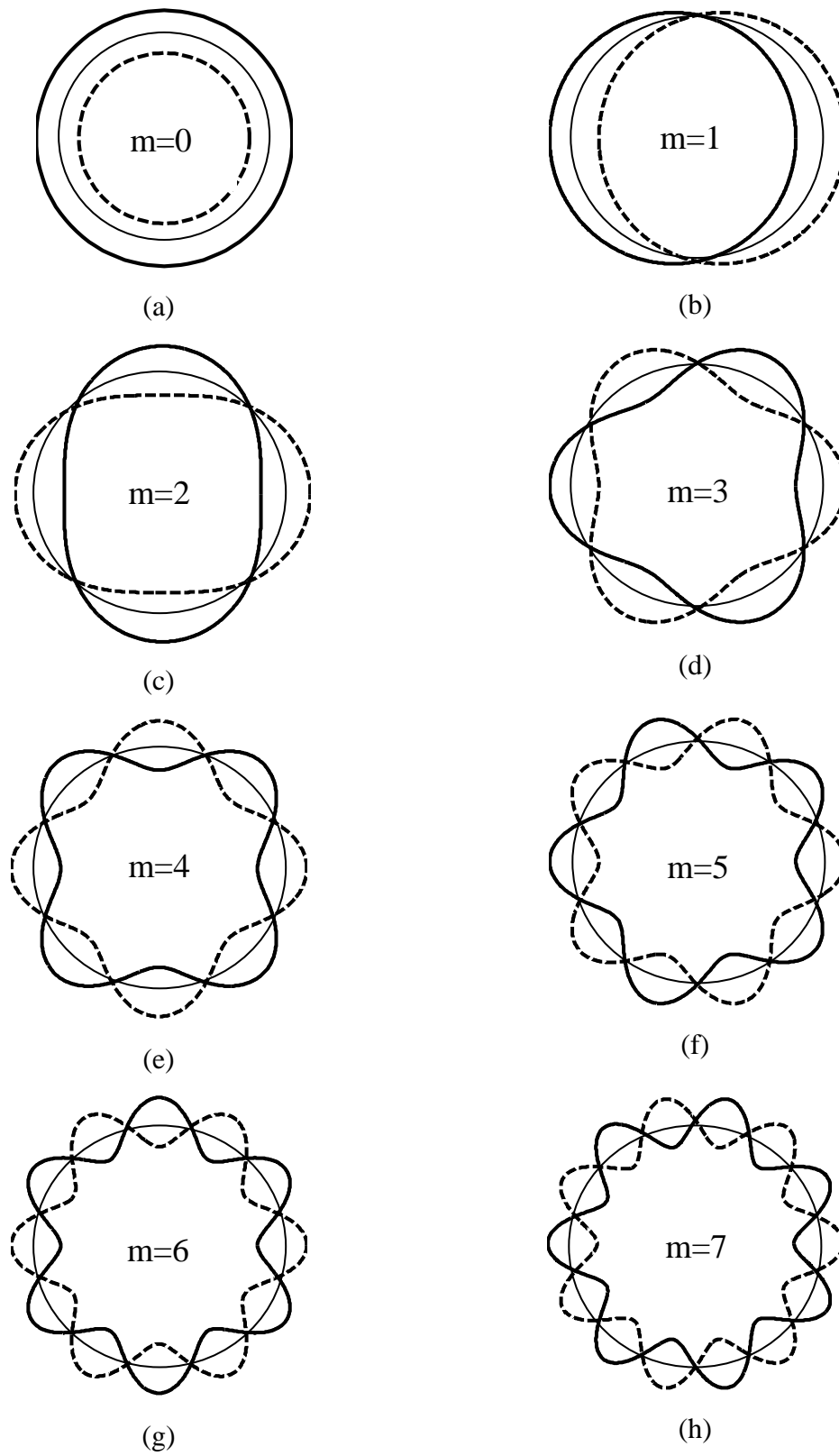


Figure 33. Circumferential mode shapes for (a) $m=0$ (b) $m=1$ (c) $m=2$ (d) $m=3$ (e) $m=4$ (f) $m=5$ (g) $m=6$ (h) $m=7$

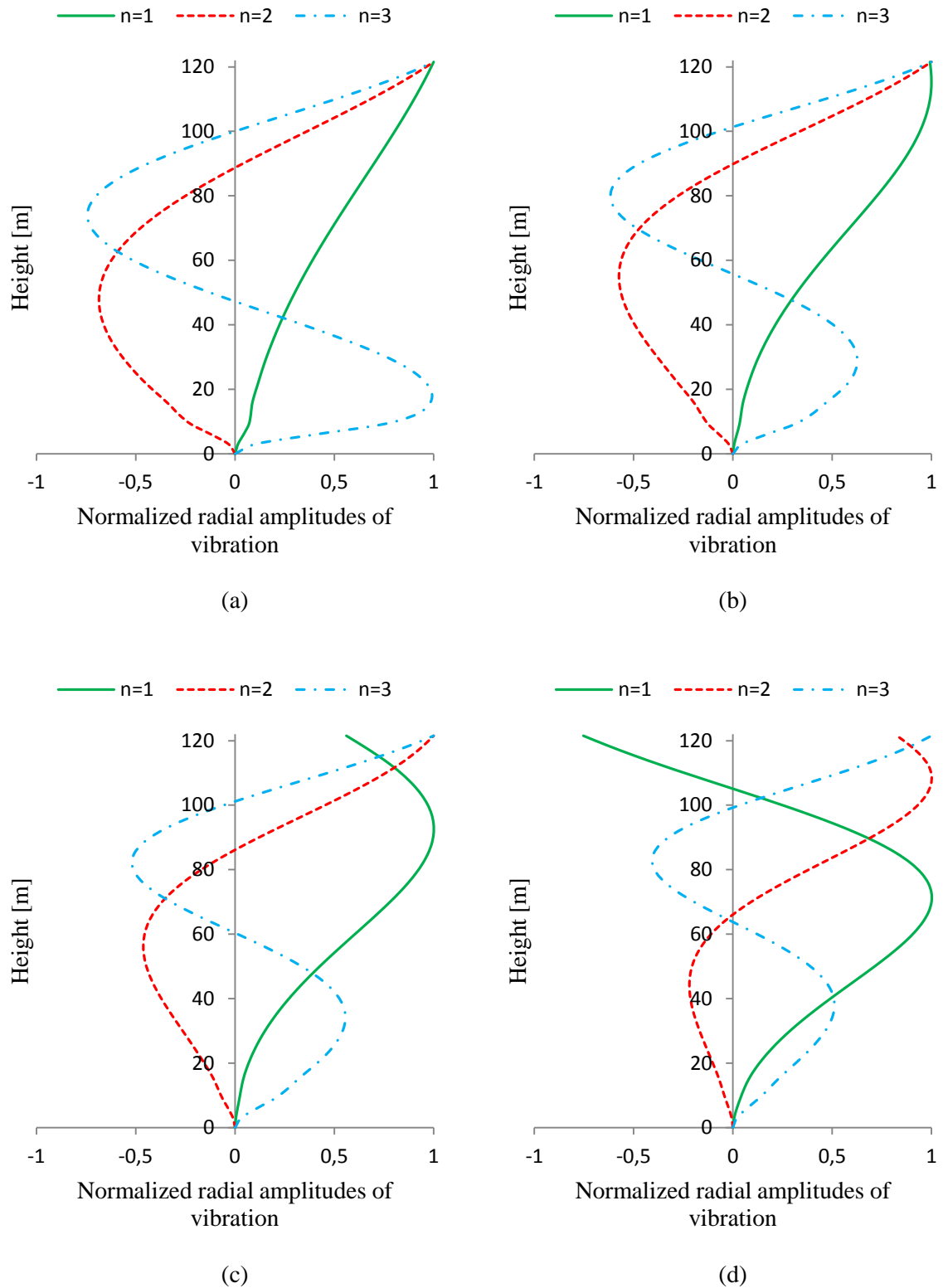
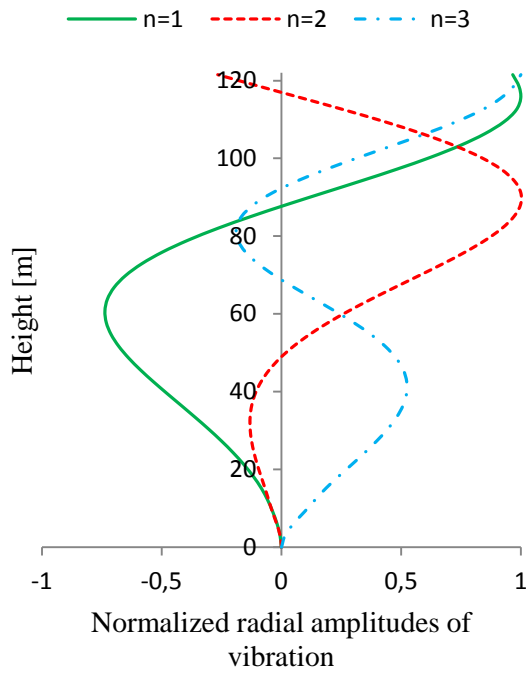
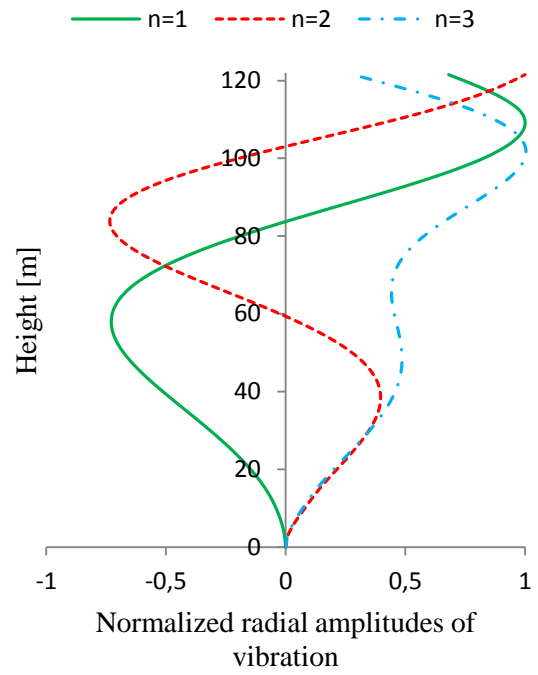


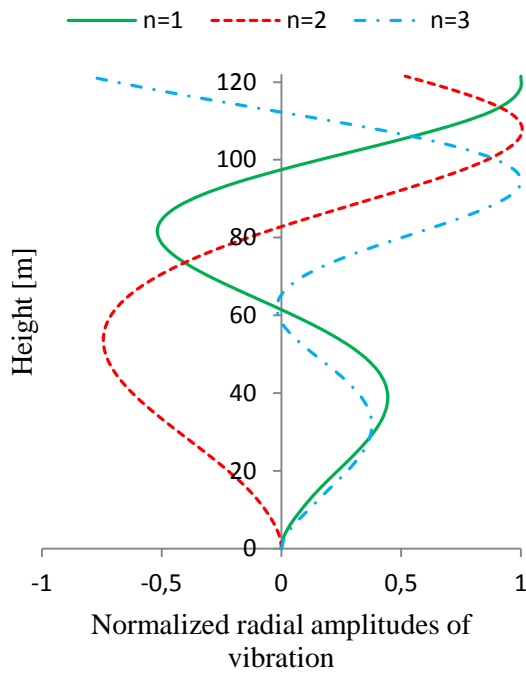
Figure 34. Normalized meridional vibration modes $n=1,2,3$ for the circumferential modes (a) $m=1$ (b) $m=2$ (c) $m=3$ (d) $m=4$



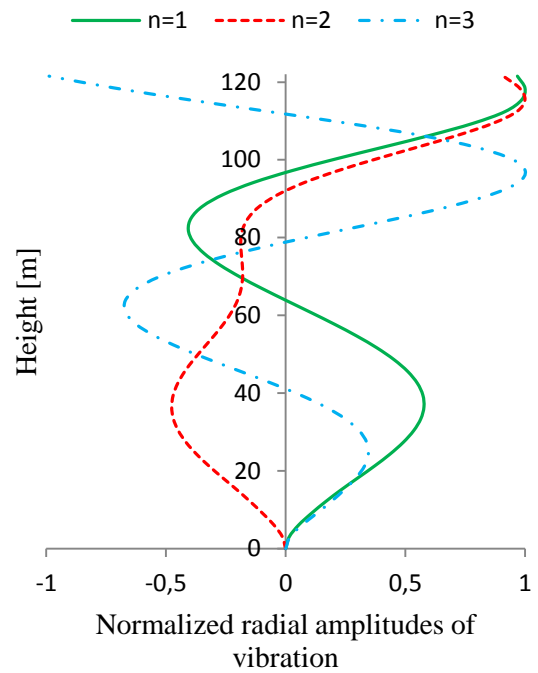
(e)



(f)



(g)



(h)

Figure 34.(Cont.) Normalized meridional vibration modes $n=1,2,3$ for the circumferential modes (e) $m=5$ (f) $m=6$ (g) $m=7$ (h) $m=8$

Three separate cases are treated, with one parameter varied at a time, keeping the others constant. To study the effect of the shell thickness, this is varied between 180 mm and 300 mm. In the next stage, height is varied between 101.5 m and 161.5 m by evenly adding or removing heights from both the upper and lower hyperbolas of the existing Stanwell tower. The base and top radii are altered during this process so as to maintain the same upper and lower curvatures. Lastly, the curvature of the 121.5 m-high Stanwell tower is varied by altering the throat diameter while the base and top diameters are constant. The throat diameter is altered between 25.78 m and 57.78 m and this provides a range of curvature as given in Table 11.

Tables 10, 11 and 12 show the results for the periods of vibration for the three cases treated. All the early modes are circumferential in nature, while the lateral modes occur very much later, beyond the 10th mode for the range of properties used. The variations of the highest period of vibration (T_1) with the shell thickness and height are approximately linear, and the changes in T_1 are 18% and 36% respectively, in the range of wall thicknesses and heights considered. The period of the first lateral mode is unaffected by a change in the thickness as given in Table 10, but it occurs earliest in the thickest shell.

Table 10. Circumferential and lateral periods of vibration of hyperbolic cooling towers of the same height and curvature with variation in shell-wall thickness

Circumferential modes		Shell Thickness (mm)				
		180	210	240	270	300
Mode 1	Period(s)	0.796	0.758	0.729	0.699	0.671
Mode 2	Period(s)	0.787	0.728	0.671	0.664	0.656
Mode 3	Period(s)	0.683	0.677	0.669	0.618	0.574
Mode 4	Period(s)	0.651	0.615	0.597	0.578	0.559
Mode 5	Period(s)	0.633	0.588	0.553	0.553	0.552
1 st lateral mode Period		0.294(29)	0.294(25)	0.294(22)	0.294(19)	0.294(17)

Table 11 shows that the lateral mode is earliest in the tallest tower, and that the periods of vibration increase with height. The results in Table 12 are for the 121.5 m-high shells having constant wall thickness of 240 mm, but with different curvatures. The variation of period of vibration is observed to be an interesting phenomenon. Fig. 35 shows the

graphical variation of the period with upper curvature k_t . It can be seen that increasing curvature causes the fundamental modal periods to decrease first and at large curvatures, this trend is reversed.

Table 11. Circumferential and lateral periods of vibration of hyperbolic cooling towers of the same curvature and shell wall thickness with variation in height of the structure

Circumferential modes		Structure Height (m)				
		101.5	121.5	131.5	141.5	161.5
Mode 1	Period(s)	0.622	0.729	0.799	0.864	0.970
Mode 2	Period(s)	0.615	0.674	0.693	0.709	0.842
Mode 3	Period(s)	0.605	0.669	0.691	0.706	0.740
Mode 4	Period(s)	0.538	0.599	0.603	0.656	0.732
Mode 5	Period(s)	0.504	0.555	0.602	0.648	0.718
1 st lateral mode Period		0.233(26)	0.294(22)	0.327(19)	0.363(19)	0.439(15)

Table 12. Circumferential and lateral periods of vibration of hyperbolic cooling tower of the same height and shell wall thickness with variation in curvature (throat diameter) of the structure

Throat Diameter (m)	25.78	37.78	43.78	45.78	49.78	55.78	57.78	
Upper curvature (k_t)	1.417	1.313	1.241	1.214	1.154	1.047	1.006	
Lower curvature (k_b)	1.098	1.089	1.083	1.080	1.076	1.067	1.065	
Circumferential modes								
Mode 1	Period (s)	0.643	0.588	0.587	0.601	0.653	0.729	0.751
Mode 2	Period (s)	0.594	0.574	0.586	0.588	0.593	0.671	0.726
Mode 3	Period (s)	0.506	0.504	0.536	0.548	0.572	0.669	0.709
Mode 4	Period (s)	0.477	0.464	0.494	0.497	0.499	0.597	0.668
Mode 5	Period (s)	0.463	0.424	0.478	0.484	0.494	0.553	0.573
1 st lateral mode period (s)	(Mode number)	0.329	0.298	0.293	0.292	0.292	0.294	0.295
		(12)	(14)	(16)	(16)	(18)	(22)	(22)

This trend is observed with the other early modes as shown in Fig. 35. The initial straight line portion of this variation shows that the stiffness of the structure increases with increase in meridional curvature, resulting in a decrease of T_1 . As a result, a change in the curvature can significantly influence the dynamic response of the shell.

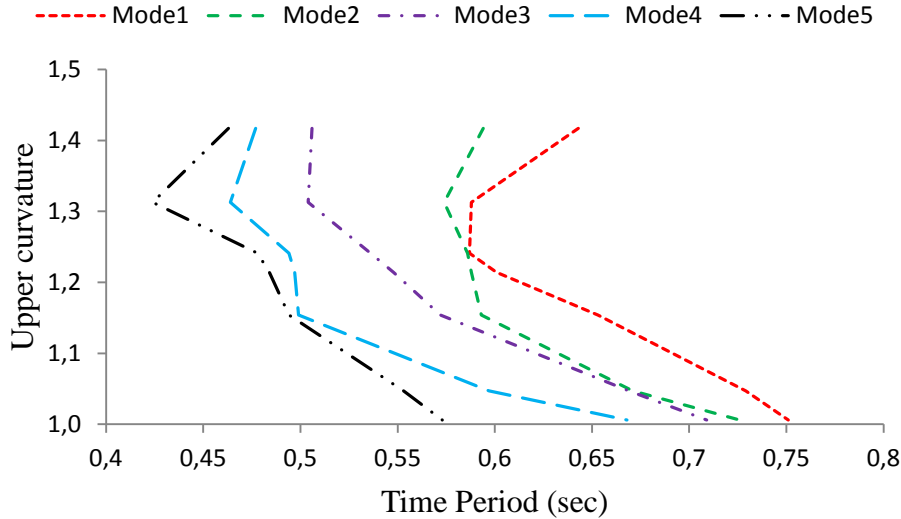


Figure 35. Effect of curvature on the response of first five circumferential periods of vibration

2.2.4. Static Analysis of the Cooling Tower

The static analysis is based on the initial geometry, linear elastic material behavior, and a linear kinematic law. The outputs of such an analysis presented here are the radial, axial displacements and circumferential, meridional stresses at the windward meridian ($\theta=0$) of the middle surface of the wall of the cooling tower under dead load and wind load in accordance with TS 498 and Eurocode. Moreover, distributions of meridional and circumferential stresses around the circumference at the base of the tower subjected to wind loading are plotted. The finite element model used in this static analysis considers the shell to be fixed at the top of the columns and, thus, does not account for the effect of the concentrated column reactions. Also, it should be remembered that the responses are considered under individual loading conditions. However, for design purposes the effects should be factored and combined to produce design values.

A convergence study is carried out and 100 Ring9 elements in axial direction and 2 Ring9 elements in radial direction are decided to be sufficient for a good level of accuracy

in the static analysis. Figs. 36 and 37 depict the radial displacements at the windward meridian ($\theta=0$) of the cooling tower for each wind load harmonics according to TS 498 and Eurocode, respectively. And Figs. 38 and 39 show the axial displacements at the windward meridian ($\theta=0$) of the cooling tower for each wind load harmonics according to TS 498 and Eurocode, respectively. The individual displacement responses of the cooling tower for each harmonic can be examined from these figures. The cumulative wind load effect on the structure in terms of radial and axial displacements for both standards can be observed in Figs. 40 and 41. It can be recognized from Fig.40 that the maximum radial displacement over the height of the tower occurs at the top ($H=121.5\text{m}$) with a value of 7.64 mm for TS 498 whereas the maximum radial displacement appears to be at the throat level ($H=91.5\text{m}$) with a value of 29.3 mm for Eurocode. The latter is about four times greater than the former due to the relatively large wind pressure distribution coefficients for circumferential modes $m>1$ produce undulating deformations around the cross section for Eurocode. It should be noted that radial deflections are not just the beam-like deflections but the combination of both beam-like deformations and undulating deformations. When the Fig. 41 is considered it can be concluded that the axial displacements for TS 498 increase with the height since the tower under just compressive wind pressure on the half portion behaves like a beam while for Eurocode the displacements oscillate through the height due to undulating shell deformations derived from higher circumferential modes ($m>1$).

The most important information a structural analyst looks for in a typical finite element static analysis is the state of stress in the structure. It is therefore very important for one to know points of optimal stresses in the element. It is known that the stress recovery at nodes from displacement elements is unreliable, as the nodes are usually the points where the strains and stresses are least accurate. Empirical evidence indicates that evaluating stresses at the Gauss integration points used in the element stiffness integration and extrapolating to the element node points generally deliver better stress values for quadrilateral elements (Felippa, 2004). Therefore, stresses given in this section are obtained at Gauss points and stress averaging is used to improve the stress accuracy.

Dead load analysis results in Figs. 42 and 43 indicate that the shell is always under compression in both directions (meridional and circumferential), except for a small circumferential tension near the top due to the geometrical form of the cooling tower. The maximum compression stresses at the bottom of the windward meridian passes through the

middle surface of the wall of the tower are -498.2 kPa and -2215 kPa in circumferential and meridional directions, respectively. Also, the maximum circumferential tension stress at the top of the windward meridian is 62.4 kPa.

In Figs. 44 through 47, the meridional and circumferential stress results of the analyses for each quasi-static wind load harmonics in accordance with TS 498 and Eurocode are shown. The cumulative or complete responses of the cooling tower under wind loading are depicted in Figs. 48 and 49. It can be seen from the figures that large tensions in both the meridional and circumferential directions are present. However, these values are significantly larger for Eurocode when compared with the values for TS 498. For instance, the maximum circumferential tension stress at the bottom of the windward meridian is 192.6 kPa for TS 498 whereas it is 529.8 kPa for Eurocode. Moreover, the maximum meridional tension stress at the bottom of the windward meridian is 851.5 kPa for TS 498 whereas the meridional stress appears to be maximum with a value of 2376.2 kPa over a distance on the windward meridian from the bottom for Eurocode. As far as these stress values are considered it can be concluded that in contrast to bluff bodies, where the magnitude of the extensional stresses along the meridian would be essentially a function of the overturning moment, the cylindrical type body is also strongly influenced by the circumferential distribution of the applied pressure. Also, the regions of tension may extend a considerable distance along the circumference from the windward meridian and the magnitude is strongly dependent on the circumferential distribution as shown in Figs. 50 and 51. These figures depict the distribution of circumferential or tangential stress around the circumference at the base and top of the cooling tower under different wind loadings.

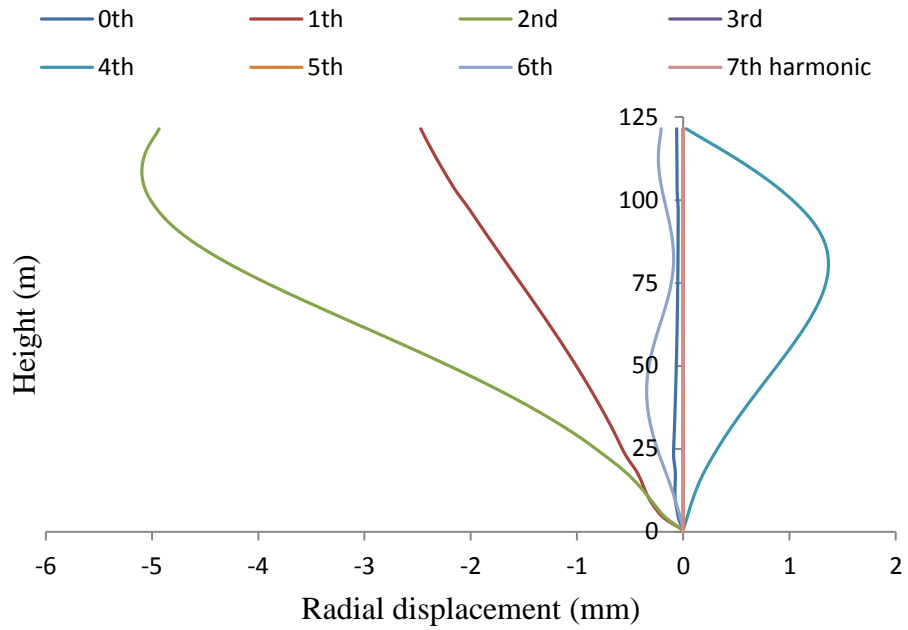


Figure 36. Radial displacements at windward meridian ($\theta=0$) of the cooling tower throughout the height for each wind load harmonics according to TS 498

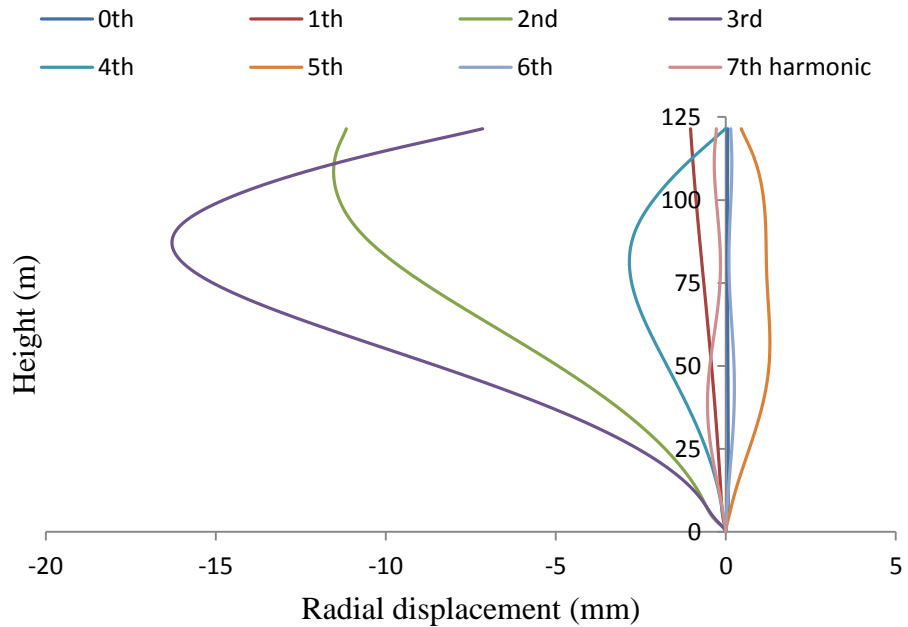


Figure 37. Radial displacements at windward meridian ($\theta=0$) of the cooling tower throughout the height for each wind load harmonics according to Eurocode

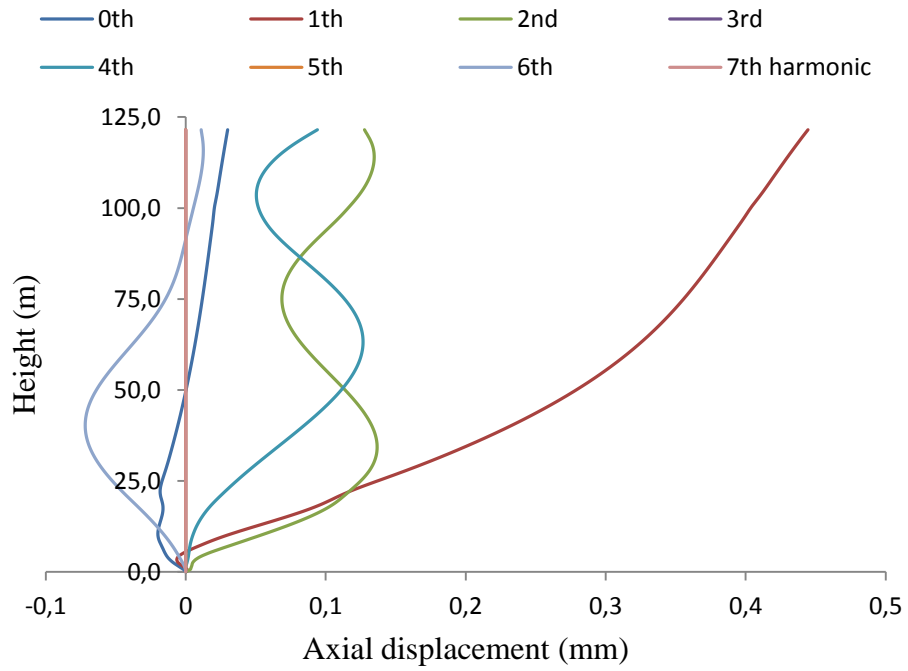


Figure 38. Axial displacements at windward meridian ($\theta=0$) of the cooling tower throughout the height for each wind load harmonics according to TS 498

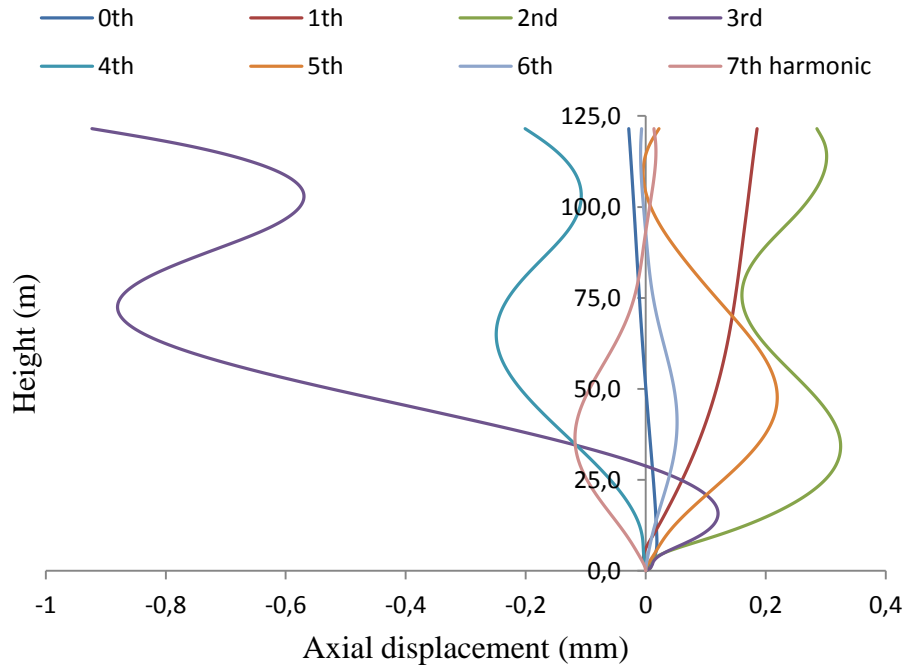


Figure 39. Axial displacements at windward meridian ($\theta=0$) of the cooling tower throughout the height for each wind load harmonics according to Eurocode

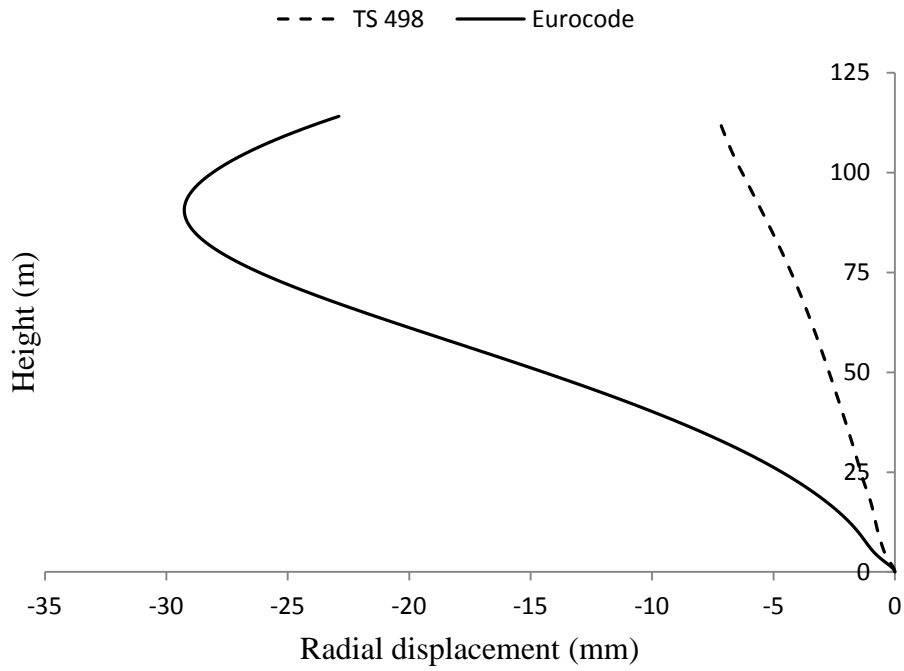


Figure 40. Radial displacements at windward meridian ($\theta=0$) of the cooling tower under wind load throughout the height according to TS 498 and Eurocode

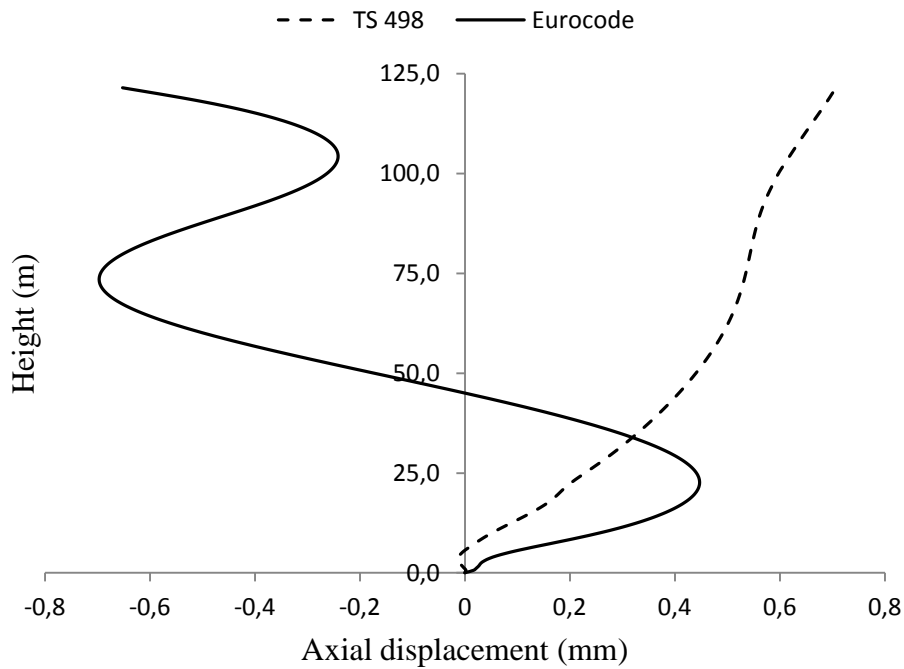


Figure 41. Axial displacements at windward meridian ($\theta=0$) of the cooling tower under wind load throughout the height according to TS 498 and Eurocode

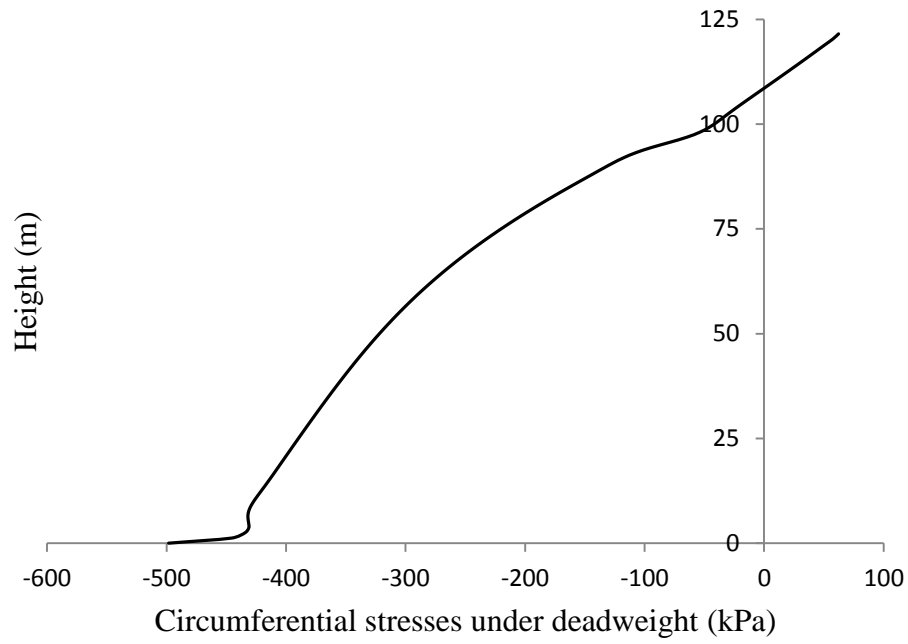


Figure 42. Circumferential stresses at windward meridian ($\theta=0$) throughout the height of the cooling tower under deadweight

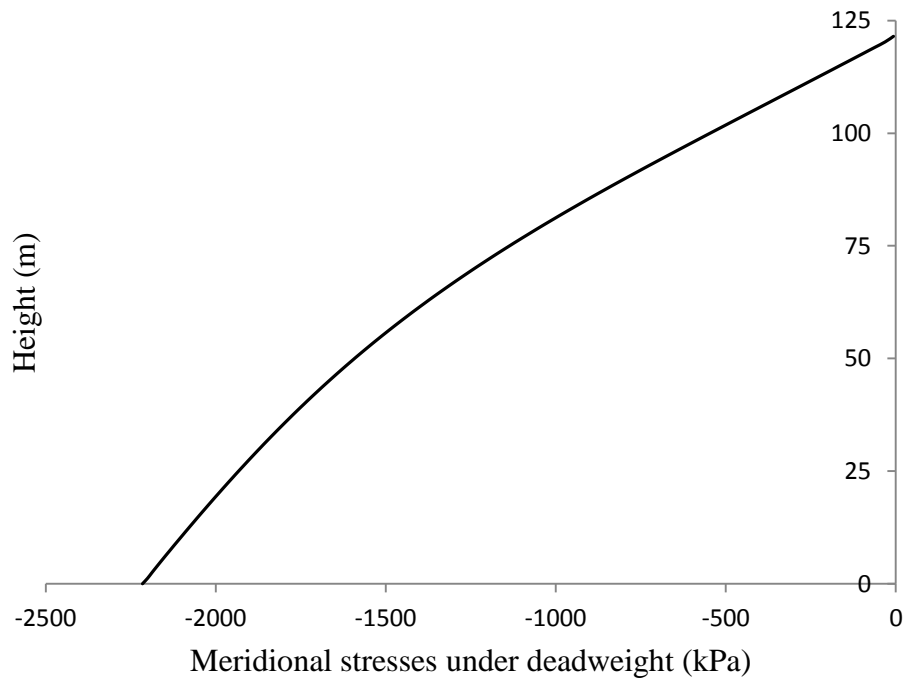


Figure 43. Meridional stresses at windward meridian ($\theta=0$) throughout the height of the cooling tower under deadweight

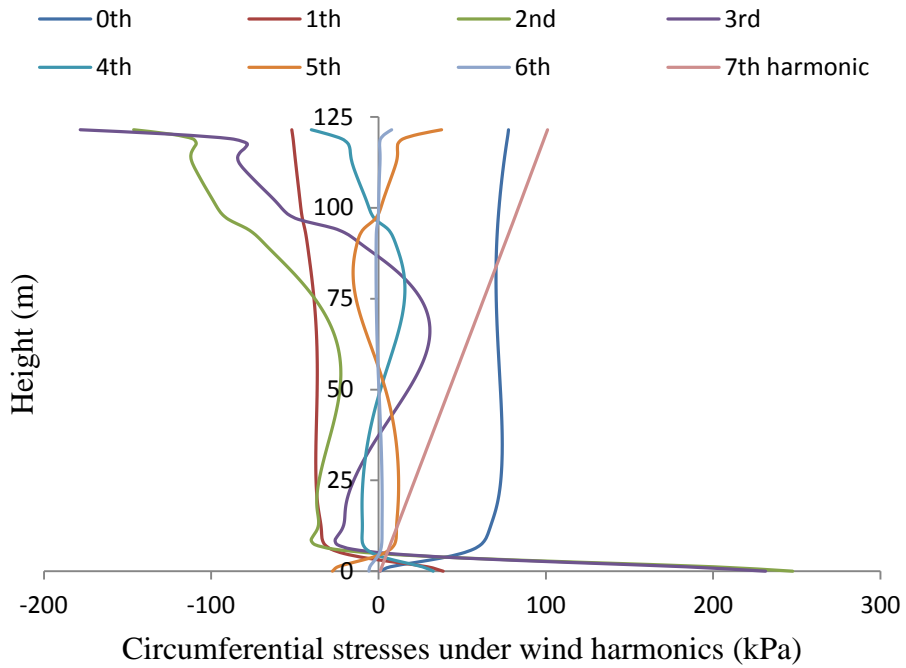


Figure 44. Circumferential stresses at windward meridian ($\theta=0$) throughout the height of the cooling tower for each wind load harmonics according to Eurocode

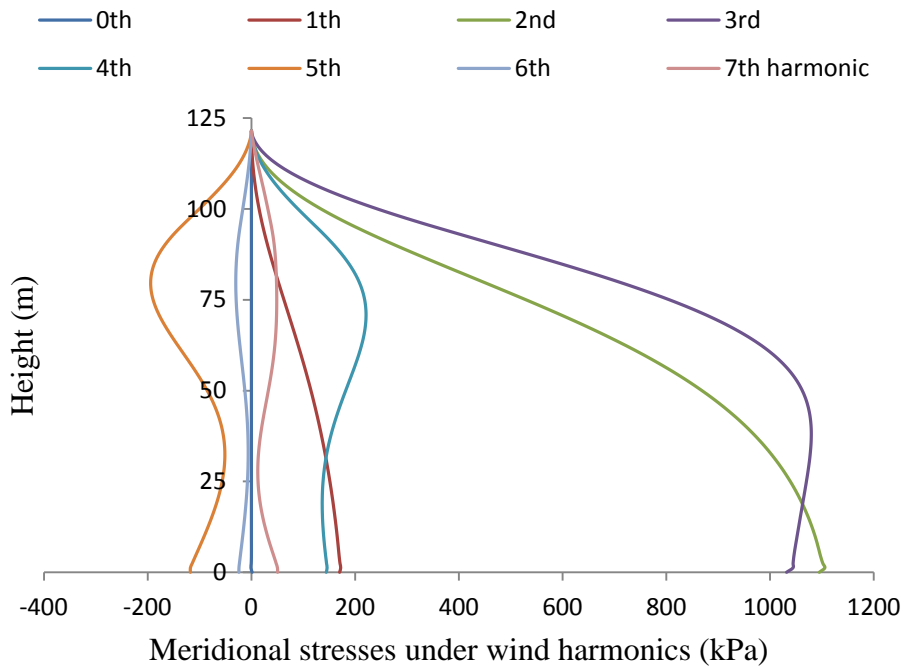


Figure 45. Meridional stresses at windward meridian ($\theta=0$) throughout the height of the cooling tower for each wind load harmonics according to Eurocode

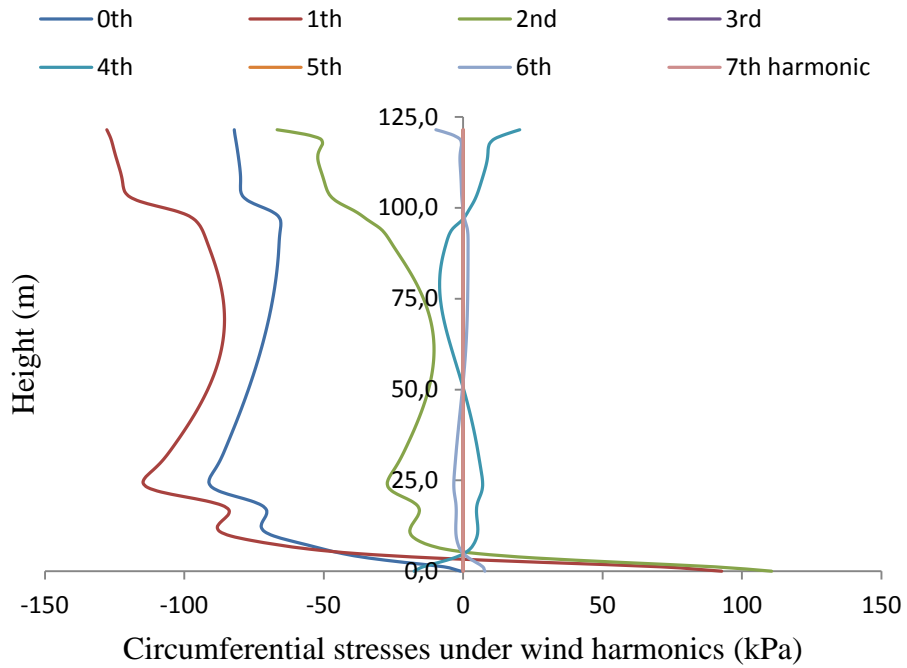


Figure 46. Circumferential stresses at windward meridian ($\theta=0$) throughout the height of the cooling tower for each wind load harmonics according to TS 498

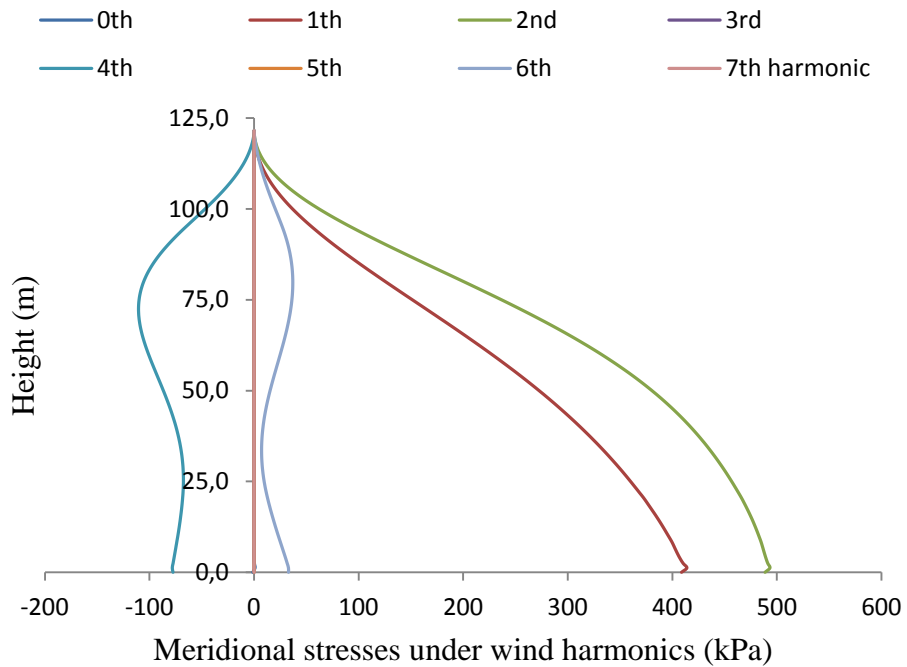


Figure 47. Meridional stresses at windward meridian ($\theta=0$) throughout the height of the cooling tower for each wind load harmonics according to TS 498

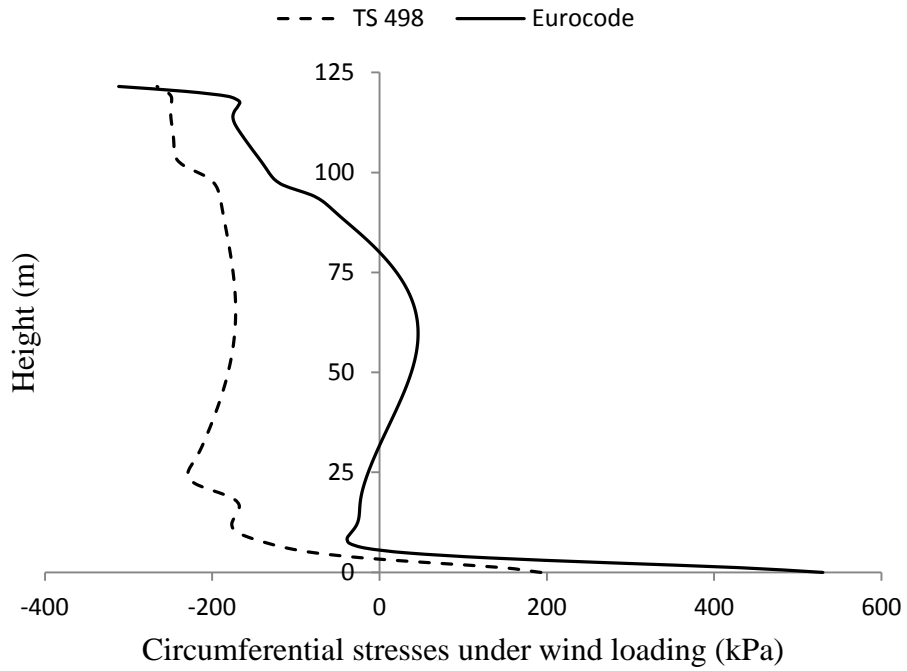


Figure 48. Circumferential stresses at windward meridian ($\theta=0$) throughout the height of the cooling tower under wind load according to TS 498 and Eurocode

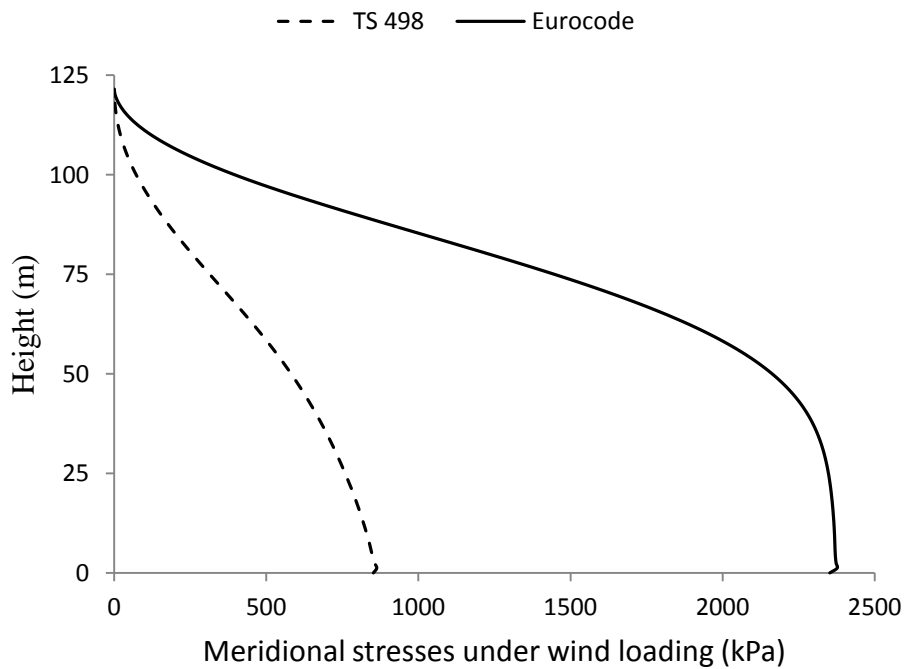


Figure 49. Meridional stresses at windward meridian ($\theta=0$) throughout the height of the cooling tower under wind load according to TS 498 and Eurocode

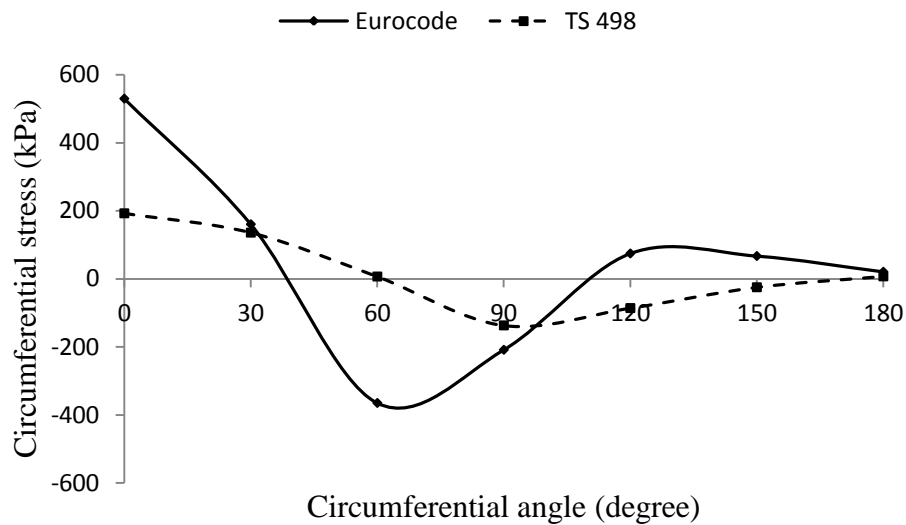


Figure 50. Distribution of the circumferential stress around the circumference at the base of the Stanwell tower subjected to wind pressure

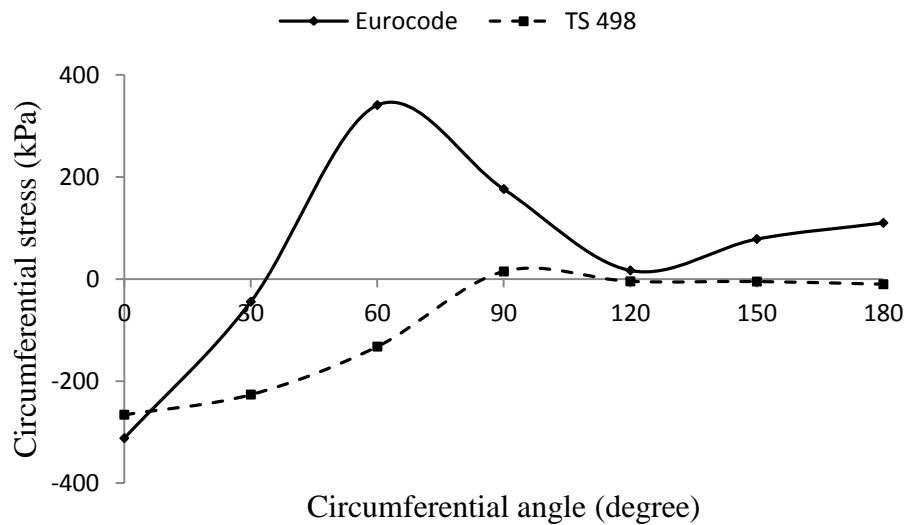


Figure 51. Distribution of the circumferential stress around the circumference at the top of the Stanwell tower subjected to wind pressure

2.2.5. Dynamic Analysis of the Cooling Tower

Dynamic load of interest include only seismic actions that are time dependent. Seismic loads are modeled in the finite element time history analysis as ground accelerations applied at the base of the structure, and the response is analyzed by Newmark

direct integration using time history records. The transient responses of the six hyperbolic axisymmetric shell structures with variations in wall thickness, height and curvature values as given in Table 13 to earthquake loading by direct integration using time history records of Düzce earthquake as plotted in Fig. 31 are discussed in this section and results are presented in graphical format.

Table 13. Six different models analyzed for earthquake loading

Model #	Nomenclature	Height (m)	Wall thickness (mm)	Throat radius (m)
1	ht-141	141.5	240	27.89
2	ht-101	101.5	240	27.89
3	th-300	121.5	300	27.89
4	th-180	121.5	180	27.89
5	r-21	121.5	240	21.89
6	ht-121-Stanwell/th-240- Stanwell/r-27-Stanwell	121.5	240	27.89

Figs. 52, 53 and 54 show the response in terms of deflections and stresses along the height for these different models. The results are obtained for the time step of 0.005 s when the maximum values are reached. During the earthquake these stresses keep on reversing from tension to compression and vice versa as shown in Figs. 55 and 56. From the results, it can be seen that the tallest shell structure experiences some of the largest deflections and stresses as depicted in Fig. 52. The value of the top deflection is increased by 49% in ht-141 (the tallest structure) and decreased 60% in ht-101 (the shortest structure), compared with values for the Stanwell cooling tower as shown in Fig. 52(a). The meridional stress at the base is increased by 13% in ht-141 and decreased by 47% in ht-101, as shown in Fig. 52(b). The hoop or circumferential stresses are more critical at the top. They are increased by 5.5% in ht-141 and decreased by 30% in ht-101, as shown in Fig. 52(c). Comparison of models of the same height but different wall thicknesses indicate higher stress resultants in shells with thicker walls, as shown in Fig. 53(a, b). The stress resultants are worked out by multiplying the average stress (stress at the center Gauss point) by the corresponding wall

thicknesses for better plotting. The stresses, on the other hand, are almost identical in all the three cases. As the top curvature k_t increases (due to a decrease in throat radius), the meridional stress at the throat levels increases but decreases by 20% at the base as shown in Fig. 54(a), while the circumferential stress increases by 25% at the top as shown in Fig. 54(b). From these figures it can be concluded that maximum circumferential stress increases with increase in curvature while maximum meridional stress decreases. Thus, the hyperbolic axisymmetric structure is observed to be quite sensitive to curvature and can be optimized by investigating the modal shapes and the period of vibrations. Such optimization can be achieved by changing curvature thus improving earthquake response. This may ultimately involve the variation of the shell thickness over the height of the structure.

Figs. 55 and 56 show the meridional and circumferential stress responses along the height of the Stanwell hyperbolic cooling tower subjected to Düzce earthquake loading for each time step during Newmark dynamic analysis, respectively. As mentioned before during the earthquake these stresses carry on reversing from tension to compression and vice versa. Dark regions in these figures indicate that the stresses intensify within small interval during the earthquake.

Fig. 57 (a, b, c) depict the time histories of the maximum lateral (radial) displacement at the top of the Stanwell tower, maximum meridional stress at the base of the Stanwell tower and maximum circumferential stress at the top of the Stanwell tower under Düzce earthquake loading, respectively. As shown in these figures maximum values within the earthquake duration are obtained at around the time of maximum ground acceleration appeared at the 9.135 second of the earthquake. The maximum radial displacement at the top, maximum tensional meridional stress at the base and maximum tensional circumferential stress at the top of the Stanwell cooling tower are obtained as 33.1 mm, 5129.8 kPa and 1195.8 kPa respectively using the time-acceleration records within the duration of 5-10 s. of Düzce earthquake in Newmark direct integration method.

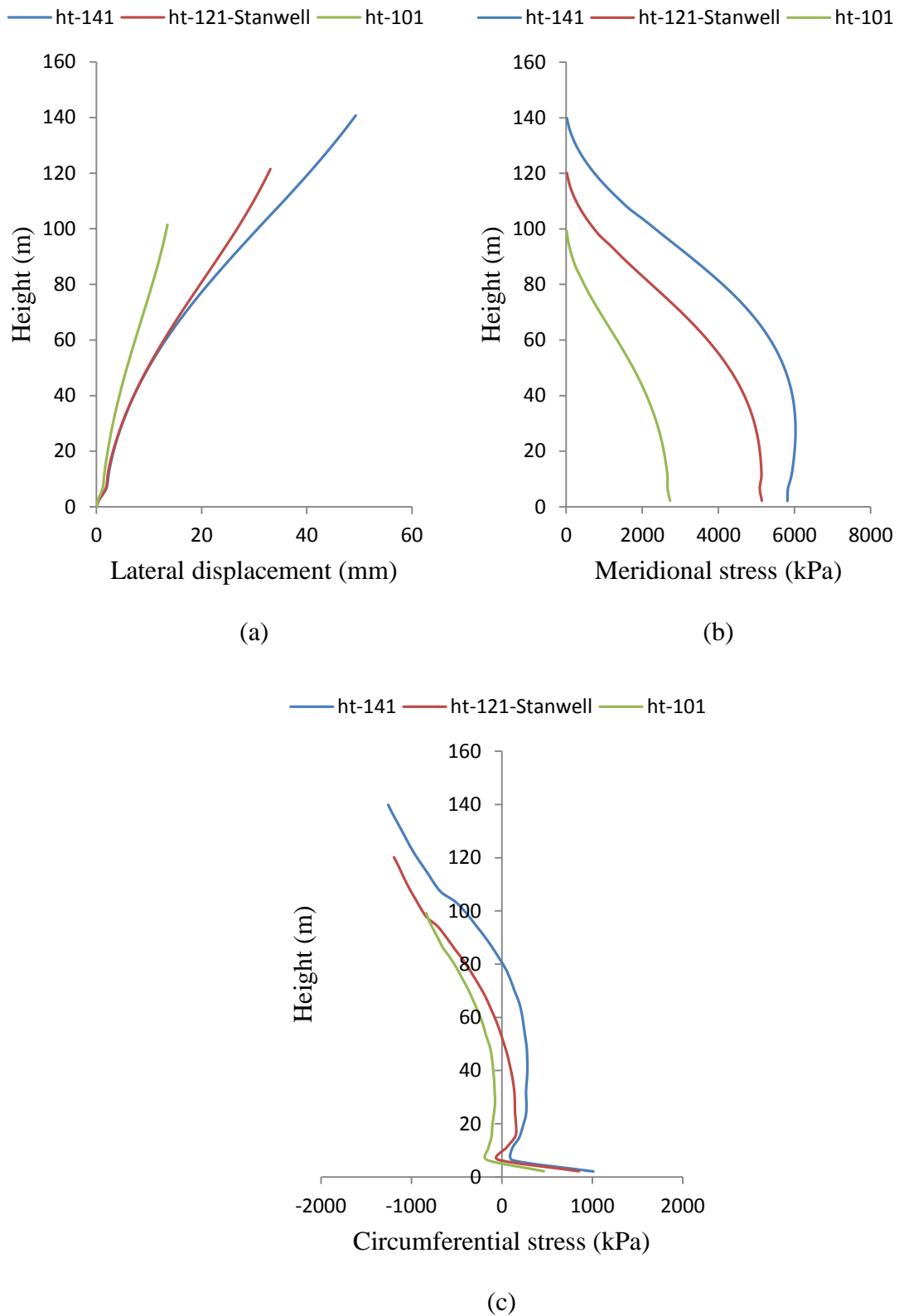


Figure 52. Responses along the three different heights of hyperbolic cooling tower under Düzce earthquake loading of (a) the lateral deflection (b) the meridional stress and (c) the circumferential stress when the maximum values are reached

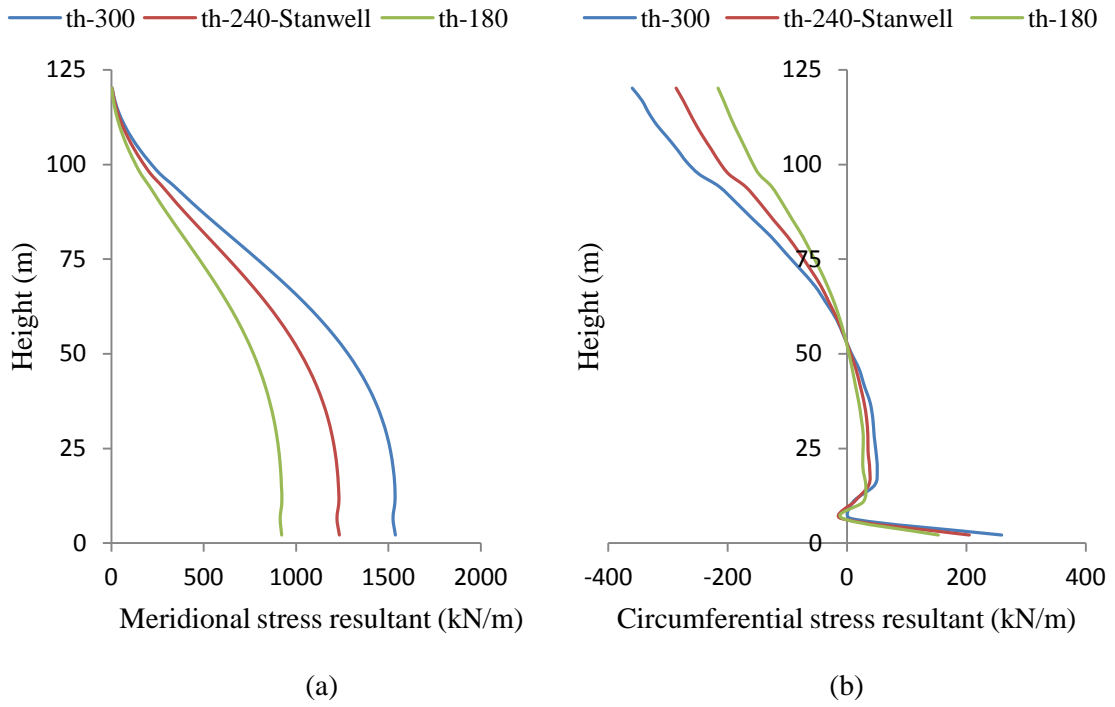


Figure 53. (a) Meridional and (b) Circumferential stress resultants of the three different wall thicknesses of the hyperbolic cooling tower under Düzce earthquake loading along the height when the maximum values are reached

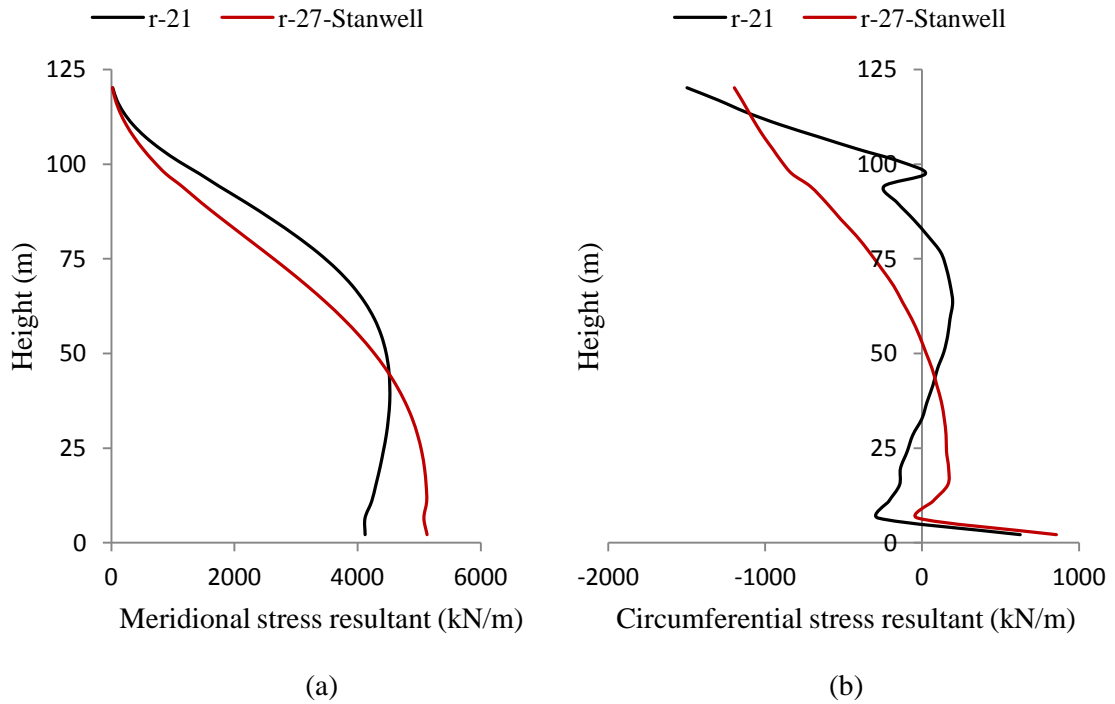


Figure 54. (a) Meridional and (b) circumferential stress responses of two different curvatures of the hyperbolic cooling tower under Düzce earthquake loading along the height when the maximum values are reached

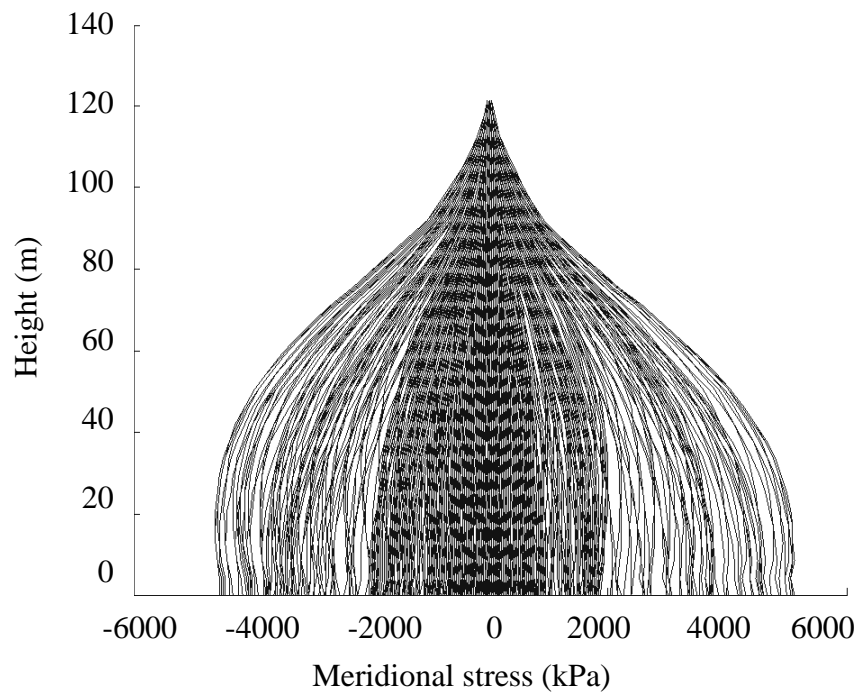


Figure 55. Meridional stress responses along the height of the Stanwell hyperbolic cooling tower under Düzce earthquake loading

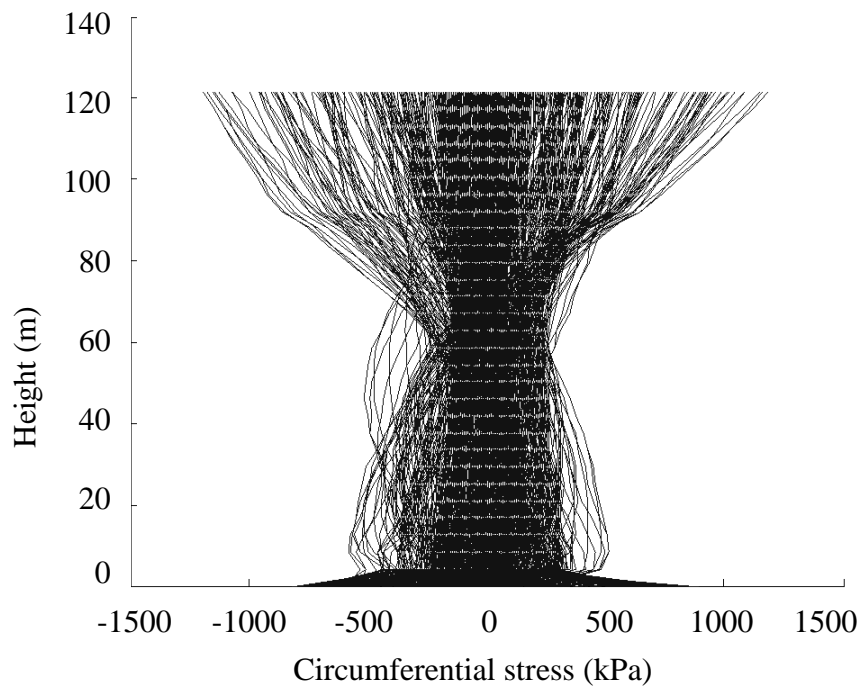
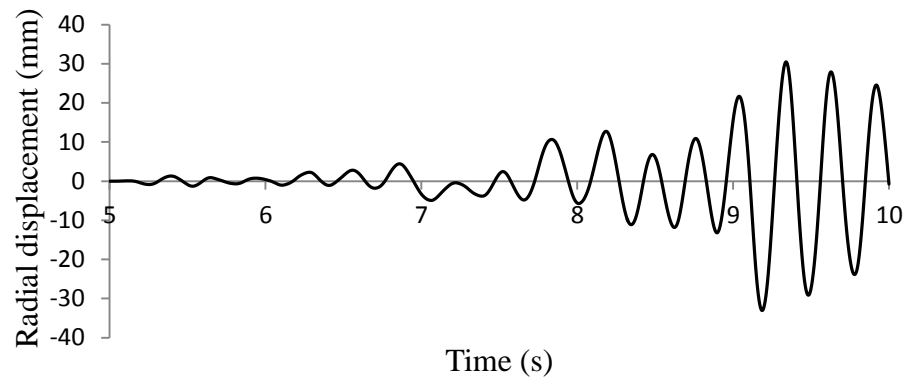
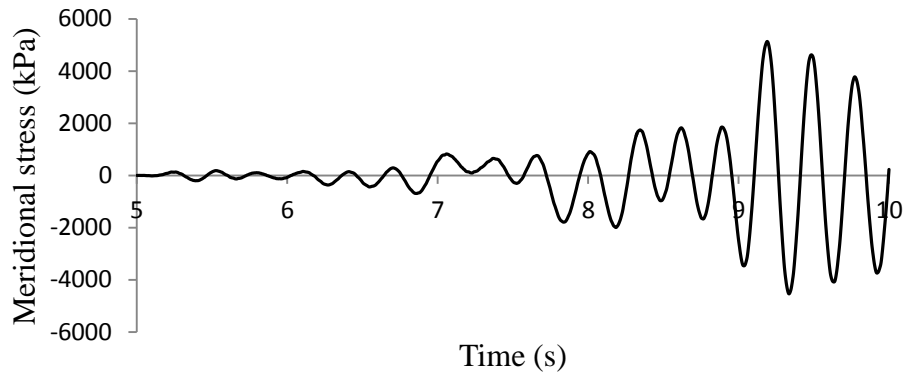


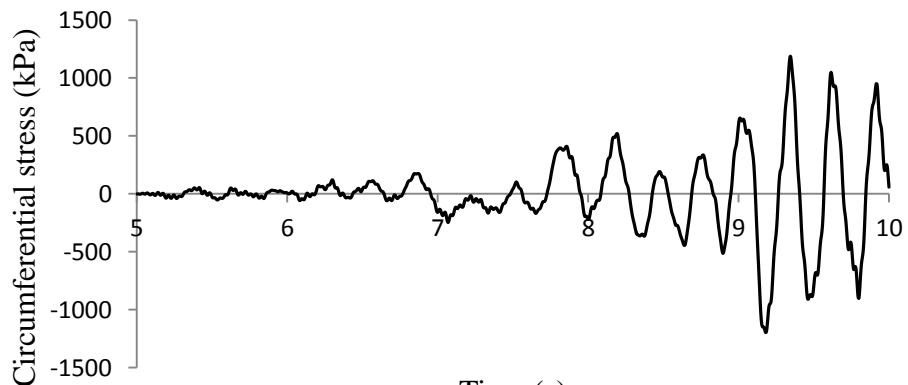
Figure 56. Circumferential stress responses along the height of the Stanwell hyperbolic cooling tower under Düzce earthquake loading



(a)



(b)



(c)

Figure 57 Time history of the (a) maximum lateral (radial) displacement (b) maximum meridional stress and (c) maximum circumferential stress of the Stanwell tower under Düzce earthquake loading

3. CONCLUSIONS AND RECOMMENDATIONS

Static, forced and free vibration analysis of axisymmetric structures subjected to non-axisymmetric loadings such as wind pressure as well as axisymmetric loading such as inertia force are studied using 4-noded and 9-noded quadrilateral ring elements. The geometry of the axisymmetric structure to be analyzed is defined parametrically and nodal coordinates can be obtained easily by the coded program. The verification of the program was done by solving several benchmark problems such as internally pressurized thick cylinder, rotating thin disc and circular plate bending problems. The stresses and the displacements were compared with the exact solutions and very good agreement was achieved. The analysis of cooling towers was studied next to show the applicability of the program to an important practical problem. Stanwell cooling tower was analyzed under wind loading according to TS 498 and Eurocode, and Düzce earthquake loading. Also, the free vibration analysis of the tower was conducted. Additionally, the influence of height, thickness and curvature parameters on the response of such cooling towers was examined by changing one parameter while keeping the others constant.

Most important conclusions drawn from the study are as follows:

- Almost all practically used revolutionary axisymmetric objects, such as cylindrical, conical, spherical, ellipsoidal, hyperboloidal, paraboloidal, etc. can be obtained parametrically.
- In the case of hollow cylinder problem under axial load, axial torque and lateral load the relative errors compare to analytical solutions are very small for both Ring4 and Ring9 and decrease with the mesh refinement.
- The natural frequencies obtained in the case of modal analysis of a hollow cylinder are very close to each other for FEM with and without model reduction technique, which verifies that solid ring elements with model reduction can be used successfully for the modal analysis of axisymmetric structures.
- In the case of internally pressurized thick cylinder hole edge radial stresses using ring elements are underestimated due to impossibility of doing interelement stress averaging at that high stress edge.
- Volumetric locking problem was observed using Ring4 in case of internally pressurized thick cylinder for low values of Poisson's ratio.

- Shear locking problem was observed in the case of plate bending problem for low values of the thickness using Ring4.
- Convergence rate of Ring4 suffering from shear locking becomes much smaller as the thickness to diameter ratio of the circular plate decreases but that of Ring9 is not that significant.
- Results obtained using full integration and selectively reduced integration come so close to each other at the ratio of $H/D=0.05$ for center displacement and $H/D=0.1$ for radial stresses. That means that above these certain limits shear locking disappears.
- Non-axisymmetric wind loadings are described according to TS 498 and Eurocode and can be expressed using Fourier series with eight harmonics.
- As far as Fourier coefficients for wind loading are examined it can be concluded that Eurocode indicates that a significant portion of the wind loading will cause shell deformations in circumferential mode greater than $m=1$. However, TS 498 indicates that the tower deforms in the translational mode of beam-like response.
- The tensile and compressive stress resultants are sensitive to the type of circumferential distribution curve of the wind loading.
- The natural frequencies of the Stanwell cooling tower decrease with increasing circumferential mode number until a minimum is reached whereupon they increase.
- Height of the cooling tower is seen to have the greatest influence on the free vibration response, with increase of height significantly increasing the period of vibration.
- Increasing curvature causes the fundamental periods to decrease first and at large curvatures, this trend is reversed.
- The variations of the highest period of vibration with the shell thickness and height are approximately linear.
- Dead load analysis results that the shell is always under compression in both meridional and circumferential directions, except for a small circumferential tension near the top due to the hyperbolic shape of the cooling tower.
- Hoop stresses are greatly affected by changes in shell curvature. The response is quite sensitive to high curvature values, which must be avoided.

- Stresses due to the earthquake excitation keep on reversing from tension to compression and vice versa.
- Maximum circumferential stress occurred at the top and maximum meridional stress was observed at the base of the structure of the Stanwell cooling tower under seismic loading.

Some recommendations may be given for future studies as followings:

- Rotational freedom can be added to the finite element model to estimate the behavior of the structures such as plates in bending more precisely.
- In the work related to the analysis of hyperbolic cooling towers, under either dead, wind or earthquake loads, only the fixed based tower shell was considered in the analysis. However, the tower shell is supported by columns. In order to consider realistic boundary conditions, it is essential to consider the supporting columns in the analysis along with the shell.
- In order to be able to consider the column effects in the analysis it may be possible to transform these columns into equivalent shell surfaces, so that the coded elements can be utilized.
- One element type can be used for modeling of different environment such as structures, soil and water. Therefore, interaction problems coupled eigenvalue problem can be investigated.
- The hyperbolic shape and wall thickness of the cooling towers can be optimized by investigating the frequency of the structure.
- Linear elastic analysis of axisymmetric structures is performed. Nonlinearities may also be considered for a better analysis.
- The study can be improved by incorporating the temperature effect on the static and dynamic behavior of the cooling tower.

4. REFERENCES

- Ahmadian, M.,T. and Bonakdar, M., 2008, A New Cylindrical Element Formulation and Its Application to Structural Analysis of Laminated Hollow Cylinders, Finite Elements in Analysis and Design, 44, 617-630.
- Baillis, Ch., Jullien, J.,F. and Limam, A., 2000. An Enriched 2D Modeling of Cooling Towers: Effects of Real Damage on the Stability Under Self weight and on the Strength Under Wind Pressure, Engineering Structures, 22, 831-846.
- Bathe, K., J., 1996. Finite Element Procedures, Prentice-Hall, USA.
- Benasciutti, D., De Bona, F. and Munteanu, M.,Gh., 2011. Numerical Analysis- Theory and Application, InTech, Italy.
- Bhatti, M., A., 2006. Advanced Topics in Finite Element Analysis of Structures: with Mathematica and Matlab Computations, John Wiley&Sons, USA.
- Busch, D., Harte, R., Kratzig, W.,B. and Montag, U., 2002. New Natural Draft Cooling Tower of 200 m of Height, Engineering Structures, 24, 1509-1521.
- Clough, R.,W. and Penzien, J., 1975. Dynamics of Structures, McGraw-Hill, USA.
- Cook, R.,D., Malkus, D.,S. and Plesha, M.,E., 1989. Concepts and Applications of Finite Element Analysis, 3rd Edition, Wiley & Sons, USA.
- Felippa, A., C., 2011. IFEM Lecture Notes, Department of Aerospace Engineering Sciences, University of Colorado at Boulder.
- Florin, T.,O. and Sunai, G., 2010. Evaluation of Damping in Dynamic Analysis of Structures, Int. J. Math. Models and Methods in Applied Sciences, 2,4, 124-131.
- Higgins, W. and Basu, D., 2011. Fourier Finite Element Analysis of Laterally Loaded Piles in Elastic Media, International Geotechnical Report 2011-1, Paper 2.
- Hong, T. and Teng, J.,G., 2002. Non-linear Analysis of Shells of Revolution Under Arbitrary Loads, Computers and Structures, 80, 1547-1568.
- Jog, C.,S. and Annabattula, R., 2006. The Development of Hybrid Axisymmetric Elements Based on the :Hellinger-Reissner Variational Principle, Int. J. Numer. Meth. Engng, 65, 2279-2291.
- Kang, J.,H. and Leissa, A.,W., 2005. Three Dimensional Vibration Analysis of Thick Hyperboloidal Shells of Revolution, Journal of Sound and Vibration, 282, 277-296.

- Karadeniz, H., 2009. Spectral Analysis Program of Structures: SAPOS User Manual, Delft University of Technology, Netherlands, 79-90.
- Kim, J.,G. and Kim, Y.,Y., 2000. A Higher-order Hybrid-mixed Harmonic Shell-of revolution Element, Comput. Methods Appl. Mech. Engrg., 182, 1-16.
- Lang, C., Meiswinkel, R. and Filippou, F.,C., 2002. Non-linear Analysis of Shells of Revolution with Ring Elements, Engineering Structures, 24, 163-177.
- Nasir, A.,M., Thambiratnam, D.,P., Butler, D. and Austin, P., 2002. Dynamics of Axisymmetric Hyperbolic Shell Structures, Thin-Walled Structures, 40, 665-690.
- Noorzaei, J., Naghshineh, A., Abdul Kadis, M.,R., Thanoon, W.,A. and Jaafar, M.,S., 2006. Nonlinear Interactive Analysis of Cooling Tower-Foundation-Soil Interaction Under Unsymmetrical Wind Load, Thin-Walled Structures, 44, 997-1005.
- prEn 1991-1-4, 2004. Eurocode 1: Actions on Structures- Part 1-4: General Actions-Wind Actions, Brussels.
- Phillip, L. and Gouldand, W.,B., 2005. Handbook of Structural Engineering, 2nd Edition, CRC Press, Germany.
- Redekop, D., 2004. Free Vibration of Hollow Bodies of Revolution, Journal of Sound and vibration, 273, 415-420.
- Smith, J., W., 1988. Vibration of Structures: Applications in Civil Engineering Design, Chapman and Hall, USA.
- Timoshenko, S., Goodier, J., N., 1951. Theory of Elasticity, McGraw-Hill, New York.
- T.S.E., 1997. Yapı Elemanlarının Boyutlandırmasında Alınacak Yüklerin Hesap Değerleri, TS 498, Türk Standartları Enstitüsü, Ankara.
- Ugural, A., C., 1981. Stresses in Plates and Shells, McGraw-Hill, USA.
- Viladkar, M.,N., Godbole, P.,N. and Krishna P., 1998. Finite Element Analysis of Column Supported Hyperbolic Cooling Towers Using Semi-loof Shell and Beam Elements, Engineering Structures, 20,1-2, 75-85.
- Viladkar, M.,N., Karisiddappa, Bhargava, P. and Godbole, P.,N., 2006. Static Soil-Structure Interaction Response of Hyperbolic Cooling Towers to Symmetrical Wind Loads, Engineering Structures, 28, 1236-1251.
- Zienkiewicz, O.,C. and Taylor, R.,L., 2000. The Finite Element Method -Volume 2: Solid Mechanics, 5th Edition, Butterworth-Heinemann, UK.

CURRICULUM VITA

PERSONAL INFORMATION

Surname, Name: KARAKAŞ, Ali İhsan
Date of Birth: 29.01.1986
Place of Birth: Trabzon
Nationality: Turkish (TC)
Marital Status: Single
Email: aliihsanka@yahoo.com

EDUCATION

Degree	Institution	Year of Graduation
BS	Boğaziçi University Civil Engineering Department	2009
High School	Trabzon High School	2004
Primary School	İsmetpaşa Primary School	2000

WORK EXPERIENCE

Year	Place	Status
2010-Present	Karadeniz Technical University	Research Assistant

FOREIGN LANGUAGES

English

SCHOLARSHIP

National Scholarship Programme of TUBITAK for Master Students

HOBIES

Painting, Table Tennis, Volleyball